Aspects of Nuclear Phenomena Under Explosive Astrophysical Conditions

C. Ruiz, B.Sc

Thesis submitted for the degree of Doctor of Philosophy in the Faculty of Science and Engineering

School of Physics

University of Edinburgh

2003

Abstract

The breakout of the hot CNO cycle and the onset of the rapid-proton process are of significant importance to our understanding of the nucleosynthesis of proton-rich nuclei in our universe. In particular $^{15}O(\alpha,\gamma)^{19}Ne$ and $^{21}Na(p,\gamma)^{22}Mg$ are both thought to be key reactions for these processes under explosive astrophysical conditions. In this work, an experiment has been carried out at Louvain-la-Neuve, Belgium, in order to test the feasibility of a measurement of the lifetime of the 4.033 MeV state in ^{19}Ne, which is considered extremely important for the $^{15}O(\alpha,\gamma)^{19}Ne$ reaction. Also, an elastic-scattering experiment was performed using a newly-developed ^{21}Na beam at the ISAC post-accelerated radioactive beam facility in Vancouver, Canada. The experiment represents the first scientific result achieved with this facility. A centre-of-mass energy range of $\approx$ 0.4-1.5 MeV was investigated using a thick-target scan technique utilising polyethylene ($[CH_2]_n$) foils. Data were collected using a silicon charged-particle detector array, enabling the identification of elastic and inelastic resonances in the ^{21}Na+p system. Monte-Carlo simulations were used to estimate the experimental resolution effects present in the experiment. These results were then incorporated into an analysis of the data using a single-channel $\ell = 0$ R-matrix code. An analysis of the data enabled the identification of four states in ^{22}Mg, one of which was previously unobserved. Resonance energies and widths were estimated for each of these states. A comparison of the results with states in the T=1 analogue system was made. The effect a detailed knowledge of these resonances would have on the $^{21}Na(p,\gamma)^{22}Mg$ rate under extreme high temperature conditions was also investigated.

Acknowledgements

I begin by thanking my supervisor Alan Shotter, for his guidance, inspiration and encouragement, without which this thesis would not have been possible. Thanks to my second supervisor, Phil Woods, and to Tom Davinson, for invaluable discussions, suggestions and advice. Thanks to my collaborators at Louvain-la-Neuve; Carmen Angulo, Pierre Leleux, and all the technical staff there, especially Paul Demaret. Thanks to Pierre Descouvement for useful R-matrix discussions. Thanks to my collaborators at TRIUMF; Lothar Buchmann, for his patience and advice, and to Pat Walden for his help with the experiment. Thanks to Bob Laxdal and Matteo Passini for their great beam tuning. A big thanks to Dick Azuma for a productive and friendly collaboration via email, and for his good humour and attitude. Thanks to C. Jeynes, W. Catford and G. Terwagne. Thanks to those at the York group involved with the ^{21}Na+p experiment.

Thanks to all the Edinburgh students, especially Darren, who provided much help and advice. A special mention for Fred Sarazin, who helped a great deal with both experiments and without whose help much of this work would have not been possible. Thanks to Alex Murphy for much advice, and to Gordon Turnbull for technical work.

Love and thanks to my Mum, Anna and Dad for their support of my work during a difficult few years. Thanks to G, Oates and Kmack for keeping things real! Finally, all my love and thanks to my partner Roslynn, for keeping me grounded and being my best friend.

Acknowledgements to the Engineering and Physical Sciences Research Council (EPSRC) for funding of this project.

.... and I suppose I'd better thank Arthur C. Clarke for getting me into physics!

Prelude

As thinking, feeling, Human Beings, we cannot help but look around at our world in wonder. Since the dawning of our collective consciousness as "Mankind", we have posed the questions "How?" and "Why?". Ever representative of the mysteries of existence were the heavens above, the realms of the gods, the untouchable firmament. Our fragile planet has often been described as the cradle of our developing humanity, in which we came to consciousness, and first opened our eyes. Our deepest questions about our and our Universe's origins attempt to describe the beginnings of everything, our conception and birth.

It has taken many thousands of years of conjecture, experiment and observation for us to finally come home, to finally realise that our fragile, living, breathing bodies are wrought from materials originating out in the stars; that the very life-sustaining blood for so long representative of our biological humanity and mortality is built from almost indestructible iron forged deep in the heart of the gargantuan furnaces of supernovae. By our very nature we are made of the stuff of gods. If the Earth is our cradle, then the stars are the wombs from which we were born.

Contents

List of Figures

List of Tables

Chapter 1

Introduction

1.1 Nuclear astrophysics

Nuclear Astrophysics is the study of the nuclear processes which drive the birth, evolution and death of stars. Our current cosmological belief is that the nuclei which make up the majority of matter were first made from nucleons created a short time after the beginning of the Universe, in the expanding fireball we call the *Big-bang*, and later forged in the interiors of stars and stellar explosions.

It is of significant and enduring interest to Mankind to piece together the picture of our evolution from the very first times. In particular, we now know that almost all of the material from which our planet was created was made in a vast series of nuclear reactions inside stars, and spread throughout the interstellar medium via stellar outbursts and energetic explosions. Astrophysicists have modeled these processes in the hope of explaining the isotopic abundances we see today on our Earth, around the Solar system, in

meteoric remains and in astronomical observations of other stellar systems and the interstellar medium, in the hope of tying together a comprehensive understanding of the series of events leading to our present condition. Also of interest are the physical constraints placed on the energy generation and lifetimes of stars resulting from the detailed study of the realm of nuclear interactions, leading to predictive models and observational tools useful in cosmology, the study of the large-scale evolution of the Universe.

In this thesis an experimental investigation of a method to enable the measurement of a crucially important parameter in explosive stellar energy generation is performed. Another experiment utilising cutting-edge radioactive nuclear beam technology is also performed, enabling the study of nuclear parameters significant in highly explosive nucleosynthesis scenarios. Thus this thesis encompasses two of the main areas of Nuclear Astrophysics: energy generation and nucleosynthesis. New information on these parameters is presented and the resultant implications discussed.

The remainder of this chapter will focus on a basic description of what we know and don't know in Nuclear Astrophysics, highlighting some nuclear parameters or reactions of importance. Chapter 2 outlines the theory of nuclear reactions in the stellar environment and presents the R-Matrix theory of nuclear reactions. Chapter 3 describes the investigation of an experimental method to measure a parameter significant to the important $^{15}O(\alpha,\gamma)^{19}Ne$ reaction, which is thought to be a breakout route from the Carbon-Nitrogen-Oxygen cycles in types of hot stars. Chapter 4 outlines the rapid-proton process important for nucleosynthesis in various stellar scenarios and the $^{21}Na(p,\gamma)^{22}Mg$ reaction significant to it. Chapter 5 describes the experimental procedure involved in the measurement of properties of

states in ^{22}Mg via ^{21}Na+p elastic scattering using a newly developed radioactive beam facility. Chapter 6 and 7 are concerned with the methods of analysis and conclusions drawn from this analysis, leaving chapter 8 as a short summary and proposal of possible future work.

We continue now, however, with a description of nucleosynthesis in the Universe beginning with the formation of nucleons and nuclei after the Big-bang.

1.2 Formation of the first nuclei

We begin our summary of the standard Big-bang cosmological model at $t = 10^{-45}s$. At this extremely short time after the Big-bang, the Universe is a ferocious high energy substance seething with particles and radiation, annihilating and popping into existence continuously. The Universe is expanding rapidly, and the forces of nature which are thought to act are gravity and the unified form of the strong-electroweak force, if indeed this does exist[1]. Small-scale quantum fluctuations become the beginning of what will eventually end up as the large-scale structure seen in our present day Universe due to what is termed the *inflationary era*, where the rate of expansion accelerates exponentially (see figure 1.1).

As the Universe expands the strong-nuclear and electroweak forces decouple from each other, and eventually the weak and electromagnetic forces. This is the *Hadron era*, where matter is created and annihilated in a sea of radiation. Here the nucleons and their antiparticles are created via the

[1]Before this time gravity needs to be described by a quantum theory, and is thought to perhaps unify with the other forces at the extremely high energies involved in this regime [1].

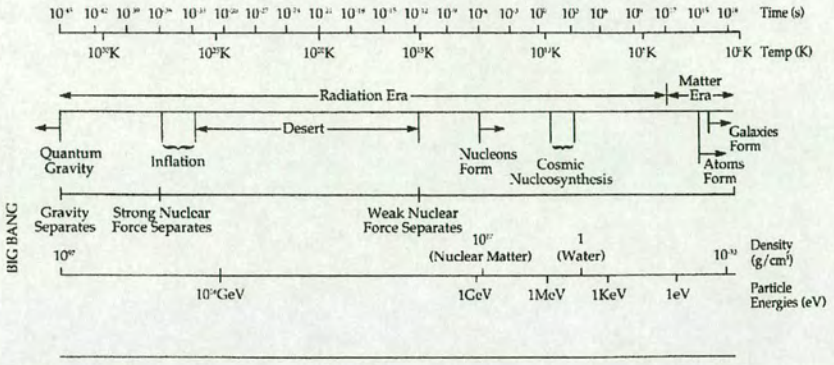

Figure 1.1: *Schematic of the evolution of the Universe. The time axis starts with the Big-bang at the left and ends at the present on the right. [1].*

equilibrium processes:

$$\gamma + \gamma \longleftrightarrow \mathrm{p} + \bar{\mathrm{p}}$$

$$\gamma + \gamma \longleftrightarrow \mathrm{n} + \bar{\mathrm{n}}$$

At this point, there are thought to be almost as many antiparticles as particles, and almost equal numbers of protons as neutrons. As the Universe cools further, the apparent baryon-antibaryon symmetry is broken in a spate of annihilations, leaving the excess of baryons of which our Universe is mostly composed today [2].

The proton-neutron balance is tipped towards favouring protons as the mass difference between the two particles becomes similar to the energies available to the particles for reactions. This begins to occur at around $T = 10^{11}$ K, or $t = 0.01s$ after the Big-bang. As the temperature drops below around $T = 9 \times 10^9$ K, the electron neutrino "decouples", and electron-

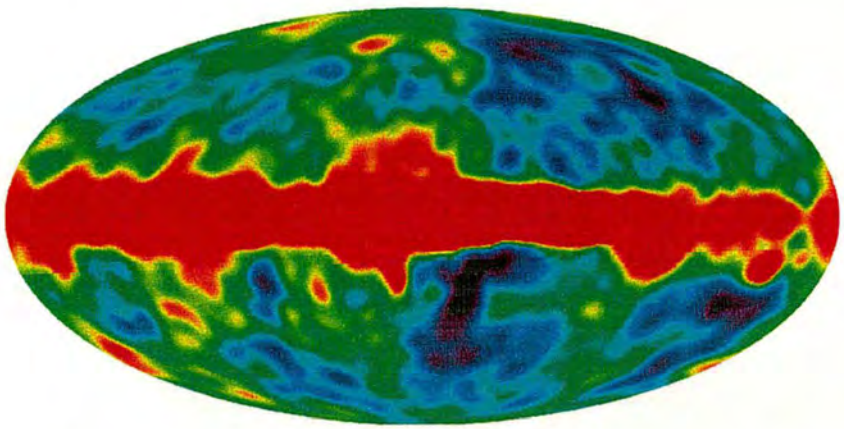

Figure 1.2: *COBE image of the cosmic microwave background, the last scattering surface left over from the matter-radiation decoupling era [4].*

positron annihilation increases [3]. This effectively freezes out the neutron fraction at $\chi_n = n/p \simeq 1/6$, leaving beta-decay as the only remaining neutron removal process. At $T = 10^9$ K nucleosynthesis is sustained with the series of reactions

$$\begin{aligned}
&\mathrm{p} + \mathrm{n} \rightarrow \mathrm{d} + \gamma \\
&\mathrm{d} + \mathrm{d} \rightarrow {}^3\mathrm{He} + \mathrm{n} \\
&{}^3\mathrm{He} + \mathrm{n} \rightarrow \mathrm{t} + \mathrm{p} \\
&\mathrm{d} + \mathrm{d} \rightarrow \mathrm{t} + \mathrm{p} \\
&\mathrm{t} + \mathrm{d} \rightarrow {}^4\mathrm{He} + \mathrm{n}
\end{aligned}$$

with the net result that a quarter of the nucleosynthesised mass is made up from α-particles. The binding energy of the deuteron is low, and so in a hotter earlier Universe it tends to be destroyed quickly, which is why this series of nucleosynthesis reactions can be sustained now. With the

freshly created ^{4}He, reactions can create the isotopes ^{7}Li, and ^{7}Be (which will decay to ^{7}Li). This sets the limits of the products of primeval nucleosynthesis, making ^{7}Li the heaviest primordial isotope produced in any significant quantity. Part of the reason no other species are produced is the mass gaps at A=5 and A=8 where no stable nuclear configurations exist. However, other isotopes in the mass region up to A=8 are thought to be synthesised via a spallation process in the later Universe involving energetic cosmic rays [2].

As further cooling ensues, the recombination of electrons into atomic nuclei occurs and radiation and matter decouple. The Universe then evolves into the matter-dominated era[2]. This is the era which has left its signature in the cosmic microwave background we observe today (see figure 1.2). The structure which began as pre-inflationary fluctuations now comes into play as gravity, the weakest force, becomes important. This allows the galaxies and stars to form, bringing the Universe into the age of stellar nucleosynthesis.

1.3 Star birth

Giant Molecular Clouds containing hydrogen and helium exist in the interstellar medium. The cores of the most dense parts of these clouds tend to be cold ($\approx$10 K) [1], and any heating would arise mostly from neighbouring stars within the region. The gravitational collapse of these clouds can be initiated by supernovae shock waves or by the density increase caused in spiral galaxy arms [5]. Various factors can impede collapse, including the centrifugal force caused by rotation [1], however, once collapse is underway

[2]The matter density becomes larger than the radiation density.

the region starts to heat up due to the conversion of gravitational potential energy into thermal (kinetic) energy. Most of the heat that is generated is lost quickly through radiation, but once the cloud has become dense enough that it becomes opaque to radiation it begins to heat up quickly, usually settling into a period of slow contraction [6].

The now protostar continues to slowly contract until the central region is hot enough and dense enough ($\approx 10^6$ K) for fusion reactions to take place, with the release of a large amount of energy. The outward pressure exerted by the hot core and radiation generated from it becomes enough to balance the inward force of gravity, and collapse is halted. This brings the star onto a stable period of nuclear burning and relative calm called the *Main sequence*, which is the current evolutionary stage of our own Sun.

1.4 Main sequence nucleosynthesis

The first stars to exist in the Universe are termed *population II* stars. These would be composed from the elements which had been created in the Big-bang. To begin with, the star is mostly composed of hydrogen and helium, with only trace amounts of heavier elements. Thermonuclear reactions begin with the proton-proton chain (pp chain), of which there are three stages. The pp-I chain is:

$$\begin{aligned} \mathrm{p} + \mathrm{p} &\longrightarrow \mathrm{d} + \mathrm{e}^+ + \nu_\mathrm{e} \\ \mathrm{d} + \mathrm{p} &\longrightarrow {}^3\mathrm{He} + \gamma \\ {}^3\mathrm{He} + {}^3\mathrm{He} &\longrightarrow {}^4\mathrm{He} + \mathrm{p} + \mathrm{p} \end{aligned}$$

The pp-II chain is:

$$
\begin{aligned}
{}^3\mathrm{He} + {}^4\mathrm{He} &\longrightarrow {}^7\mathrm{Be} + \gamma \\
{}^7\mathrm{Be} + \mathrm{e}^- &\longrightarrow {}^7\mathrm{Li} + \nu_\mathrm{e} \\
{}^7\mathrm{Li} + \mathrm{p} &\longrightarrow {}^4\mathrm{He} + {}^4\mathrm{He}
\end{aligned}
$$

while the pp-III chain is:

$$
\begin{aligned}
\mathrm{p} + {}^7\mathrm{Be} &\longrightarrow {}^8\mathrm{B} + \gamma \\
{}^8\mathrm{B} &\longrightarrow {}^8\mathrm{Be} + \mathrm{e}^+ + \nu_\mathrm{e} \\
{}^8\mathrm{Be} &\longrightarrow {}^4\mathrm{He} + {}^4\mathrm{He}
\end{aligned}
$$

Of these three chains, the pp-I chain generates by far the most energy. The net result of all three chains is the processing of hydrogen into helium. This is the energy source of all main sequence stars. A star will continue burning in this way until the hydrogen fuel in the core begins to run out. When this happens, the star is forced to evolve in any of a number of ways, depending on the star's initial mass, which are described in the next section.

1.5 Evolving stars

As the hydrogen depletes in a Main sequence star, it is replaced in the core by the product of the burning, helium. In most scenarios a thin shell of hydrogen remains burning around the inner helium core, which has become isothermal. Due to the lack of thermal pressure as the hydrogen runs out, the core begins to contract. The hydrogen shell is heated up a little more,

and the envelope of the star, which up until now has not been involved in nuclear burning and so is mostly still hydrogen, begins to expand as it heats [5]. This is the *red giant* phase of evolution. Depending on the mass of the star, the evolution will now proceed in a number of ways.

In a one solar mass star ($\approx 1.99 \times 10^{30}$ kg), the helium core contracts until it becomes an electron degenerate gas. The core cannot contract further once it has become degenerate, and the temperature has reached sufficient levels to allow the helium burning process called the *triple alpha reaction* to occur:

$$^4\mathrm{He} + {}^4\mathrm{He} \longrightarrow {}^8\mathrm{Be} + \gamma$$
$$^8\mathrm{Be} + {}^4\mathrm{He} \longrightarrow {}^{12}\mathrm{C} + \gamma$$

In a degenerate core, because the thermal conductivity is extremely high, as soon as this reaction begins it propagates throughout the core very rapidly, producing what is called the *helium flash*. The star now burns helium in the core until it is exhausted, and a core contraction and envelope expansion phase similar to that during the red giant phase recurs. However, much of the stars outer envelope is thrown off during this phase as the star loses mass in the *planetary nebulae* phase, eventually becoming a *white dwarf*, an electron degenerate star composed mostly of carbon in which all thermonuclear reactions have stopped. It will then proceed to cool slowly, until it finally dies as a cold *black dwarf*.

A star of several solar masses becomes hot enough to keep the degeneracy from occurring in the core at the first red giant phase. Here, the onset of the triple alpha process is slow, as no helium flash occurs. As the

helium is depleted and a carbon core formed, the star goes into the supergiant phase. A succession of core ignition, core exhaustion, contraction and reheating phases occur, burning the ashes of the previous burning stage, until an onion-skin-like structure is reached. The heaviest product which is synthesised in these stars again depends on the mass, but the absolute endpoint is the synthesis of iron, as beyond this mass, all possible reactions are endothermic, ie. consume energy.

1.6 Explosive scenarios

In order to explain the isotopic abundances we see around our Universe, we must take into account explosive stellar scenarios. Two neutron-capture processes, the slow (s) process and the rapid (r) process, are thought to be responsible for the synthesis of the heavy elements beyond iron. The s-process is a non-explosive process, while the r-process is thought to occur only in explosive scenarios. The r-process is thought to be responsible for the nucleosynthesis of the actinides, since these cannot be created via the s-process.

1.6.1 Supernovae type II

The onion-skin picture of a massive evolved star at the end of its fuel burning life leads us into the description of nucleosynthesis of neutron-rich matter. Such a star forms a very dense core as heavier and heavier material is burned. The core becomes degenerate and it is thought that silicon burning then recurs around an iron core. As more heavy material is deposited on the core, electron degeneracy pressure is overcome and the core compresses until

stopped by the pressure exerted by neutron degenerate matter. At this point the core is effectively a neutron star. Depending on how massive the star, it is also possible that gravity could overcome neutron degeneracy pressure and the star becomes a black-hole.

In the neutron core picture however, as material from the mid-layers of the star fall onto the core, they meet with an impassible resistance because of the incompressibility of the degenerate matter. Thus they experience a "hammer-anvil" effect, where the infalling matter bounces of the solid core causing an outward shock wave to rip through the star, blowing all the outer material off the core and into the interstellar medium, leaving the neutron star remnant characteristic of supernovae type II.

During the explosion, there is a large neutrino flux from the core, and also a large flux of neutrons. In this neutron-rich environment, the r- and s-processes can occur, synthesising massive neutron-rich matter via a staggered radiative-capture-beta-decay path (figure 1.3). The s-process can synthesise isotopes up to ^{209}Bi [5]. It is thought that the r-process can account for a large fraction of the nucleosynthesis of neutron-rich isotopes up to the *Uranium island.* The r-process only occurs after collapse of the stars because the density and neutron flux need to be extremely high. During the r-process and s-process, all the nucleosynthesis is from the neutron rich side, leaving the question of where the rare proton-rich stable isotopes which exist in nature are created, for they are impossible to create via neutron processes alone.

It is thought that supernovae type II, although responsible for the synthesis of most of the neutron rich isotopes and their distribution throughout the galaxies, are not responsible for the proton-rich rare isotopes. For these

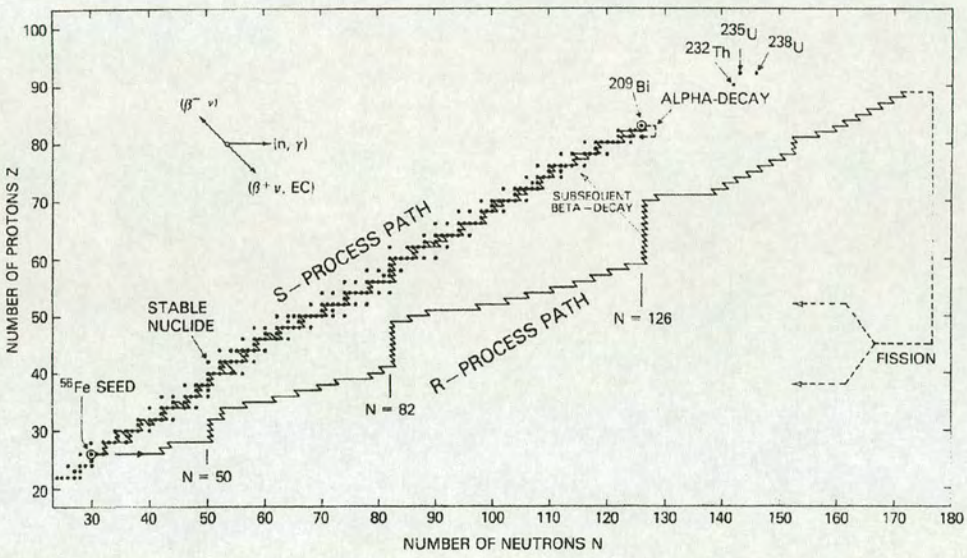

Figure 1.3: *The s-process and r-process neutron capture paths [2].*

nuclides, a very high temperature hydrogen-rich environment would be required, leading into our consideration of stellar binary systems.

1.6.2 Binary systems

Novae

It is observed that up to 50% of stars in the Galaxy are part of binary systems [7], where two stars orbit each other. If the stars are of different mass, usually one of them evolves quicker than the other (normally the more massive the star, the faster it evolves because of its rate of fuel consumption and greater temperature). Because of the centrifugal forces involved in the orbit, the Lagrangian point which normally exists between two massive bodies, where the gravitational pull of each cancels the other out, becomes a pair of extended equipotential surfaces termed *Roche lobes*. When one star evolves such that it is in a stage of expansion, its envelope can fill the Roche lobe where, because of the equal gravitational pull, it can be transferred into the Roche lobe of the smaller star, being captured by its gravitational field and forming an accretion disk around the star. The hydrogen-rich material gradually falls onto the smaller star, forcing it to evolve, until it expands and fills its lobe, transferring material back to the first star. Transfers like this can happen several times until one star becomes a white dwarf.

When the white dwarf's companion eventually expands and material is accreted, we have a situation where hydrogen is deposited on the degenerate surface of the white dwarf in a strong gravitational field. The hydrogen itself becomes degenerate, allowing the temperature to rise without the envelope expanding. Thermonuclear reactions within the carbon-rich white dwarf

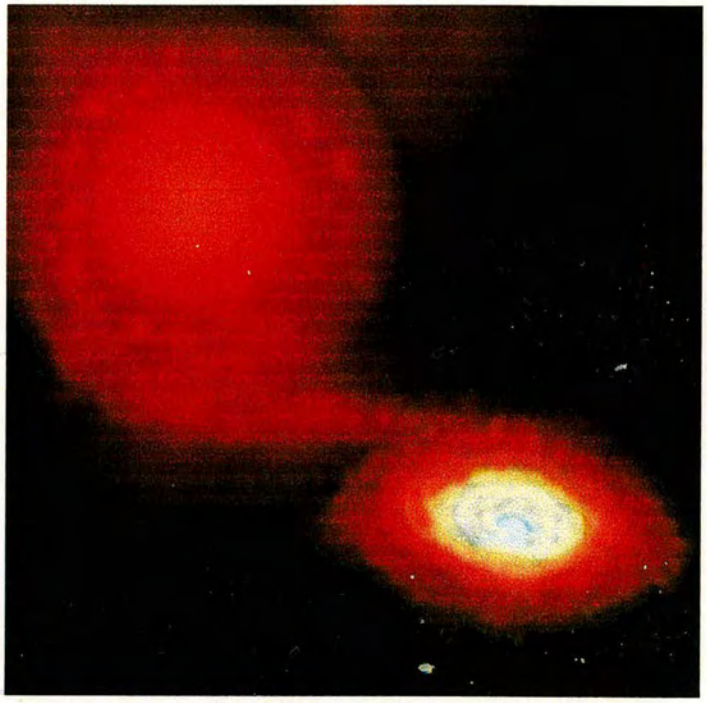

Figure 1.4: *Artist's impression of an accreting white dwarf binary system.*

begin to take place through the Carbon-Nitrogen-Oxygen (CNO) cycles, which will be detailed in the next section. Because the electron-degenerate material cannot expand and cool while it is accreting onto the star, the temperature rises until the degeneracy is suddenly lifted, causing a rapid envelope expansion blowing material out into the interstellar medium. This is a nova (*new star*), so called because of its sudden increase in luminosity during this period.

During nova explosions, proton rich material can be synthesised if the high temperature hydrogen burning CNO cycles can be broken out of, allowing radiative proton-captures up to higher masses. The conditions for the breakout of these cycles are the subject of much Nuclear Astrophysical study, a point which will be discussed in section 1.7. Once synthesised, the nova ejects the proton-rich material into the interstellar medium.

Supernovae type 1a

Under certain circumstances, an accreting white dwarf in a binary system can reach a condition of thermonuclear instability, due to a large accretion rate causing the star to exceed its Chandrasekhar limit[3]. When this happens, as soon as ignition occurs, a massive thermonuclear explosion blasts the entire star apart, in some cases taking the companion with it. Although these explosions distribute material into the interstellar medium, it is composed mostly of the light elements up to iron. Supernovae type 1a are not thought to be important contributors to nucleosynthesis beyond

[3]The Chandrasekhar limit is 1.4 solar masses.

iron.

X-ray binaries

Under certain conditions, binary systems may evolve to the point where, instead of becoming a white dwarf, one of the stars becomes a neutron star. Again, a process of accretion occurs where hydrogen-rich matter falls in towards the neutron star. In such a strong gravitational field, strong X-ray fluxes are generated by the infalling matter, providing the observational X-ray signature of these systems. As material accumulates on the surface of the star, becoming degenerate as in a nova, it can heat to extreme temperatures before degeneracy is lifted. When degeneracy is lifted, the outer layers can explode, similar to a nova. However it is not known whether or not the explosion is powerful enough to throw off the outer layers into the interstellar medium due to the the large gravitational pull of the neutron star. These explosions are characterised by bursts of intense X-ray activity leading to the phenomena being known as *X-ray bursters.*

Since temperatures in X-ray bursters are extremely high, proton-capture nucleosynthesis can proceed at a faster rate, where reactions unimportant in novae can contribute significantly to the production of proton-rich isotopes.

1.7 Hydrogen burning

1.7.1 CNO cycle

In hot enough hydrogen-rich environments, the CNO cycle is the main energy production mechanism. The CNO cycle becomes active in stars at temperatures in excess of around 10^7 K. An initial amount of ^{12}C is required, and

a hydrogen-rich environment.

The Carbon-Nitrogen cycle begins with the radiative proton capture on ^{12}C. The cycle then proceeds via a series of proton-captures and β-decays:

$$^{12}\mathrm{C}(\mathrm{p},\gamma)^{13}\mathrm{N}(\beta^{+}\nu_{\mathrm{e}})^{13}\mathrm{C}(\mathrm{p},\gamma)^{14}\mathrm{N}(\beta^{+}\nu_{\mathrm{e}})^{14}\mathrm{C}(\mathrm{p},\gamma)^{15}\mathrm{N}(\mathrm{p},\alpha)^{12}\mathrm{C}$$

The (p,α) reaction closes the cycle as it is more probable than another proton-capture on ^{15}N. As temperatures rise, the proton-capture on ^{14}N becomes more probable than β-decay, leading to the normal CNO cycle sequence:

$$^{12}\mathrm{C}(\mathrm{p},\gamma)^{13}\mathrm{N}(\beta^{+}\nu_{\mathrm{e}})^{13}\mathrm{C}(\mathrm{p},\gamma)^{14}\mathrm{N}(\mathrm{p},\gamma)^{15}\mathrm{O}(\beta^{+}\nu_{\mathrm{e}})^{15}\mathrm{N}(\mathrm{p},\alpha)^{12}\mathrm{C}$$

The result of this process is the conversion of four protons into a helium nucleus, with the release of energy. The carbon, nitrogen and oxygen nuclei are used as catalysts, their relative abundances remaining unchanged during the process.

1.7.2 The hot CNO cycles

The longest-lived β-decay sections of the CNO cycles are termed *waiting points*, because the cycle must wait at these points before proceeding further if the probability of proton-capture instead of β-decay is still extremely low. As temperatures rise, proton-captures become more probable in a way which is dependent on the nuclear properties in the compound nucleus, a fact which

will be discussed in more detail at a later point in this work. Therefore, just like the Carbon-Nitrogen cycle changes into the CNO cycle via the choice of the path ^{14}N(p,γ)^{15}O instead of ^{14}N($\beta^{+}\nu_{e}$)^{14}C, the CNO cycle can proceed into what is termed the *hot* CNO cycle, via the choice of the path ^{13}N(p,γ)^{14}O at higher temperatures ($0.2 \leq T_9 \leq 0.4$). The hot CNO cycle thus proceeds as:

$$^{12}\mathrm{C(p,\gamma)^{13}N(p,\gamma)^{14}O(\beta^{+}\nu_{e})^{14}N(p,\gamma)^{15}O(\beta^{+}\nu_{e})^{15}N(p,\alpha)^{12}C}$$

The net conversion during this process is again the catalytic transformation of four protons into a helium nucleus.

A "hotter" CNO cycle also exists where the reaction ^{14}O(α,p)^{17}F links into the cycle ^{14}O(α,p)^{17}F(p,γ)^{18}Ne($\beta^{+}\nu_{e}$)^{18}F(p,α)^{15}O. This hotter cycle is thought to occur above 0.4 GK [7].

The longest-lived isotopes (waiting points) in both the hot CNO cycles are ^{14}O ($t_{1/2}$ = 70.6 s), ^{15}O ($t_{1/2}$ = 122.2 s) and ^{18}Ne ($t_{1/2}$ = 1.7 s). These isotopes are therefore important in the consideration of nucleosynthesis because at the hotter temperatures of explosive scenarios, breakout of the hot CNO cycles could occur via radiative proton or alpha capture reactions on these nuclei, leading into a rapid proton-capture process forming proton-rich isotopes.

1.8 Nuclear astrophysical goals

Currently, much research is being done into the reaction rates of various nuclear processes in low energy stellar environments, such as burning in Main sequence stars and red giants. Nuclear cross-sections are measured at the lowest possible experimental energy, and then extrapolations made to stellar energies, which tend to be lower still. An example of this would be the $^{12}C(\alpha,\gamma)^{16}O$ reaction. Also subjects of active research are the higher energy processes of hydrogen burning in the hot CNO cycles and their breakout. The breakout reactions $^{15}O(\alpha,\gamma)^{19}Ne$ and $^{18}Ne(\alpha,p)^{21}Na$ from the hot CNO cycle are currently being paid much experimental attention, and the former reaction is connected to part of this thesis. Of particular importance in Nuclear Astrophysics however, is the study of the specifics of the rapid-proton process. Questions which need to be answered are: What are the key contributing reactions in the rp-process at various temperatures? What are typical rp-process sites: does it occur in X-ray busters only, and if so does the envelope escape into the interstellar medium providing a nucleosynthesis source? Do rp-process reactions occur in novae, where we know the envelope escapes? How much of the nucleosynthesis of proton-rich nuclei can be accounted for by these rp-process scenarios?

One of the key reactions thought to be important to the rp-process is the $^{21}Na(p,\gamma)^{22}Mg$ reaction, as it may provide a link from the Neon-Sodium-Magnesium cycle to the rp-process path as well as influencing the final abundances of certain isotopes in certain stellar scenarios. The latter part of this work will focus on the study of the nucleus ^{22}Mg relevant to this.

Chapter 2

Theory of Thermonuclear Reactions in Stellar Environments

In this chapter the basic equations needed to determine stellar reaction rates are defined, with focus on the specific parameters important in experimental determination of these rates. The R-Matrix theory needed to fit resonant elastic scattering data obtained later in this thesis is outlined.

2.1 Thermonuclear reaction rates

2.1.1 Penetrating the barrier

In stellar environments, nuclear material is synthesised when two nuclei react together to produce a new nuclear species. Thus particle a can react with target particle X to form the product pair b and Y, where Y is the synthesized

nucleus, and b can either be a product particle, an energetic γ-ray, or both.

In stellar nucleosynthesis models, reaction rates are required which define the flow of nuclear material being synthesized. In order to derive an expression for the reaction rate, the cross-section for the reaction at a given energy must be known. Typical solar-type stellar temperatures of around 15×10^6 K correspond to energies of the order 1 keV, while supernovae temperatures can be around 9×10^9 K and correspond to energies of a few hundred keV or more [2]. Coulomb barriers between light particles such as protons and light nuclei are of the order of a few hundred keV to a few MeV. The typical particle energies found in stellar environments are therefore too low to overcome the mutual Coulomb repulsion between them in order to react. However, particles may penetrate the Coulomb barrier through the quantum tunneling phenomenon. This occurs with a characteristic energy dependent probability, parameterised by the *Penetrability*, $\mathcal{P}_\ell$, given by

$$\mathcal{P}_\ell = \frac{kr}{F_\ell^2 + G_\ell^2} \tag{2.1}$$

where k is the wavenumber, r is the separation between the two particles, and F_ℓ and G_ℓ are the regular and irregular solutions to the Coulomb wavefunction for a given relative orbital angular momentum, ℓ. At energies much lower than the Coulomb barrier, the penetration can be approximated [2] as

$$\mathcal{P}_0 \approx \exp\left(-2\pi\eta\right) \tag{2.2}$$

where η is the Sommerfeld parameter given by $\eta = Z_1 Z_2 e^2/\hbar v$, where Z_1 and Z_2 are the charges of the two particles and v is their relative velocity. In this form the penetrability is known as the *Gamow Factor.*

The cross-section for the reaction varies directly with this penetrability factor, as well as with an energy dependent geometrical factor $\pi/k^2 \propto E^{-1}$ accounting for the de-Broglie wavelength of the particle, giving a general variation of the cross-section as

$$\sigma(E) = E^{-1} \exp(-2\pi\eta) S(E) \tag{2.3}$$

The *Astrophysical S-factor* S(E) has been introduced to account for all the specifically nuclear effects and properties which determine the reaction probability. Since experiments at typical stellar energies are extremely difficult due to the low cross-sections involved and the small signal-to-noise ratio, S-factors are used to extrapolate experimental cross-sections measured at higher energies down into the astrophysical regime. This is convenient due to the slow, continuous variation of S(E) with energy when resonances are not present, compared to the other cross-section factors, which vary rapidly with energy.

2.1.2 Thermal stellar properties

The interiors of such stellar systems, comprising of hot nuclear plasma containing different abundances of isotopes, are in dynamic thermal equilibrium, meaning that the velocity distribution of particles follows the Maxwell-Boltzmann relation

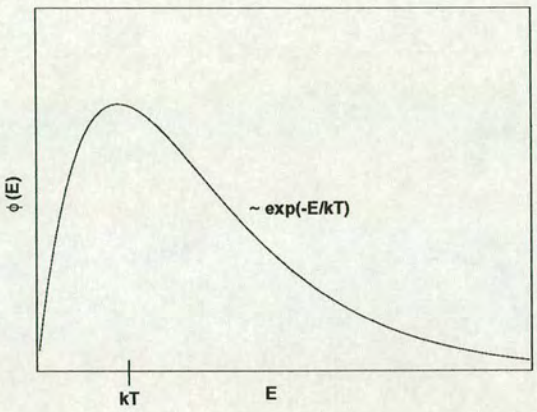

Figure 2.1: *Functional form of Maxwell-Boltzmann energy distribution representative of thermalised stellar interiors.*

$$\phi(v) = 4\pi v^2 \left(\frac{m}{2\pi kT}\right)^{3/2} \exp\left(-\frac{mv^2}{2kT}\right) \tag{2.4}$$

In terms of energy, this can be written

$$\phi(v) \propto E \exp\left(-E/kT\right) \tag{2.5}$$

The functional form of this equation can be seen in figure 2.1. The value E = kT represents the energy at which any given particle has the highest probability of being found in.

2.1.3 Reaction rates

The total reaction rate of a process $a + X \rightarrow b + Y$ in units of $cm^3 s^{-1}$ is given by

$$R = N_a N_X \int_0^\infty \phi(v) v \sigma(v) dv \tag{2.6}$$

where N_a and N_X are the number densities (cm^{-3}) of particles a and X respectively. Thus the rate is a type of convolution of the velocity dependent cross-section and the Maxwell-Boltzmann velocity distribution.

Using relevant velocity transformations, the reaction rate per particle pair can be written in terms of energy as

$$< \sigma v >= \left(\frac{8}{\pi\mu}\right)^{1/2} \frac{1}{(kT)^{3/2}} \int_0^\infty \sigma(E) E \exp\left(-\frac{E}{kT}\right) dE \tag{2.7}$$

where μ is the reduced mass of the particle pair. Inserting the expression for the cross-section of equation 2.3, this integral results in the distribution shown in figure 2.2. Since for non-resonant reactions the S-factor varies smoothly with energy, the exponential penetrability term and the exponential Maxwell-Boltzmann term in the cross-section have the most influence on the integral. The resulting form in figure 2.2 is called the *Gamow Peak*, and represents the region of energies for which the reaction is most probable.

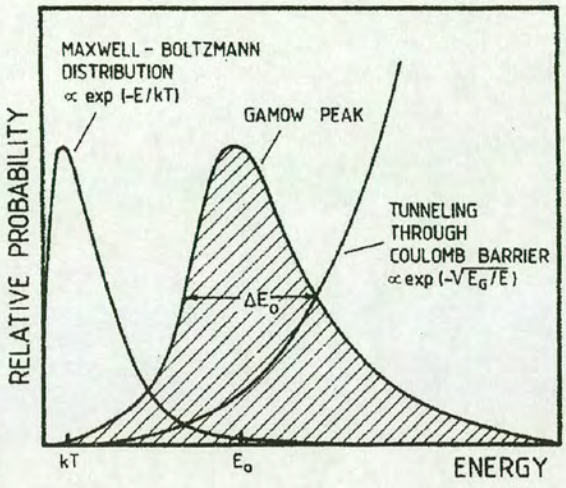

Figure 2.2: *The Gamow Peak (shaded), resulting from convolution of the Maxwell-Boltzmann distribution and the penetrability [2].*

2.1.4 Resonant reactions

The previously derived reaction rate expression relies on the smooth variation of the S-factor with energy for non-resonant (direct) reactions. However, very often, resonant reactions can take place where the two nuclei a and X can fuse together into an excited state of a *Compound Nucleus*, then decay into the product particles b and Y. In this case, when the incident energy is such that the wavefunctions of the incident particle and compound state are well matched, the cross-section for reaction is greatly enhanced around this energy, causing a large increase in the S-factor expression.

The cross-section for a resonance reaction is usually given by the Breit-Wigner Lorentzian form

$$\sigma_{BW}(E) = \omega \frac{\pi}{k^2} \frac{\Gamma_a \Gamma_b}{(E - E_R)^2 + \Gamma^2/4} \tag{2.8}$$

the differential cross-section expression for $\ell = 0$ is simply

$$\frac{d\sigma_{BW}(E)}{d\Omega} = \omega \frac{1}{4k^2} \frac{\Gamma_a \Gamma_b}{(E - E_R)^2 + \Gamma^2/4} \tag{2.9}$$

where ω is the spin-statistical factor $\omega = \frac{(2J+1)}{(2I_1+1)(2I_2+1)}(1 + \delta_{12})$. Γ is the total width of the compound state, and is equivalent[1] to the full-width at half-maximum of the Lorentzian curve. The total width is the sum of the partial widths for all open reaction channels $\Gamma = \Gamma_a + \Gamma_b + ...$, while E_R is the resonance energy, at which the reaction cross-section peaks.

A narrow resonance, where typically $\Gamma/E_R \leq 10\%$, has the specific property of acting like a δ-function in the reaction rate integral of equation 2.7. The resulting reaction rate peaks sharply at the resonance energy of that particular resonance.

When the integral of equation 2.7 is evaluated the functional form of the reaction rate is given by the relationship

$$< \sigma \upsilon > \propto T^{-3/2} \exp\left(-\frac{E_R}{kT}\right) \omega\gamma \tag{2.10}$$

where $\omega\gamma = \omega\Gamma_a\Gamma_b/\Gamma$ is termed the *resonance strength.*

[1]This is true in general for the simplified Breit-Wigner expression but may not be so in other formalisms such as R-Matrix

Low energy narrow resonances in nuclei where reaction particles are well below the Coulomb barrier will tend to have a larger probability of γ-decay than particle decay. In these cases, $\Gamma_\gamma \approx \Gamma$ and therefore the reaction rate of the (p,γ) reaction into that state depends specifically on the partial proton width Γ_p. The reverse can occur where the particle energy is well above the Coulomb energy, where Γ_p will tend to be much larger than Γ_γ, making Γ_γ the dominant factor in the reaction rate. This shows that there are certain scenarios in Nuclear Astrophysics where measurement of one resonance parameter can greatly enhance or definitively pin down the knowledge of a reaction rate.

In the presence of several narrow resonances, the reaction rate simply varies as the sum of the individual resonance contributions:

$$< \sigma v > \propto T^{-3/2} \times \sum_i (\omega\gamma)_i \exp\left(-\frac{E_i}{kT}\right) \tag{2.11}$$

So, in cases where reactions are dominated by the contributions of several narrow resonances, a detailed knowledge of the resonances energies, total widths and partial widths are required in order to calculate the reaction rate. It has been estimated that accuracies of around 20% or so are required in Nuclear Astrophysical calculation in order to meet the limited sensitivity of the models [8]. This work focuses on two specific cases where reaction rates are dominated by narrow resonances, and attempts to measure or deduce individual state properties relevant to these.

2.2 R-Matrix theory of compound nucleus reactions

2.2.1 Reaction channels and the nuclear surface

The R-Matrix formalism is a parameterisation of the properties of compound nucleus reactions. A compound nucleus reaction occurs when two nuclei a and X fuse into an intermediate or *compound* nucleus, C, before decaying into products b and Y. The compound nucleus is usually formed in an excited state, and is normally unstable to particle decay since it was formed via a particle mechanism in the entrance channel. Compound nuclei exist for times much larger than the time it would take for an incident nucleon to cross the nuclear dimensions of the target particle.

The formulation of R-Matrix theory begins with the idea of a *nuclear surface* which defines the volume within which nucleons are considered part of a compound nucleus. This is due to the short-range nature of the strong nuclear force. The volume within this surface contains all the nucleons which make up the compound nucleus, however, once any particles exist outside this surface, they are considered separate entities. In the configuration space of all the possible ways in which the compound nucleus can either be created or decay, the regions outside the nuclear surface are referred to as distinct reaction *channels*. Figure 2.3 shows a schematical representation of this in the case of the compound nucleus $^{8}\mathrm{Be}^{*}$.

In the region outside the nuclear surface, or the *external* region, the nuclear forces between particles are extremely weak. Hence the only contributing forces to the wavefunction properties of particles in the external

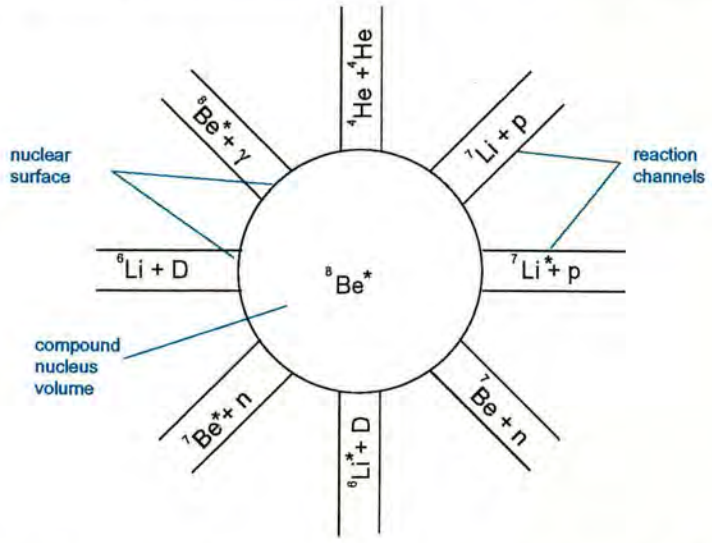

Figure 2.3: *Schematic of the compound nucleus volume defined by the nuclear surface, showing the different reaction channels possible for formation or decay of the system for the example of* $^{8}Be^{*}$. *Adapted from [9].*

region are electromagnetic in nature; the Coulomb repulsion between two like charges and the centrifugal force for particles at non-zero impact parameters. We can then proceed to construct a mathematical description of the qualities of the wavefunctions in the internal and external regions separately.

We define the nuclear surface, the boundary between the internal and external regions, as existing at a radius a_c, the *channel radius*. Outside this boundary, the particle system is described as a superposition of incoming and outgoing waves. Since in the external region no nuclear interactions are operating, the scattering qualities are completely described by factors such as the Coulomb phase shift (which depends on the penetrability, and therefore angular momentum, incident energy and channel radius).

The wavefunctions of the internal region are equated with excited states of the compound nucleus. Because these states eventually decay, they

are quasi-stationary. However, a set of stationary states can be constructed so that the derivative of the internal wavefunction and the wavefunction itself are related by a constant at the channel radius [10].

The relationship between the wavefunctions at the nuclear surface allows the total wavefunction to be constructed. It is this total wavefunction which then relates the description of the reaction properties to the observed cross-sections and angular distributions in reality.

2.2.2 Construction of external and internal wavefunctions

It is useful at this point to use a simplified physical situation in order to illustrate the derivation of the R-Matrix formalism, adding more complicated aspects where necessary, before finally proceeding to define the core complete equations of R-Matrix theory.

The following discussions follow mainly the formalism of refs. [11] and [9], and centre on the discussion of the scattering of a spinless particle by a central potential V(r) to derive the basic equations relating the wavefunctions and properties of the compound nucleus to the R-Matrix parameters.

For a spinless $\ell = 0$ particle scattering from a central potential, we may show the wavefunction of the internal region, Ψ, satisfies the radial Schrödinger equation:

$$\left(-\hbar^2/2m\right)\frac{d^2\Psi}{dr^2} + V(r)\Psi = E\Psi \tag{2.12}$$

However, in reality the nuclear states decay, and therefore do not have

well defined energies (are quasi-stationary). To proceed therefore, a complete set of stationary states are constructed to represent the wavefunction:

$$\Psi = \sum_{\lambda} A_{\lambda} X_{\lambda} \tag{2.13}$$

These stationary states satisfy the Hamiltonian $HX_{\lambda} = E_{\lambda}X_{\lambda}$, where E_{λ} are identified as the energy eigenvalues of the system, with X_{λ} the eigenvectors. To make sure that these states relate directly to the actual quasi-stationary states at the nuclear surface r=a, we introduce a boundary constant, b, giving the boundary condition:

$$\frac{dX_{\lambda}}{dr} + bX_{\lambda}|_{r=a} = 0 \tag{2.14}$$

We then obtain by substitution and integration

$$\left(-\hbar^2/2m\right)\left(\Psi\frac{dX_{\lambda}}{dr} + X_{\lambda}\frac{d\Psi}{dr}\right)_{r=a} = (E - E_{\lambda})\int_0^a X_{\lambda}\Psi dr \tag{2.15}$$

The relation $A_{\lambda} = \int_0^a X_{\lambda}\Psi dr$ and eq. 2.14 can then be used to write

$$A_{\lambda} = \left(-\hbar^2/2m\right) X_{\lambda}(a)\frac{\Psi'(a) + b\Psi(a)}{E - E_{\lambda}} \tag{2.16}$$

We can now substitute this into the expression for $\Psi(r)$ given by eq. 2.13 to get

$$\Psi(r) = G(r,a)\left(\Psi'(a) + b\Psi(a)\right) \tag{2.17}$$

where the Green's function G(r,a) is given by

$$G(r,a) = \left(\hbar^2/2m\right)\sum_{\lambda}\frac{X_\lambda(r)X_\lambda(a)}{E_\lambda - E} \tag{2.18}$$

Now the value of the wavefunction at r=a can be determined via the definition of the *R-function* as the value of the Green's function at r=a:

$$R \equiv G(a,a) = \left(\hbar^2/2m\right)\sum_{\lambda}\frac{X_\lambda^2(a)}{E_\lambda - E} \tag{2.19}$$

If we introduce a new set of parameters γ_λ such that $\gamma_\lambda^2 = (\hbar^2/2m)|X_\lambda|^2$, then the R-function is written

$$R = \sum_{\lambda}\frac{\gamma_\lambda^2}{E_\lambda - E} \tag{2.20}$$

The R-function then relates the internal stationary parameters such as the wavefunctions and eigenenergies to the total wavefunction at the nuclear surface $\Psi(a)$, going some way to enable the description of the system.

The logarithmic derivative of the wavefunction is given by

$$\Psi'(a)/\Psi(a) = (1 - bR)/R \tag{2.21}$$

Knowing the logarithmic derivative of the wavefunction at one point (r=a) for all energies is equivalent to knowing the cross-section for all energies [9].

In the external region the total wavefunction can then be written as a superposition of the incident and outgoing waves, I and O, in the form

$$\Phi_\ell = I_\ell - U_\ell O_\ell \tag{2.22}$$

where U_ℓ is the *collision function*, and we have included the index ℓ to denote the incident orbital angular momentum of the system. The incident and outgoing waves are related to the regular and irregular Coulomb functions F_ℓ and G_ℓ by

$$\begin{aligned} I_\ell &= (G_\ell - iF_\ell)\exp(i\omega_\ell) \\ O_\ell &= (G_\ell + iF_\ell)\exp(-i\omega_\ell) \end{aligned} \tag{2.23}$$

Here, ω_ℓ is the *Coulomb phase shift*, and is given by $\omega_\ell = \sum_{n=1}^{\ell} \tan^{-1}(\eta_\ell/n)$.

Manipulation of incident and outgoing wave equations of unit flux and use of equation 2.22 allow the construction of the *nuclear scattering amplitude*:

$$A(\theta) = \frac{1}{2} i k^{-1} \sum_{\ell} (2\ell + 1)(1 - U_\ell) P_\ell(\cos\theta) \tag{2.24}$$

The differential cross-section is then given by

$$\frac{d\sigma(\theta)}{d\Omega} = |A(\theta)|^2 = \frac{1}{4} k^{-2} \left| \sum_{\ell} (2\ell + 1)(1 - U_\ell) P_\ell(\cos\theta) \right|^2 \tag{2.25}$$

The collision function U_ℓ is related to the R-function and therefore the stationary state qualities by equating the logarithmic derivatives of the internal and external wavefunctions at r=a. This allows U_ℓ to be expressed in terms of a *phase shift*, δ_ℓ, as

$$U_\ell = \exp(2i\delta_\ell) \tag{2.26}$$

where[2]

$$\delta_\ell = \tan^{-1}\left[R_\ell \mathcal{P}_\ell / (1 - R_\ell S_\ell)\right] - \phi_\ell \tag{2.27}$$

Here, $\phi_\ell, \mathcal{P}_\ell$ and S_ℓ are the hard-sphere phase shift, penetrability and energy shift function, respectively, and are given by

[2]The

$$\begin{aligned} \phi_\ell &= \tan^{-1}(F_\ell/G_\ell) \\ \mathcal{P}_\ell &= kr/(F_\ell^2 + G_\ell^2)|_{r=a} \\ S_\ell &= \mathcal{P}_\ell(F_\ell F_\ell' + G_\ell G_\ell') \end{aligned} \tag{2.28}$$

From this point, we have an expression for the differential cross-section which depends on the collision function which in turn depends on the phase shifts associated with Coulomb scattering (ω_ℓ), hard-sphere scattering (ϕ_ℓ), and reaction scattering (R-function). All the information about the stationary states is contained within the R-function, and these states are related to the physical reality by the boundary constant, b, which will be discussed in more detail later.

2.2.3 Multi-channel matrix representation

To extend the above formalism of the R-function to the case where many reaction channels are open and many combinations of spin can contribute to the formation of states of different spin-parity, we introduce matrix notation and a corresponding set of indices. The indices are the set $c = \{\alpha s \nu \ell m\}$. These denote channel, channel spin, channel spin component, orbital angular momentum, and orbital angular momentum component, respectively. The fact that they are grouped together under the index c represents the fact that each reaction channel is uniquely defined by a certain combination of values of these indices. In this representation, the R-function becomes the R-Matrix, whose elements are constructed by

$$R_{cc'} = \sum_{\lambda} \frac{\gamma_{\lambda c'} \gamma_{\lambda c}}{E_\lambda - E} \tag{2.29}$$

where the unprimed and primed indices denote values in the entrance and exit channels respectively. The collision function becomes the collision matrix, and is related to the R-Matrix as [12]

$$U_{cc'} = (k_c r_c)^{1/2} O_c^{-1} (1 - \mathcal{R}\mathcal{L})^{-1} (1 - \mathcal{R}\mathcal{L}^*) I_{c'} (k_{c'} r_{c'})^{-1/2} \tag{2.30}$$

Here, the diagonal matrix $\mathcal{L}_c$ is given by $\mathcal{L}_c \equiv S_c - B_c + i\mathcal{P}_c$, where B_c is the matrix form of the boundary constant.

The expression for the differential cross-section of a process $\alpha \to \alpha'$ as derived in ref. [11] is not stated here but in Appendix B. Instead next we discuss the meaning of various aspects of the R-Matrix formalism and its application to real physical scenarios.

2.2.4 Formal and observed parameters

Because discrete states exist in the compound nucleus, the cross-section is enhanced when the incident wavefunction matches the internal wavefunction, ie. when the energy of the incident particle is closely matched to that of the physical state. This appears as a resonance in the cross-section, whose resonant energy corresponds to the physical energy of the compound nuclear state. A resonance has associated with it a strength and a width, for which the important parameters are the Γ widths defined in section 2.1.4.

These widths are the physical reality of the strength of the resonance; no matter what formalism is used, the experimental data will always show a particular resonance has a certain strength and width corresponding to the real physical properties of the compound nuclear configuration. In contrast, the parameters in the R-Matrix which directly influence the strength of the resonant cross-section, the $\gamma_{\lambda c}$, are identified only as eigenstates of the stationary wavefunctions used to describe the internal region of the compound nucleus.

In the R-Matrix formalism, the external and internal contributions combine in such a way as to make the collision matrix, and therefore the cross-sections, independent of the choice of channel radius or boundary condition. Thus the final cross-section over a resonance can be described as having an observed experimental width, which is the physical reality of the situation, and is related to the internal eigenstate parameter $\gamma_{\lambda c}$ via the channel radius and boundary condition. This is the sense in which R-Matrix is phenomenological in approach. It describes the observed cross-section in terms of parameters Γ analogous to Breit-Wigner widths, without giving any information about the real wavefunctions of the compound nucleus.

The $\gamma_{\lambda c}$ parameters are termed the *reduced widths* and have units of $\sqrt{E}$. Widths with units of energy can be made from them via the relation

$$\tilde{\Gamma}_{\lambda c}(E) = 2\mathcal{P}_c(E)\gamma_{\lambda c}^2 \tag{2.31}$$

this is the *formal width* of the resonance. The definition of resonance energy is that when the state energy E_λ is such that the boundary condition

is equal to the shift function, then the pole energy and resonance energy are equivalent. This leads to the definition of the *observed width* as

$$\Gamma^{o}_{\lambda c}(E) = 2\mathcal{P}_c(E)\gamma^2_{\lambda c}/(1 + \gamma^2_{\lambda c}S'(E)|_{E=E_R}) \tag{2.32}$$

The observed widths are the parameters which are important for astrophysical calculations, and so once a choice of channel radius and boundary condition have been made, and experimental data fitted, steps need to be taken to extract the observed widths and resonance energies from the parameters E_λ and $\gamma^2_{\lambda c}$. The method for doing this is described in chapter 7.

If knowledge is required about the nuclear wavefunctions of the compound nucleus, then the channel radius has to be set to a value which closely resembles the true physical radius of the potential. If the boundary condition is set equal to the shift function at the pole energy, then the corresponding set of formal reduced widths more closely emulate real properties of the wavefunctions. They can then be compared to quantities such as the *Wigner limit*, which will be discussed in chapter 7, in order to predict nuclear structure aspects of the state.

The R-Matrix provides a complete description of scattering cross-sections of resonant reactions in cases where one or more nuclear states can be formed in the compound nucleus via a variety of different mechanisms. One point which R-Matrix theory takes into account which a simple Breit-Wigner resonance does not, is that neighbouring resonances can interfere with each other leading to phase shift modification. However, for the single-level, single-channel, spin-zero case, the R-Matrix representation

reduces to the simple Breit-Wigner equation.

Not taken into account in the R-Matrix theory in this representation are the effects of negative energy channels (sub-threshold resonances), γ-ray emission or excitation, or direct reaction contributions. However, for the particular case in which we wish to apply R-Matrix theory in this work, these effects are either thought to be extremely small or non-existent.

Later in this thesis, the core aspects of R-Matrix theory are modified to be used to fit experimental data of nuclear scattering for an astrophysically important scenario, leading to measurements of the nuclear parameters involved.

Chapter 3

The Lifetime of the 4.033 MeV State of ^{19}Ne

This chapter covers the design and implementation of a test experiment to determine the feasibility of measurement of the lifetime of the 4.033 MeV state of ^{19}Ne, which is of considerable importance to the breakout of the hot-CNO cycle via the $^{15}O(\alpha,\gamma)^{19}Ne$ reaction.

3.1 The role of the $^{15}O(\alpha,\gamma)^{19}Ne$ reaction in the breakout of the hot-CNO cycle

3.1.1 The importance of breakout

In stellar environments with temperatures in excess of 0.2 GK, such as in O-Ne-Mg Novae, the hot-CNO cycle dominates energy generation over other reaction chains. As long as the hot CNO cycle remains unbroken, the net result will always be the catalytic transformation of hydrogen into helium,

with the isotopic abundances of the catalysts carbon, nitrogen and oxygen remaining in equilibrium. It is of considerable interest in Nuclear Astrophysics to determine the routes by which the hot CNO cycle might be broken in certain stellar scenarios, because the beginning of the rapid proton process is reached in this way, resulting in heavy element generation up to as far as ^{68}Se or possibly higher, such as Te [13].

To break the hot CNO cycle, a reaction between either hydrogen or helium, and the CNO catalyst is required which will take the reaction path up to heavier isotopes before the majority of the catalyst isotopes can β^+ decay back into the cycle. Since such a reaction has to essentially compete with β^+ decay for breakout, it is the longest lived proton-rich isotopes in the cycle which are important; the so-called *waiting points.* The longer the lifetime of the radioactive isotope, the more chance it has of reaction with either hydrogen or helium.

In the hot-CNO cycle sequence:

$$^{12}\mathrm{C(p,\gamma)}^{13}\mathrm{N(p,\gamma)}^{14}\mathrm{O}(\beta^+)^{14}\mathrm{N(p,\gamma)}^{15}\mathrm{O}(\beta^+)^{15}\mathrm{N(p,\alpha)}^{12}\mathrm{C}$$

the waiting points are the ^{14}O and ^{15}O radioactive isotopes, both proton-rich. A proton-capture on ^{14}O is forbidden since ^{15}F has a proton decay width of about 1 MeV. However, the nature of states in ^{18}Ne (i.e. ^{14}O + α) above the α-threshold means that the $^{14}\mathrm{O}(\alpha,\mathrm{p})^{17}\mathrm{F}$ reaction becomes possible at around 0.4 GK. This links to the next part of the hot-CNO cycle path, and consequently ^{18}Ne and ^{18}F are brought into the cycle via the chain:

$$^{14}\mathrm{O}(\alpha,\mathrm{p})^{17}\mathrm{F(p,\gamma)}^{18}\mathrm{Ne}(\beta^+)^{18}\mathrm{F}$$

where ^{18}Ne is now also a waiting point of the cycle due to its reasonably long lifetime (1.7 s).

If the proton-capture reaction ^{18}F(p,γ) were favourable, then ^{19}Ne would be formed. This would then β^+-decay to ^{19}F and a subsequent proton-capture would take it to stable ^{20}Ne, hence the cycle would be broken. This is actually not the case, as the states in ^{19}Ne which are formed are above the α-threshold, allowing the ^{18}F(p,α)^{15}O reaction to occur, a fact which is not usually the case for Z_{even}-1,N=Z_{even}-1 nuclei below cesium [14], and so the cycle is taken back to one of its waiting points. Proton-capture on ^{15}O is hindered in the same way as on ^{14}O, and this leaves the waiting point ^{18}Ne(β^+). The proton-rich nucleus ^{19}Na is very likely to proton decay compared with its γ-decay, so that the reaction ^{18}Ne(p,γ)^{19}Na does not compete.

3.1.2 The breakout route $^{15}O(\alpha,\gamma)^{19}Ne$

Since all conceivable proton-capture routes out of the hot-CNO cycle are either impossible or unlikely, only α-induced reactions are possible instigators of breakout, helium being the next most abundant fuel to hydrogen. The two possible waiting-point nuclei α-capture reactions are then $^{15}O(\alpha,\gamma)^{19}Ne$ and ^{18}Ne(α,p)^{21}Na. The ^{18}Ne(α,p)^{21}Na reaction relies first on the ^{14}O(α,p)^{17}F link to the second part of the hot-CNO cycle, and then requires temperatures in excess of 0.6 GK to become important [15], but at lower temperatures, the $^{15}O(\alpha,\gamma)^{19}Ne$ is thought to dominate the breakout path. This reaction in particular is important in a number of ways. Firstly, the reaction will lead to a proton-capture on ^{19}Ne and consequently ^{20}Na will be formed, β-decaying to ^{20}Ne. This is stable, and from this point, there is absolutely no way that the seed nuclei can be taken back into the CNO cycle, with the result that heavier isotopes above mass 20 are the main

products of explosive hydrogen burning. Secondly, the energy generation of the rapid-proton process above mass 20 is thought to exceed that of the HCNO cycle by a factor of one hundred [16] under certain conditions. This has consequences for the modeling of hot stellar scenarios.

3.2 The structure of ^{19}Ne relevant to the $^{15}O(\alpha,\gamma)^{19}Ne$ reaction rate

3.2.1 The states in ^{19}Ne of Astrophysical interest

The α-particle threshold in ^{19}Ne corresponds to an excitation energy of 3.529 MeV, therefore, the structure of ^{19}Ne around this energy determines the low temperature reaction rate of $^{15}O(\alpha,\gamma)^{19}Ne$. It is thought that the direct reaction mechanism does not contribute significantly to this reaction rate [17], and that the reaction proceeds by the contribution of resonances corresponding to the states above α-threshold in ^{19}Ne.

The structure of ^{19}Ne above the α-threshold has been studied using many methods over the years. Initially, evidence for states at E_x=3.841 MeV and E_x=4.013 MeV was found using the reaction $^{20}Ne(^3He,^4He)^{19}Ne$ [18], while a restudy using the reaction $^{17}O(^3He,n)^{19}Ne$ also found evidence for a state at 4.01 MeV, and a state at 3.7 MeV although the existence of the latter was uncertain [19]. A further study again using the $^{20}Ne+^3He$ transfer reaction [20] measured the first state above threshold as 4.036 MeV, as the experiment failed to yield any evidence for a state below this value, even though the experiment was performed at a higher bombarding energy than the previous $^{20}Ne+^3He$ study.

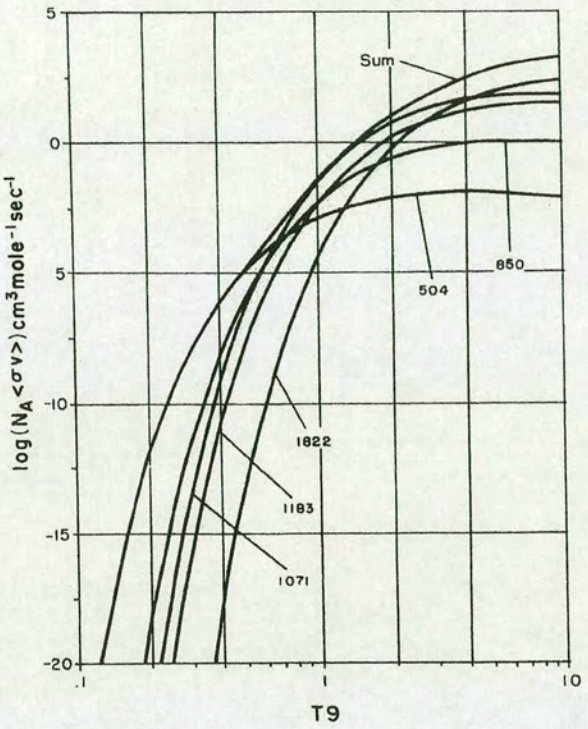

Figure 3.1: *Reaction rates for the $^{15}O(\alpha,\gamma)^{19}Ne$ reaction as calculated in ref. [16], showing the contribution of individual resonances.*

Other states considered to be the major contributors to the $^{15}O(\alpha,\gamma)^{19}Ne$ reaction under astrophysical conditions are the levels at E_x = 4.379 MeV, 4.549 MeV, 4.600 MeV, 4.712 MeV and 5.092 MeV. These have resonance strengths, $\omega\gamma$, ranging between $\sim$ 5 meV and $\sim$ 200 meV [16]. However, the first state above threshold mentioned previously is considered the most important state under low-temperature astrophysical conditions, for reasons that will be explained in the next section. The following part of this work will concentrate on this state.

3.2.2 Properties of the 4.033 MeV state in ^{19}Ne

A spin-parity assignment of $3/2^+$ was given to the 4.036 MeV state as a result of DWBA fits in the ^{20}Ne(^{3}He,^{4}He)^{19}Ne experiment [20], and this low spin means that the ^{15}O$(\alpha,\gamma)^{19}$Ne reaction could occur with significant strength via a low orbital angular momentum α-capture to this state[1] since the resonant energy is low. The state energy has been remeasured as 4032.9 ± 4 keV in an experiment using the reaction^{19}F(^{3}He,t)^{19}Ne [16]. This energy corresponds to a centre-of-mass energy of 0.504 MeV in the ^{15}O+α system, and this resonance would dominate the reaction rate below 0.7 GK [16]. Ideally the reaction rate should be measured experimentally, but due to the extremely small cross-section of the reaction, the direct measurement is difficult. Good quality radioactive ^{15}O beams are still under development, as are the experimental facilities, such as recoil separators, needed to perform this direct measurement [21]. The cross-section is thought to be extremely small for this resonance due to the magnitude of the α-branching ratio $\Gamma_\alpha/\Gamma_{tot}$, which is thought to be of the order 10^{-4} based on the equivalent resonant state properties in the mirror nucleus ^{19}F (measurement made on ^{15}N$(\alpha,\gamma)^{19}$F resonance strengths) [22]. Current reaction rate estimates for the ^{15}O$(\alpha,\gamma)^{19}$Ne(4.033) resonance are usually based on this analogue assignment [16] although several experiments have attempted to measure this rate indirectly, the methodology of which will be discussed in the next section.

[1]The reaction pair ^{15}O ($J^\pi=\frac{1}{2}^-$) + α ($J^\pi=0^+$) can proceed to a ^{19}Ne ($\frac{3}{2}^+$) state via $\ell = 1$ capture

3.3 Indirect measurement of the $^{15}O(\alpha,\gamma)^{19}Ne(4.033)$ reaction rate

3.3.1 Systematics of the reaction rate

The expression for the resonant reaction rate given by equation 2.10 contains the resonance strength $\omega\gamma$, which for the $^{15}O(\alpha,\gamma)^{19}Ne$ reaction will be given by:

$$\omega\gamma = \omega \times \frac{\Gamma_\alpha \Gamma_\gamma}{\Gamma_{tot}}$$

Because Γ_α is thought to be much smaller than Γ_γ, the approximation $\Gamma_{tot} \approx \Gamma_\gamma$ can be made, and therefore the reaction rate will vary directly as Γ_α. Thus a measurement of Γ_α can be used to estimate the reaction rate, regardless of the absolute value of Γ_{tot}. This has the implication that any measurement of both the α-branching ratio *and* the γ-decay width will yield a number which can be used to directly estimate the reaction rate.

3.3.2 Measurement of the α-branching ratio

The α-branching ratio can be written as $\Gamma_\alpha/\Gamma_\gamma$ using the approximation above, and so can be measured by using a reaction to populate the relevant state in ^{19}Ne and detecting coincident ^{15}O recoils and ejected α-particles as a ratio to the total excitation of the 4.033 MeV state in ^{19}Ne nuclei. The ratio between these populations, folded in with the experimental efficiency,

will give the branching ratio[2], $\Gamma_\alpha/\Gamma_\gamma$. The problems in measuring this ratio relate to finding a suitable populating reaction with a high yield of the 4.033 MeV state, and having sensitive enough experimental setups to efficiently detect the decay products ^{15}O and α.

Several experiments have been proposed or tested to measure this branching ratio using a variety of different populating reactions, for example the $^{18}Ne(d,p)^{19}Ne$ reaction [23][24], the $^{20}Ne(^3He,^4He)^{19}Ne$ reaction [25], and the $^9Be(^{18}Ne,2\alpha)^{19}Ne$ reaction [26]. The first experimental constraints have been put on this branching ratio recently as $\Gamma_\alpha/\Gamma_\gamma \leq 5 \times 10^{-4}$ [25].

3.3.3 Measurement of the γ-decay width

Although much attention has been paid to measurement of the branching ratio, less has been paid to the γ-decay width although there are and have been attempts at measurement of this parameter [27].

It is important that the lifetime of the state (related to the γ-decay width by $\tau = \hbar/\Gamma_\gamma$) be measured explicitly, via an independent experimental method, so that the value can be combined with data from branching ratio experiments in order to yield a good solid estimate of the α-width of the state.

---

[2]Each ^{19}Ne nucleus detected has proceeded via γ-decay of the 4.033 MeV state (the kinematics of the ^{19}Ne will tag the excited state) while the pair of ^{15}O and α nuclei will have proceeded via α-decay of the state (again with their kinematics tagging the state), so that the experimental ratio measured is actually $\Gamma_\alpha/\Gamma_\gamma$

3.4 Design of a lifetime measurement experiment for the 4.033 MeV state in ^{19}Ne

3.4.1 The Doppler-shift attenuation method

The estimated γ-width of the 4.033 MeV state in ^{19}Ne is 73±41 meV [16], based on measurements of the analogue $3/2^+$ state at 3.907 MeV in ^{19}F [28][29]. This corresponds to a mean lifetime of around 9 femtoseconds.

The usual method for measurement of such small γ-ray lifetimes is the **Doppler Shift Attenuation Method** (DSAM). It is based around the premise that the energy of a γ-ray measured in the lab will be Doppler-shifted depending on the lab velocity of the excited nucleus which has emitted it. A full description of the method is described in Appendix A.

In this experiment, it was chosen to use an implanted target method where a range of different stopping materials are implanted with a thin layer of target material. The beam reacts with the target material producing the required recoil, which decays in the stopping material whilst decelerating, leading to a measurement of the mean lifetime via the analysis of the Doppler-shifted γ-ray lineshapes as described in Appendix A. In this particular case we chose to use the *centroid method*, where the centroids of the Doppler-shifted γ-ray peaks from a range of different stopping materials give a lifetime estimate using the relations described in Appendix A.

It has been found in previous investigations that the centroid method of determining the lifetime is more accurate for small lifetimes. Experiments using the centroid method over different stopping materials have successfully measured fast lifetimes of 2.2 fs with around 30% error [30].

3.4.2 The $^{3}He(^{20}Ne,^{4}He)^{19}Ne$ reaction

In order to design an experiment utilising the implanted target technique mentioned above, it is necessary to determine a suitable populating reaction for the nuclear state of interest. The $^{20}Ne(^{3}He,^{4}He)^{19}Ne$ reaction has been studied in ref. [20], using a ^{3}He beam at incident energy 15 MeV on a windowless gas cell containing ^{20}Ne. Angular distributions between 0° and 90° in the centre-of-mass were measured for states in ^{19}Ne up to E_x=7.064 MeV. To date this is the most thorough experimental cross-section data available for this reaction. This introduces the possibility of the use of the inverse kinematics reaction $^{3}He(^{20}Ne,^{4}He)^{19}Ne$ to populate the 4.033 MeV state in ^{19}Ne. This would be an advantageous reaction to use because estimates on the event rate can be made using the cross-section data, and the high recoil velocities involved in an inverse kinematics reaction are suited to a DSAM measurement. The target nucleus ^{3}He is gaseous at S.T.P, and therefore would be suited to implantation in a range of stopping materials, in analogy to the implantation of ^{4}He into metals in the DSAM experiments in refs. [31] [32]. It was decided to utilise this reaction for the DSAM experiment of the 4.033 MeV state lifetime.

The 15 MeV ^{3}He beam energy corresponds to a centre-of-mass energy in the $^{20}Ne+^{3}He$ frame of ~13.03 MeV, which translates into an inverse kinematics ^{20}Ne beam energy of ~100 MeV. The differential cross-section of the $^{20}Ne(^{3}He,^{4}He)^{19}Ne(4.033)$ reaction at $\theta_{cm} = 0°$ is ≈0.4 mb/sr and falls off rapidly with increasing angle. The DWBA fits to the experimental data in ref. [20] suggest that the reaction is a direct process due to the characteristic maxima and minima in the angular distribution. Although no

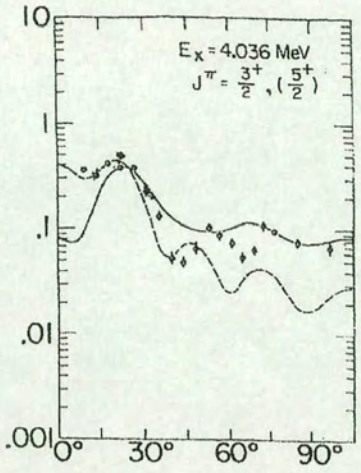

Figure 3.2: *The differential cross section (centre-of-mass) for the 4.033 MeV state of* ^{19}Ne *in the reaction* $^{20}Ne(^3He,^4He)^{19}Ne$. *Taken from ref. [20]. The solid and dashed lines show DWBA fits for* $J^\pi = 3/2^+, 5/2^+$ *respectively.*

angular data exist for the region $\theta_{cm} \geq 90°$, the data may be extrapolated to $\theta_{cm} = 180°$ to estimate the value of the differential cross-section at forward lab angles in inverse kinematics.

Figure 3.2 shows the differential cross-section between 0° and 90° in the centre-of-mass system for the 4.033 MeV state as measured in ref. [20]. When we transform into the inverse kinematics frame, there is an inversion of the z-axis, ie. the direction of the beam. This transforms the angles of the scattered particles by the relation

$$\theta_{CM,I} = 180° - \theta_{CM,N} \tag{3.1}$$

where $\theta_{CM,I}$ and $\theta_{CM,N}$ are the angles of the scattered particles in

inverse and normal kinematics reactions respectively.

An inverse kinematics reaction also provides us with an essential feature for the Doppler Shift Attenuation Method: a fast recoil velocity. This means that the recoiling excited ^{19}Ne nucleus travels a large distance in the stopping material before it decays. The decceleration in the stopping material will therefore be significant, giving a Doppler shift attenuation large enough to measure. It has been reported in ref. [32] that for heavy-ion reactions which involve recoil velocities with $\beta \approx 0.03$, lifetimes can be measured with sensitivities of around 1 fs. A recoil ^{19}Ne nucleus at $\theta_{lab} = 0°$ from the equivalent inverse reaction to that used in ref. [20] (^{20}Ne beam energy of 100 MeV) would have a recoil velocity of around $\beta \approx 0.07$, which would be less efficient than the velocities mentioned above because although a large distance is travelled in a short time, the stopping power will be less because of the high energy. However the main reason for this being too high a beam energy is the fact that there may be γ-ray contamination from a fusion-evaporation background caused by reactions on the stopping material. Because it was decided that the centroid method was to be used to measure the lifetime over a number of stopping materials, the beam energy of the reaction had to be chosen carefully so as to minimise the background from fusion on the stopping materials, yet have a suitable recoil velocity for the DSAM measurement, and suitable centre-of-mass energy for the formation of the state of interest. The DSAM experiment of ref. [30] used foils of Magnesium, Aluminium, Tantalum and Gold as its stopping media. However, the beam energies used were only 1.657 and 1.663 MeV/nucleon which were deemed suitable for the formation of the state of interest at 1.04 MeV. Since our study involves an excited state energy of 4.033 MeV, the centre-of-

mass energy of the reaction needs to be high enough to form this state. The threshold beam energy for the reaction ^{20}Ne(^{3}He,^{4}He)^{19}Ne(4.033) is 2.439 MeV, ie. this reaction is energetically possible for all beam energies above this value. However, we must also ensure that the centre-of-mass energy of the reaction is above the Coulomb barrier for the system ^{20}Ne + ^{3}He. Using the simple Coulomb equation for the size of the Coulomb potential barrier:

$$V_C = 1.44 \frac{Z_1 Z_2}{r_n (A_1^{1/3} + A_2^{1/3})} \tag{3.2}$$

where r_n is the nuclear radius ($\approx$ 1.22 fm), the barrier for ^{20}Ne + ^{3}He is roughly 5.7 MeV. Therefore a ^{20}Ne beam energy greater than 43.48 MeV would be above the barrier. The Coulomb barriers for the materials used in the experiment of ref. [30] are tabulated in table 3.1, along with various other metals. It can be seen from the table that a beam energy of 100 MeV would rule out the use of some of these metals in the experiment because fusion reactions on the stopping material would occur. However, a beam energy of 50 MeV would only rule out the use of Magnesium and Aluminium whilst being above the Coulomb barrier for ^{20}Ne + ^{3}He. A recoiling ^{19}Ne nucleus from the reaction at 0° would have a velocity $\beta \approx 0.05$, more like the velocities used in the study of ref. [30]. A 50 MeV beam energy was then chosen to be used in the experiment.

A suitable set of stopping materials had to be chosen for the experiment. Gold and Tantalum were considered as in refs. [30] [31], as also was Nickel, used in ref. [31]. In addition, Tin and Tungsten were also considered. Table 3.2 shows the stopping powers and some elemental properties for these

Material	V_C (MeV)	E_{lab} (MeV)
Mg	25.3	47.5
Al	26.9	47.8
Sn	77.2	90.7
Ta	102.9	114.9
W	104.0	115.8
Au	109.3	120.9

Table 3.1: *Approximate values of the Coulomb barrier and corresponding equivalent incident lab energies for ^{20}Ne on various metals.*

materials for an incident 50 MeV ^{20}Ne beam. 50 MeV incident energy is substantially below the Coulomb barrier for all these materials. A large range of stopping powers is covered using these materials, all of which are available in thin[3], self supported foils with purities of the order of 99.9% [4] [33]. Tin is an exceptional example as it has a relatively low atomic density compared to its atomic mass, making the stopping power low, yet remaining accessible to the experiment by having a high Coulomb barrier. It was decided to implant a selection of these foils with ^{3}He ions in order to perform a test experiment for the reaction ^{3}He(^{20}Ne,^{4}He)^{19}Ne.

The methods of implantation of the targets with ^{3}He, and the subsequent foil analyses to determine the actual ^{3}He content, are described in detail in Appendix A.

[3]'Thin' in this context refers to thicknesses of the order of a few micrometres.

[4]With the exception of Tin, which is available from suppliers with a standard maximum purity of 99.75%

Material	Stopping power (MeV/mm)	Density (g/cm^2)	Z, A
Ni	4929	8.912	28, 58
Sn	2880	7.287	50, 120
Ta	5349	16.4	73, 181
W	6167	19.3	74, 184
Au	5975	19.282	79, 197

Table 3.2: *Stopping powers (for 50 MeV incident ^{20}Ne) and elemental properties of various target materials.*

3.5 Experimental technique and results

3.5.1 Experimental setup

The setup for the first test experiment of the ^{3}He(^{20}Ne,^{4}He)^{19}Ne reaction consisted of a large cuboid shaped scattering chamber into which were recessed two cylindrical wells at 0° and 90° to the beam direction. Into the well at 0° was inserted a 70% HPGe detector, while into the other well a 45% HPGe detector with a Berylium window was placed. The 0° detector sat at a distance of $\sim$ 60 mm from the target position with the active volume subtending a total angle of approximately 60° while the 90° detector was at a distance of $\sim$ 45 mm subtending a total angle of around 80°. At the target position a laterally mobile target ladder contained three target positions mounted with either a Tungsten or Aluminium implanted foil, a Tungsten or Aluminium unimplanted foil and a blank target frame. At 0° directly behind the target sat a ΔE-E particle telescope consisting of a 65 μm p-n junction Silicon detector and a 900 mm^2 area, 700 μm thick fully depleted PIPS detector. A 12 μm thick Tantalum beam stop foil was placed between the target and the telescope, protecting the Silicon detectors, yet allowing α particles from the reaction of interest to be transmitted. A 0.8 mm diameter

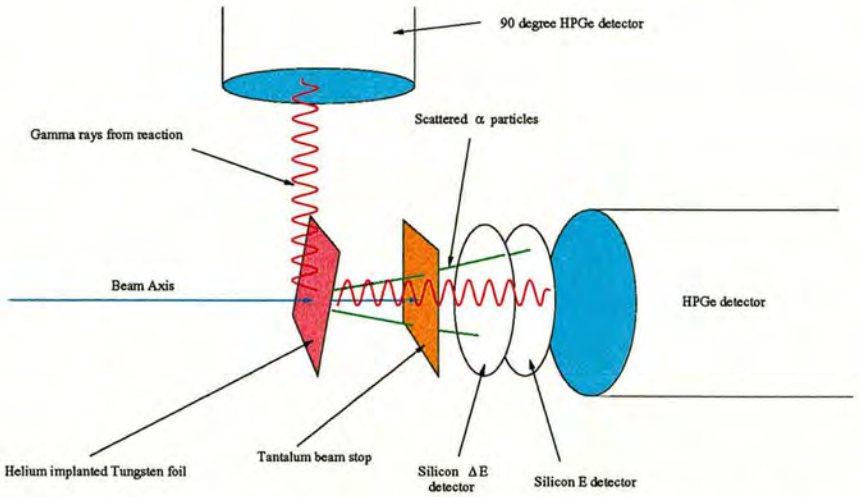

Figure 3.3: *Schematic of the $^{3}He(^{20}Ne,^{4}He)^{19}Ne$ test experiment setup.*

Gold collimator was positioned approximately 60 mm in front of the target ladder, from which the current was measured. The current was also taken off the Tantalum beam dump foil. Figure 3.3 shows a schematic of the setup.

The 50 MeV ^{20}Ne beam was produced using the CYCLONE[5] 110 cyclotron facility at Louvain-la-Neuve, Belgium. Neon gas of natural isotopic abundance is ionised in an ECR ion-source and ions are extracted using an electrostatic field. These are then injected into the centre of the cyclotron, and ^{20}Ne ions of charge state 4^{+} are accelerated up to the required energy, extracted using a 150 kV/cm electrostatic plate device and transported to the experimental station prior to which several quadrupole and dipole magnets ensure correct focussing, steering and transmission of the beam. The beam focus and steering is checked using a thermoluminescent Quartz tar-

[5]The CYCLONE 110 cyclotron is capable of accelerating ions up to energies of $110Q^2/M$, where Q is the charge state and M is the mass [34].

get positioned at approximately 1 metre in front of the target position. The estimated beam spot size at the Quartz position was around 10 mm in diameter. The beam transmission into the scattering chamber is checked by minimising the current on the Gold collimator and maximising the current on the beam dump. Currents of an average of 10 nA (electrical) were used during the experiment, which corresponds to around 1.5×10^{10} particles/s, using 4^+ charge state.

During this experiment, approximately 13 hours were spent with beam on the ^{3}He implanted Tungsten target. A further 6 hours approximately were spent with an unimplanted Tungsten target at the target position. Calibration runs were performed using standard ^{60}Co, ^{88}Y, and ^{22}Na γ-ray line sources, while data were also taken with an Americium-Berylium neutron[6] source which has a high energy γ-ray at 4.439 MeV. A standard Am-Cu-Pu α-particle source was used to calibrate the particle detectors.

3.5.2 Results

In the experimental data, certain aspects have to be identified sequentially to check the success of the reaction in populating excited states of ^{19}Ne. Firstly, α-particles from the reaction have to be identified. Secondly, γ-ray peaks associated with these events have to be found and related to possible decays of an excited ^{19}Ne nucleus. Also, a good check for the γ-ray data is to see the decay from the first excited state of ^{20}Ne, which should be populated via the Coulomb excitation of the beam in the Tantalum stopping foil.

[6]The α-particles resultant from the decay of ^{241}Am into ^{237}Np and then to ^{233}Pa combine with the Berylium in the source by the reaction ^{9}Be(α,nγ)^{12}C, where the γ-ray is from the first excited state of ^{12}C.

During data reduction, the calibrated and gain-matched particle detector data is used to construct a 2-dimensional particle identification spectrum. For each valid event (defined as an event for which data is contained in both the ΔE and E detectors and in either of the Germanium detectors), the total energy E+ΔE is plotted against the particle identification relation, given by[7]

$$(\Delta E + E)^n - E^n \propto TM^{n-1}Z^2$$

where T is the thickness of the ΔE detector, M is the mass of the projectile, and Z the charge of the projectile.

Figure 3.4 shows the 2-dimensional particle identification spectrum representing a large percentage of the total data collected on an implanted Tungsten target. Clearly seen are the scattered ^{3}He nuclei as well as the scattered ^{4}He, some of which are the result of the reaction ^{3}He(^{20}Ne,^{4}He)^{19}Ne.

Figure 3.5 shows sections of the raw Germanium detector data for both the 0° and the 90° positions, compared with the corresponding data when no ^{3}He was present in the target. Clearly seen are the 511 keV γ-rays ever-present in the radiation background, as well as some Coulomb excitation peaks from the Tungsten target and Tantalum beam stop. These peaks have been identified as the transitions: **A** = ^{182}W $4^+ \rightarrow 2^+$ (229.322 keV), **B** = ^{184}W $4^+ \rightarrow 2^+$ (252.848 keV), **C** = ^{186}W $4^+ \rightarrow 2^+$ (273.97 keV) and **D** = ^{181}Ta $\frac{11}{2}^+ \rightarrow \frac{7}{2}^+$ (301.62 keV). The peak at **X** is a candidate for the ^{19}Ne first

[7]This relation can be derived from the semi-empirical range formula for light ions in Silicon, where $R(E) = a(M,Z)E^n$ [35]

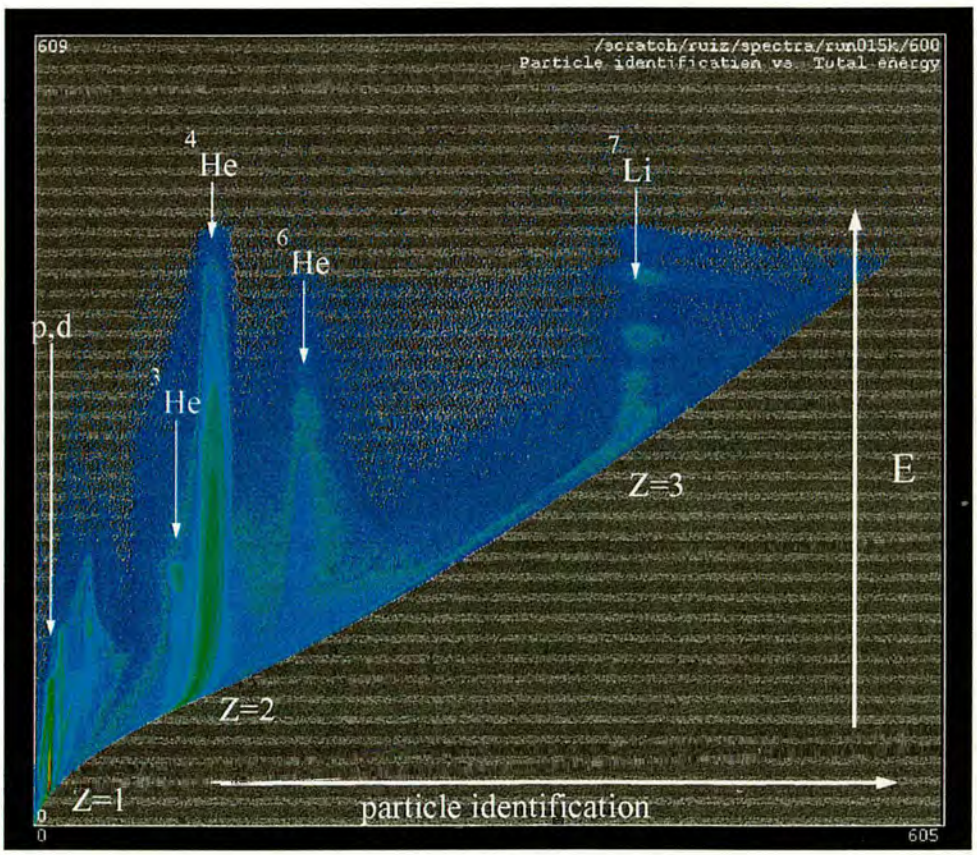

Figure 3.4: *Particle identification spectrum.*

excited state decay of 238.27 keV. To ascertain which γ-rays come from the reaction of interest, a 1-dimensional gate is put on the particle-identification variable ensuring only α-particle associated events are incremented into the relevant γ-ray spectra.

Figure 3.6 shows the resulting low energy sections of the α-particle coincident γ-ray spectra. The identification of the decays from the first and second excited states of ^{19}Ne have been made. The first excited state of ^{19}Ne has an energy of 238.27 keV, and a mean lifetime of 18 nanoseconds. Because the excited ^{19}Ne nucleus travels a large distance in this time, it will have decelerated to rest in the Tantalum beam stop before it decays. Therefore the γ-ray from this decay has no Doppler shift and is observed at its full energy. The peak should therefore have the same profile in each detector. The second excited state of ^{19}Ne has an energy of 275.09 keV, and a mean lifetime of 42.6 picoseconds. Here the recoil nucleus should partially make it out of the target and into the Tantalum before decaying. We therefore expect to see a Doppler-broadened peak at 0°, and in fact what is observed is a double peak-like structure which may consist of a stop-peak and the Doppler-shifted component.

Table 3.3 lists the excited states that might be populated in this experiment up to 4197.1 keV with their corresponding γ-decay energies and intensities. A Monte Carlo calculation was made using the cross-sections of ref. [20] for the ^{3}He(^{20}Ne,^{4}He)^{19}Ne reaction at an energy corresponding to twice that of this experiment, in order to estimate the relative intensities of the peaks from ^{19}Ne decay. The simulation took into account the branching ratios for the decays and Germanium detector efficiency. Figure 3.7 shows

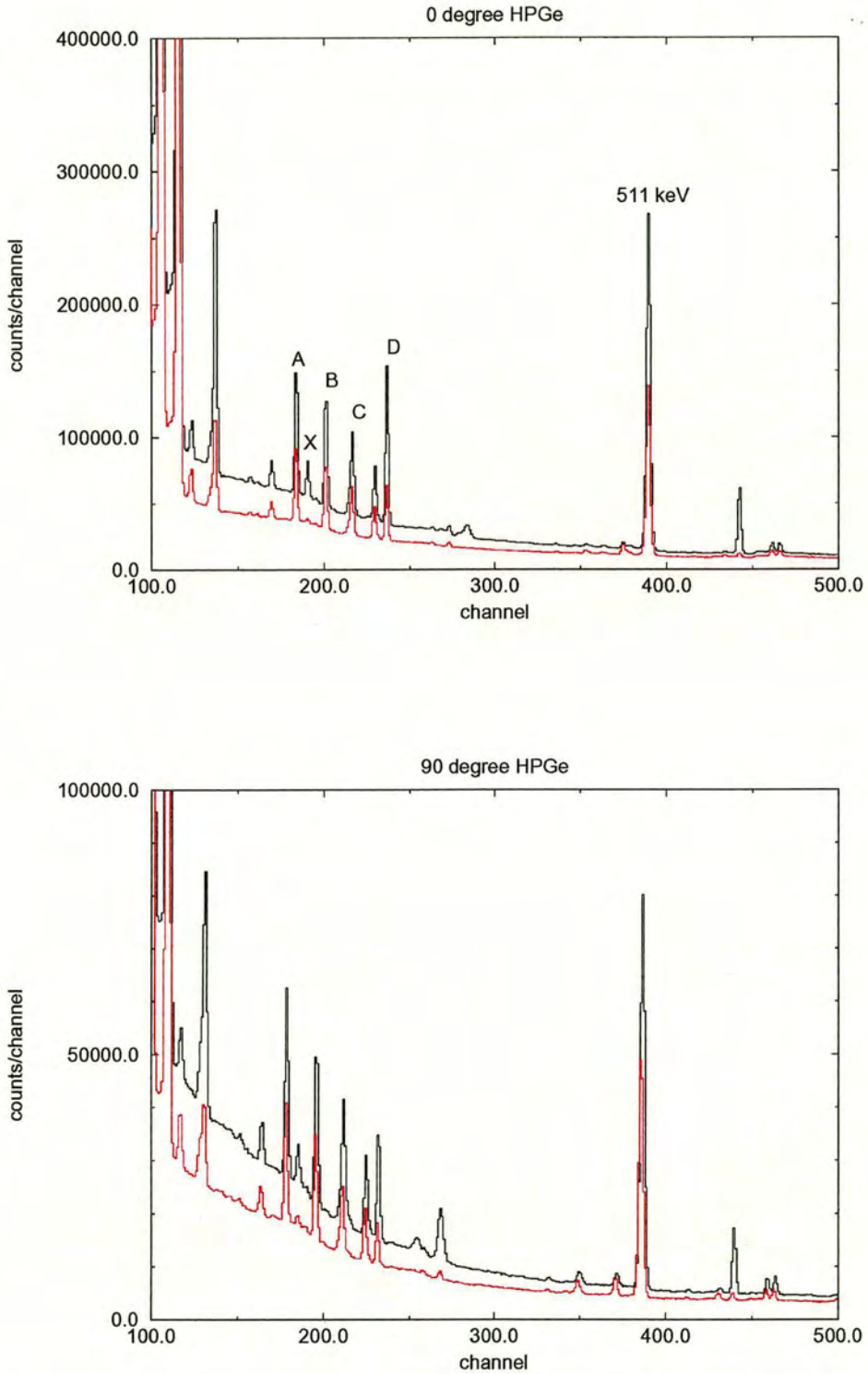

Figure 3.5: *Low energy sections of un-gated γ-ray spectra for 0° and 90° detectors respectively. The red data are the corresponding unimplanted target runs. Marked are Tungsten and Tantalum Coulomb excitation peaks.*

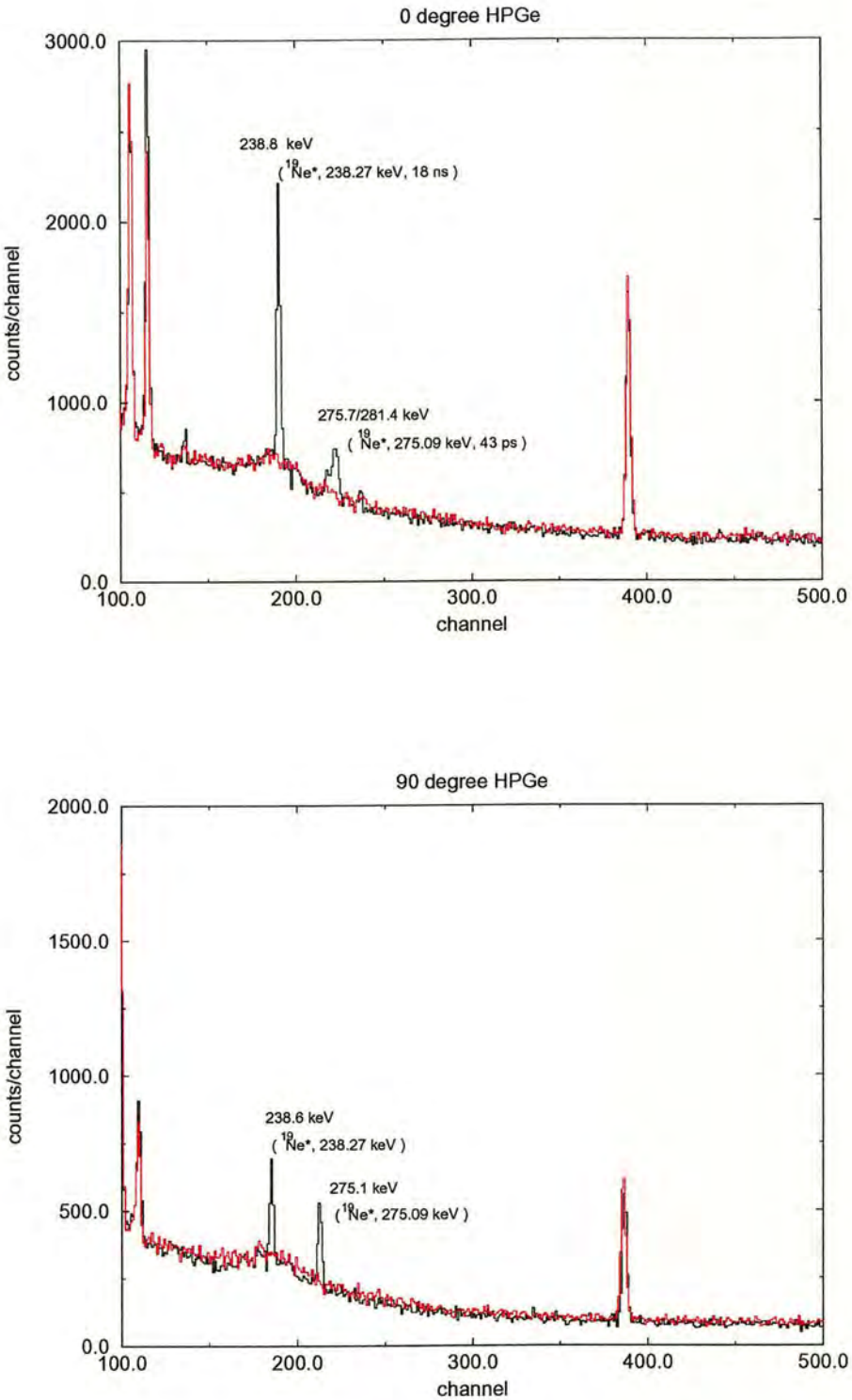

Figure 3.6: *Low energy sections of α-particle coincident γ-ray spectra for 0° and 90° detectors respectively. The red data are the corresponding unimplanted target runs. The identifications of the peaks for the first and second excited states decays of ^{19}Ne are shown. Note that the peak identified as the decay from the 275 keV state has a Doppler profile in the 0° detector but not the 90° detector.*

E_x (keV)	J^π	τ	E_γ (keV)	Intensity (%)
238.27	$5/2^+$	18.0 ns	γ_0 238.27	100
275.09	$1/2^-$	42.6 ps	γ_0 275.09	100
1507.6	$5/2^-$	1.0 ps	γ_{275} 1232.5	100
			γ_{238} 1269.3	14
1536.0	$3/2^+$	19 fs	γ_{275} 1260.9	5
			γ_{238} 1297.7	100
1615.6	$3/2^-$	99 fs	γ_{275} 1340.4	100
			γ_{238} 1377.2	14
			γ_0 1615.5	29
2794.7	$9/2^+$	97 fs	γ_{238} 2556.2	100
4032.9	$3/2^+$	< 35 fs	γ_{1536} 2496.7	19
			γ_{275} 3757.4	6
			γ_0 4032.4	100
4140	$(9/2)^-$	< 0.21 ps	γ_{1508} 2632	100
4197.1	$(7/2)^-$	< 0.25 ps	γ_{1508} 2689.3	100
			γ_{238} 3958.4	25

Table 3.3: *Excited states of ^{19}Ne and γ-ray decay energies up to 4197.1 keV.*

the spectrum, without detector resolution effects or Doppler shifts included, resulting from the Monte Carlo simulation. It can be seen from the figure that the most intense set of γ-rays seen from the decaying nucleus are those at 238 keV and 275 keV. This is partly due to the larger cross-section for formation of these states, and partly because higher energy states will feed through these states with the emission of higher energy γ-rays in coincidence. The next most intense group of γ-rays are those between 1-2 MeV. Figure 3.7 also shows these would have at least an order of magnitude lower intensity than the 238 keV and 275 keV peaks. Successively higher energy γ-ray groups would have lower and lower intensity, until the γ-ray of interest from the decay of the 4.033 MeV state should be seen with an intensity of less than one-hundredth of that of the 239 keV and 275 keV peaks.

Figure 3.8 shows the sections of the α-gated Germanium spectra where

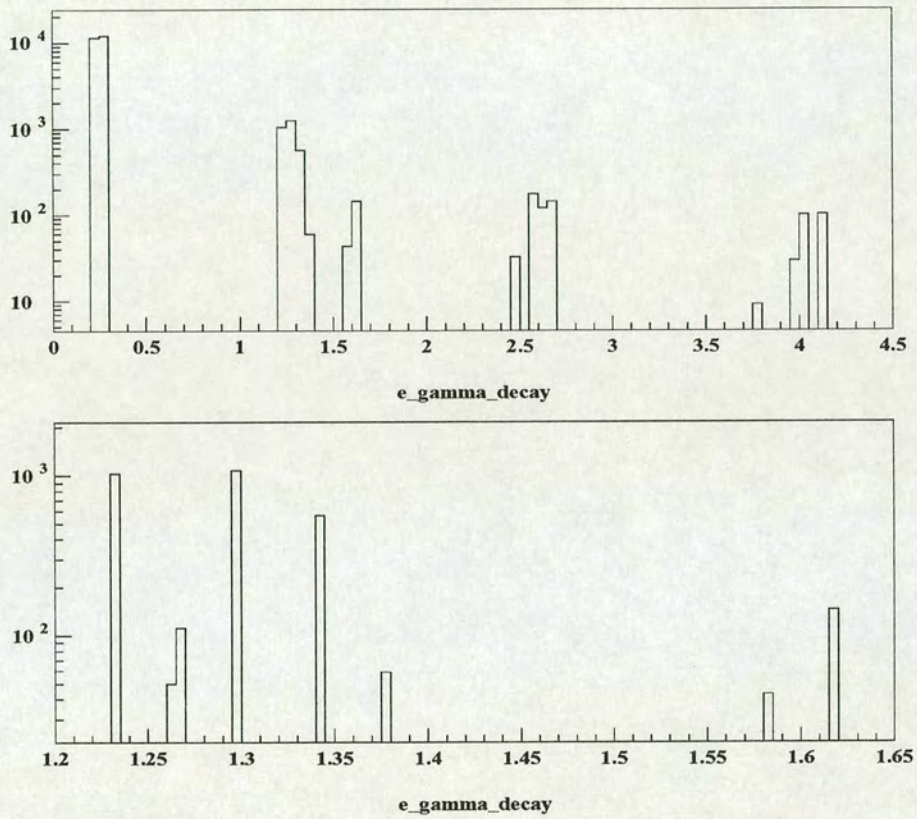

Figure 3.7: *Relative intensities of γ-rays from decay of ^{19}Ne from states up to 4197 keV from a Monte Carlo simulation. The top section shows the full range of γ-rays from 0-4.5 MeV, while the bottom section focuses on the 1-2 MeV group of γ-rays.*

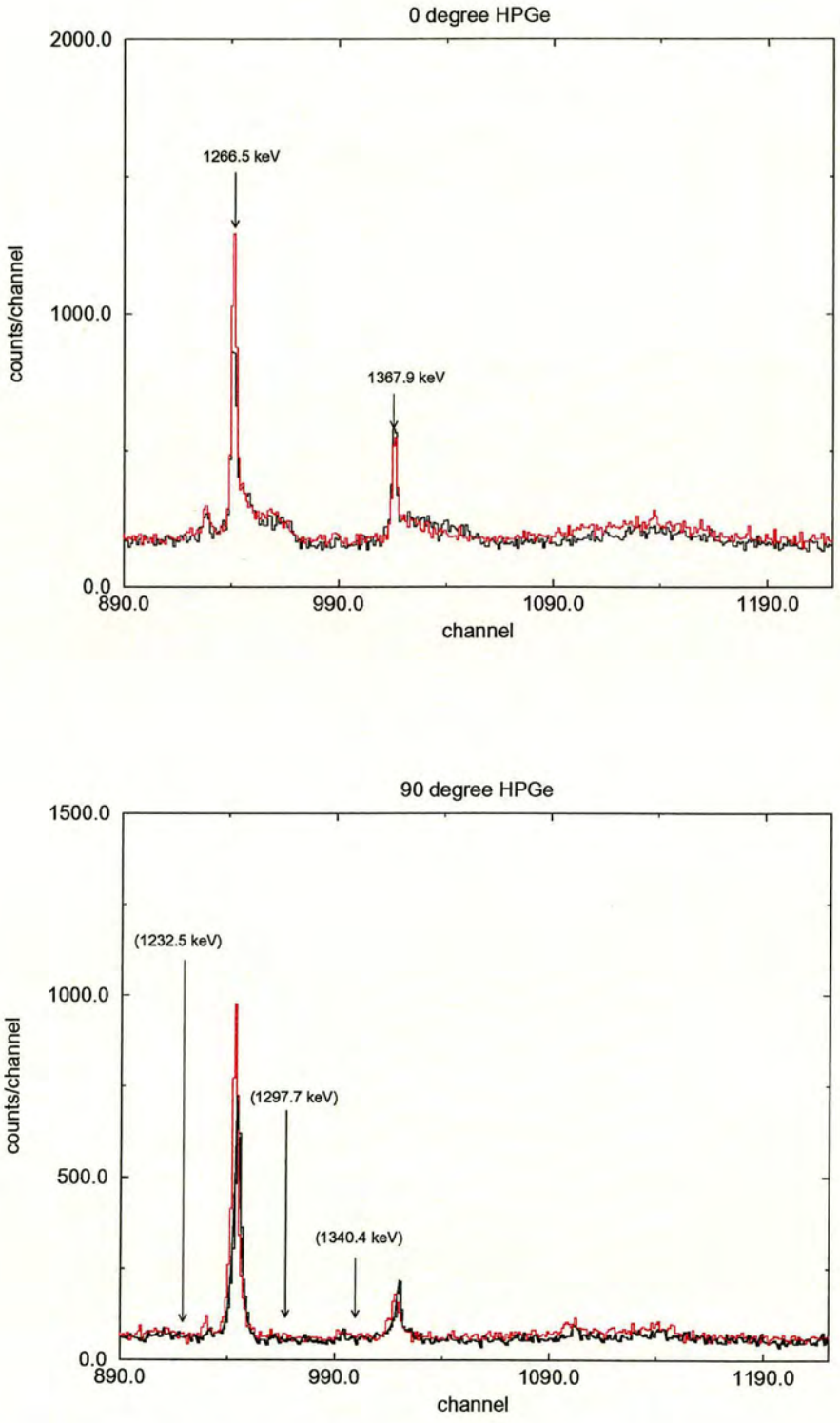

Figure 3.8: *Sections of the 0° and 90° α-gated Germanium detector data in the region of 1.2-1.6 MeV, where the second most intense group of γ-rays from the decay of ^{19}Ne are expected. The intense peaks marked are thought to be fusion-evaporation background contamination. The bracketed energies show where the most intense ^{19}Ne lines are expected in the 90° detector.*

one would expect to see the next most intense γ-rays from ^{19}Ne. The arrows indicate where these peaks would be in the 90° spectrum. There is no discernible difference between the implanted target data (black) and the unimplanted target data (red) in this region. The peaks seen in these spectra are thought to result from fusion-evaporation background events.

The absence of the expected peaks in this region either indicates that higher energy excited states are not being formed in the reaction, or they are being formed but the γ-rays are not being detected due to the lack of sensitivity in the Germanium detector setup. Indeed, a look at the high energy section of the Germanium detector data (figure 3.9) shows no visible peaks identifiable as decay lines from ^{19}Ne. It is therefore unlikely that we can tell from the γ-ray data alone whether or not excited states of ^{19}Ne were being formed here.

In order to ascertain if excited states in ^{19}Ne other than the first or second excited states were being formed, the α-particle spectra were gated on the 238 keV and the 275 keV peak in either Germanium detector. Events coincident with a peak count were incremented to a separate spectrum while events coincident with a background count in the peak region were decremented from the same spectrum. This resulted in the spectra shown in figure 3.10. Clearly seen are peaks in the particle spectra corresponding to excited states in ^{19}Ne. The corresponding data from the unimplanted target show no such peak formation, and indicate that the peaks are truly associated with the reaction ^{3}He(^{20}Ne,^{4}He)^{19}Ne. Given that the particle detectors subtend an angle of around 20°, the angular resolution is not sufficient to resolve individual states in ^{19}Ne. However, the separate groups of states, ie. those below 1 MeV, those between 1 MeV and 2 MeV, that at 2.79 MeV and

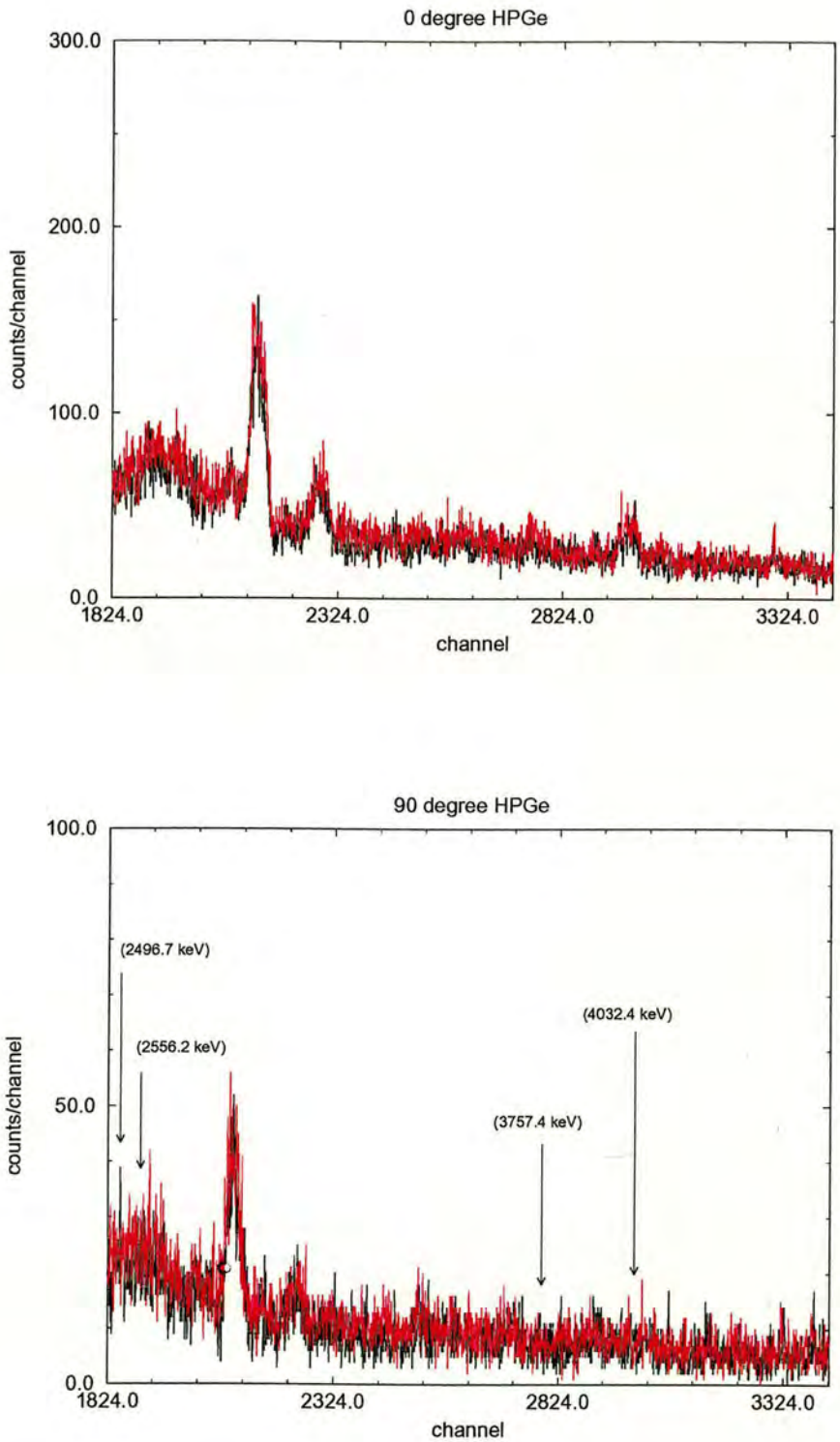

Figure 3.9: *High energy sections of the 0° and 90° Germanium spectra in the region where the first order γ-decay lines from the 4.033 MeV and 2.975 MeV states are expected. The arrows marked on the 90° spectrum show the expected positions of these lines.*

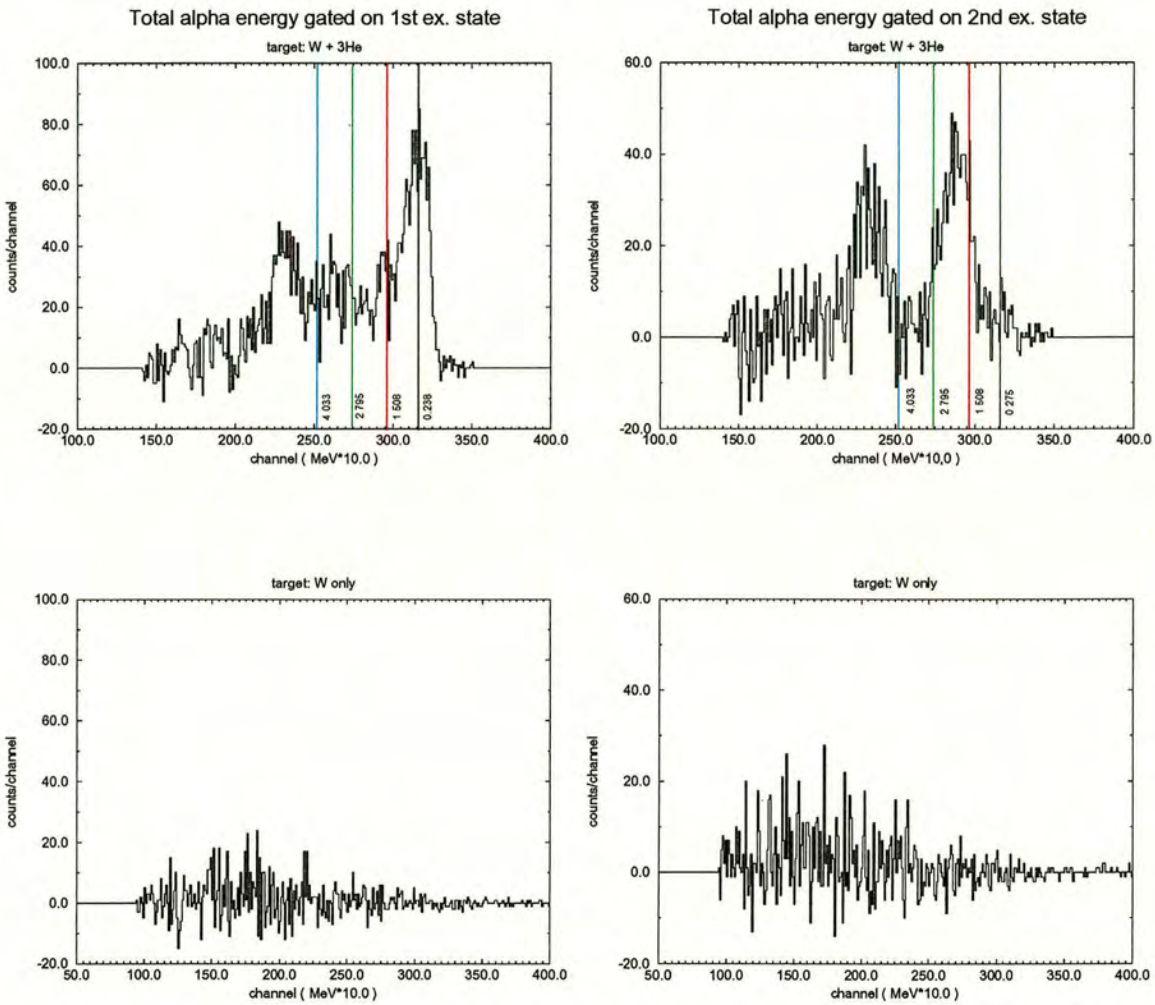

Figure 3.10: *Total alpha particle energy gated on the first and second excited states of ^{19}Ne. The coloured lines are guides to the energies of scattered ^{4}He from the reaction, at 0°, for selected excited states in ^{19}Ne.*

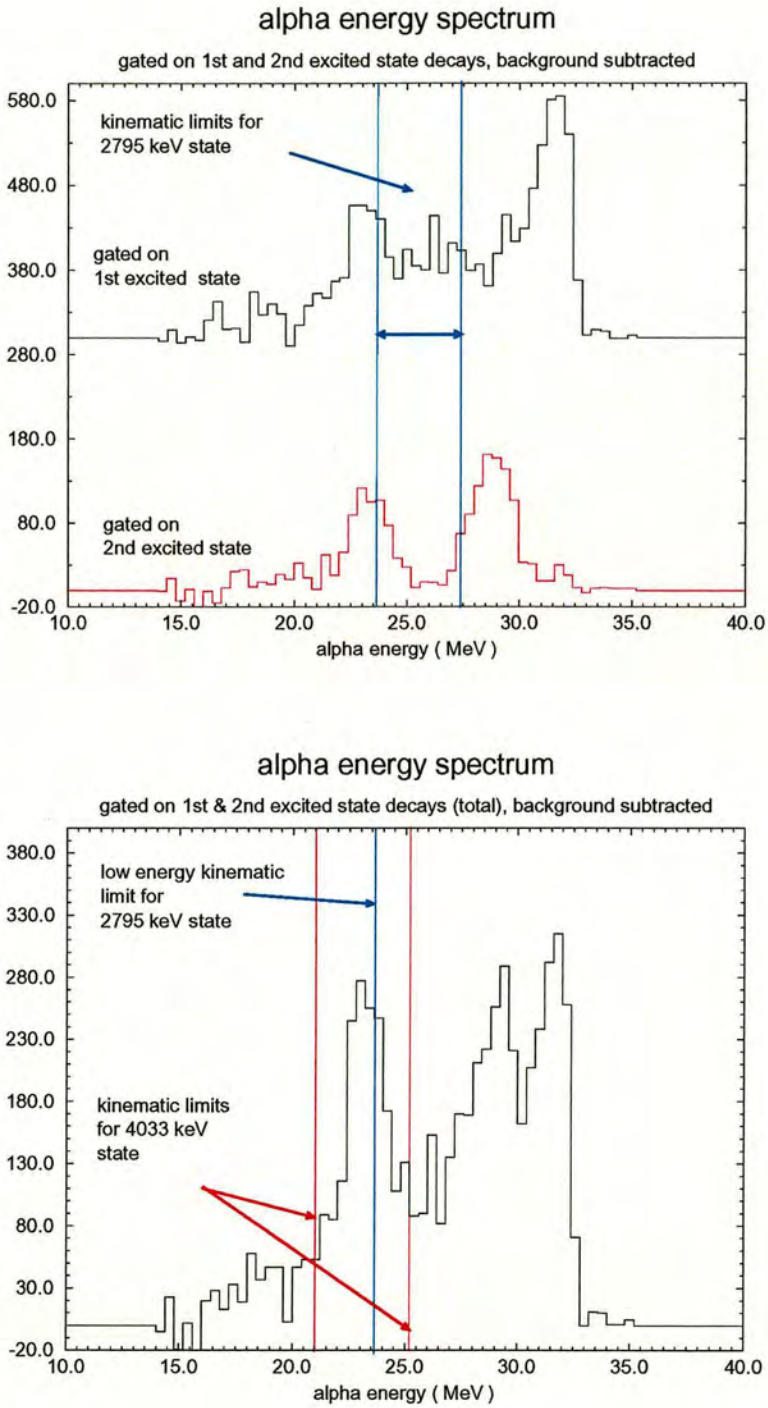

Figure 3.11: *Re-binned α-particle spectra gated on first and second excited state decays, showing the kinematic limits for formation of the 2.795 MeV and 4.033 MeV states. The 2.795 MeV state only decays to the first excited state, so that the peak in the α-spectrum gated on the second excited state which lies near the low energy kinematic limits for the 2.795 MeV state must correspond to a higher energy excited state.*

those around 4 MeV would tend to be separated. In the figure, the energies of scattered ^{4}He from the reaction at 0° have been marked for selected excited states. Because it is not known if the angular distribution peaks at 0° or higher, it is not possible to directly identify states from this energy spectrum.

Figure 3.11 shows rebinned versions of the spectra of figure 3.10. In the top spectrum, the separate rebinned spectra of α-particles gated on the first excited state and second excited state are shown. The highest energy peak (corresponding to the lowest excitation energy in ^{19}Ne) in the spectrum gated on the 238 keV γ-ray is consistent kinematically with the direct formation of the first excited state of ^{19}Ne. The second highest energy peak is seen in the second excited state gated spectrum, and is consistent kinematically with the direct formation of this state. The top picture also shows the kinematic limits for the formation of the excited state at 2.795 MeV. Therefore, any α-particle events with lower energy than these limits must have come from a state in ^{19}Ne higher than 2.795 MeV. The next such state is in fact the 4.033 MeV state. The 2.795 MeV state only decays to the first excited state, and therefore should not be seen in the spectrum gated on the 276 keV γ-ray. Therefore the peak to the low energy side of the blue marker must correspond to a state of higher energy than 2.795 MeV. The lower picture shows the kinematic limits for formation of the 4.033 MeV state, superimposed on an amalgamated spectrum of α-events gated on both the first and second excited state γ-rays. This clearly shows that the low energy peak at around 23 MeV α-particle energy is consistent with the formation of the 4.033 MeV state. However, since the true angular distribution of the reaction at these angles is unknown, an assignment to this kinematic group

cannot be justified since contributions from higher energy states cannot be ruled out. The detected α-particle energy at 0° corresponding to a ^{19}Ne excited state of around 5.5 MeV would be approximately 22.4 MeV. This is the maximum energy the α-particle from this state could have. From figure 3.11, it is quite easy to see that this then constrains the possible makeup of the lowest energy peak even further; we can rule out any states higher than 5.5 MeV. Thus the highest energy excited states formed in this reaction are between 4.033 MeV and 5.5 MeV.

These data show evidence that excited states in ^{19}Ne with higher energy than 2.795 MeV are being formed in the reaction, with only the resulting secondary γ-rays from the first and second excited states being detected. However, direct assignments to the peaks in the α-particle spectra coincident with these decays cannot be made since individual states cannot be resolved.

In considering the branching ratios from the 4.033 MeV state, and how they feed into the first and second excited states, we can say that the ratio of 238 keV γ-rays to the 275 keV γ-rays associated with the 4.033 MeV state decay is expected to be around 18:7. From figure 3.10, we can see that the α-peak at around 23 MeV is stronger in the 238 keV γ-ray gated spectrum than in the 275 keV γ-ray spectrum, although it is difficult to say by how much because of the poor statistics. However, without considering decays from states higher than 4.033 MeV, we cannot derive detailed information about the strength of the 4.033 MeV state based on this data.

3.6 Conclusion

The data collected in this experiment have shown that excited states in ^{19}Ne between 4.033 MeV and 5.5 MeV have been formed in the reaction ^{3}He(^{20}Ne,^{4}He)^{19}Ne, using ^{3}He implanted metal targets designed to facilitate the possibility of a measurement of state lifetimes using the Doppler-shift attenuation method. γ-rays from the first and second excited states of ^{19}Ne have been detected in coincidence with α-particles from the reaction. No direct γ-ray decays from higher energy states have been observed, due to the combination of low efficiency of detector setup and the small cross-section of the reaction.

A specific discussion on the future of the measurement of the ^{19}Ne state is presented in chapter 8, along with recommendations for proceeding with the method described in this experiment, based on the results found here.

Chapter 4

^{21}Na(p,p)^{21}Na Resonant Elastic Scattering

The remainder of this thesis focuses on a radioactive beam experiment designed to probe resonances in the ^{21}Na+p system relevant to the astrophysically important ^{21}Na(p,γ)^{22}Mg reaction. This chapter outlines the importance of this reaction and describes the techniques required to measure resonant properties in the ^{21}Na+p system in inverse kinematics.

4.1 The role of the rp-process in nucleosynthesis and the ^{21}Na(p,γ)^{22}Mg reaction

Beyond the hot CNO cycles, other cycles contribute to the processing of nuclear material. Because the Coulomb barriers are higher compared to those of the CNO cycles, these higher mass cycles only become important at temperatures greater than those associated with CNO cyclic processing [13]. The main cycles immediately above the hot CNO cycles are the NeNa and

MgAl cycles. Analogous to the breakout of the hot CNO cycles, breakout from these cycles by various routes can lead to the beginning of proton-rich nucleosynthesis via the rp-process.

4.1.1 NeNa cycle

The low temperature NeNa cycle proceeds via the reaction sequence

$$^{20}\mathrm{Ne(p,}\gamma)^{21}\mathrm{Na}(\beta^+)^{21}\mathrm{Ne(p,}\gamma)^{22}\mathrm{Na}(\beta^+)^{22}\mathrm{Ne(p,}\gamma)^{23}\mathrm{Na(p,}\alpha)^{20}\mathrm{Na....} \quad (4.1)$$

The cycle is closed because of the β^+ waiting points at ^{21}Na and ^{22}Na, which have timescales of 22.5 s and 2.602 yr respectively, and also the fact that the ^{23}Na(p,α)^{20}Ne reaction is more probable than the ^{23}Na(p,γ)^{24}Mg reaction at low temperatures.

It is interesting to note that in their famous treatise on synthesis of the elements in stars, Burbridge, Burbridge, Fowler and Hoyle limited their consideration of stellar hydrogen burning to those isotopes below and up to the close of the NeNa cycle [13]. However, today astronomical observations indicating strong abundances of proton-rich isotopes and certain stable elements create the need to explain nucleosynthesis beyond the NeNa cycle.

4.1.2 MgAl cycle

Current data suggest that at temperatures in the range $0.18 \leq T_9 \leq 0.6$, the ^{23}Na(p,γ)^{24}Mg reaction becomes faster than the ^{23}Na(p,α)^{20}Na reaction. When this happens, the NeNa cycle leaks into the MgAl cycle, which proceeds via the sequence

$$^{24}\mathrm{Mg}(\mathrm{p},\gamma)^{25}\mathrm{Al}(\beta^{+})^{25}\mathrm{Mg}(\mathrm{p},\gamma)^{26}\mathrm{Al}(\beta^{+})^{26}\mathrm{Mg}(\mathrm{p},\gamma)^{27}\mathrm{Al}(\mathrm{p},\alpha)^{24}\mathrm{Mg}.... \quad (4.2)$$

This reaction is therefore also closed by a (p,α) reaction, which competes with a (p,γ) reaction at higher temperatures, where the possibility of breakout from the cycle becomes more likely.

4.1.3 rp-process

In order to explain the synthesis of elements up to Z,N=50, it is essential to consider the rapid-proton (rp) process, which is characterised by a fast sequence of proton capture reactions on stable and radioactive nuclei. These reactions must compete with β^{+} decay, which brings the nucleosynthesis closer to stability, and photodisintegration reactions [36]. When temperatures are such that proton captures are faster, the reaction pathway can proceed in various ways to form higher mass proton-rich isotopes far from stability.

The rp-process depends strongly upon the conditions in the stellar environment, and high temperatures and hydrogen-rich surroundings are the vital components to these conditions. The process is thought to be initiated in a global sense when there is either a rapid increase in temperature in a hydrogen rich environment (such as a shock front), or when there is the rapid addition of hydrogen-rich material into an already hot environment [37], such as the accretion process in novae and X-ray binary systems.

One trigger reaction for the rp-process is thought to be ^{19}Ne(p,γ)^{20}Na, which has been studied previously [17] [38]. This reaction allows the possib-

ility to bypass the NeNa cycle by the subsequent reaction ^{20}Na(p,γ)^{21}Mg, and assuming conditions are hot enough, compete with β^+ decay to keep the nuclei away from stability.

Typical rp-process temperatures are around $T_9 \geq 0.5$. At these temperatures, the NeNa cycle can be broken via the ^{22}Na(p,γ)^{23}Mg reaction, and the MgAl cycle broken by the ^{26}Al(p,γ)^{27}Si reaction [17]. These are then alternative routes into the rp-process along with the ^{21}Na(p,γ)^{22}Mg reaction. Figure 4.1 shows the pathways of the NeNa and MgAl cycles, as well as early (p,γ) pathways leading to or in the rp process, as well as the competing β^+ decay pathways which drive nucleosynthesis closer to stability. Many of the important rp-process (p,γ) reaction rates involving radioactive isotopes are unknown experimentally, in contrast to β^+ decay rates, which have been more extensively studied.

The rp-process ends in a possible two ways; either the SnSbTe cycle can halt the nucleosynthesis of heavier elements than Te, or the environment can run out of hydrogen fuel [36].

The main importance of the study of the rp-process is for nucleosynthesis. The CNO cycle would still dominate the energy generation process in nova rp-process sites, but the rp-process has the largest impact on the formation of the chemical elements. In X-ray bursts, the rp-process may not be as important for nucleosynthesis since distribution of nucleosynthesised material may be impeded by the strong gravitational pull of the neutron star. However, at the higher temperatures encountered in X-ray bursts, the energy released in the rp-process is comparable to that released in the CNO cycle, making consideration of the rp-process as an energy generation mechanism more important [36].

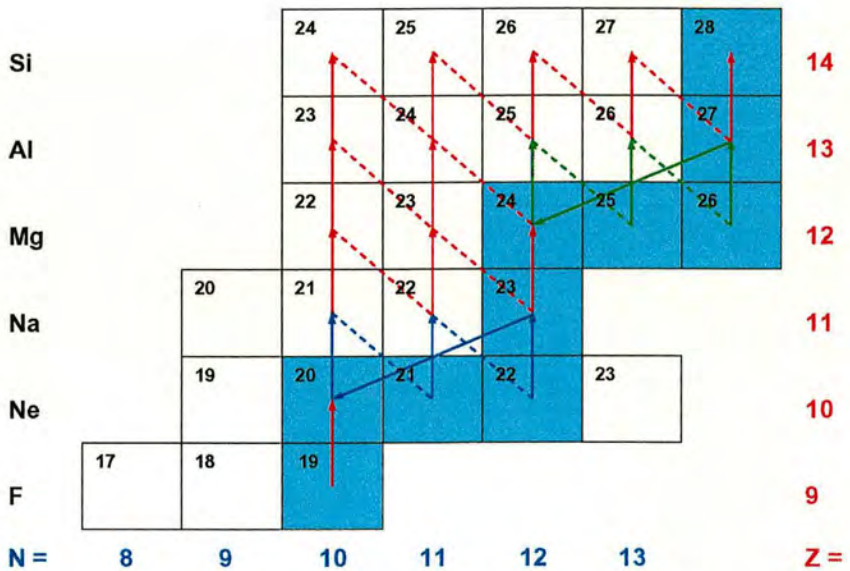

Figure 4.1: *Paths in the early rp process (red), NeNa cycle (blue) and MgAl cycle (green). The dashed lines denote β^+ decay, the solid vertical lines (p,γ) reactions and the solid diagonal lines (p,α) reactions.*

4.1.4 Abundances of Ne and Na

Part of the challenge in understanding rp-process nucleosynthesis is to explain why high abundances of certain isotopes appear in the spectra of certain types of novae. Such novae are thought to contain an oxygen-neon-magnesium (ONeMg) white dwarf. Overabundances of Ne in particular are observed in these systems [39]. Associated with these novae is the radioisotope ^{22}Na, one of the participants in the NeNa cycle and rp-process. It has long been suggested that ^{22}Na could be used as a diagnostic to compare nova reaction network models to actual nova outbursts. This is because there is a readily identifiable observational signature of the presence of ^{22}Na in novae systems. ^{22}Na β^+ decays into an excited state of ^{22}Ne which then γ-decays with an energy of 1.275 MeV. The mean lifetime of this decay of 3.75 yr allows the possibility of extrapolation to measure how much ^{22}Na was initially synthesised in a nova event, based on the observations of the decay γ-ray some time after the event. Space based γ-ray observatory instruments, such as CGRO/COMPTEL[1], CGRO/OSSE[2], or INTEGRAL[3], offer the possibility of identifying and measuring these decay lines in nova events around the Galaxy [40] [41]. INTEGRAL is currently the most advanced of these instruments, and should be operational by 2003. The satellite will carry two γ-based instruments, a spectrometer and a spatial imager, complemented by X-ray and optical instruments, and offers the best possibility of ^{22}Na abundance measurements in novae, which if made, will place significant constraints on existing nova models.

[1]Compton Gamma Ray Observatory/Imaging Compton Telescope
[2]Compton Gamma Ray Observatory/Oriented Scintillation Spectrometer Experiment
[3]International Gamma Ray Astrophysics Laboratory

4.1.5 ^{21}Na(p,γ)^{22}Mg

To compare observations with nova models, it is crucial to know the rates of formation of ^{22}Na at a given temperature, via different channels. The formation of ^{22}Na in novae can proceed via the sequences ^{21}Na(p,γ)^{22}Mg(β^+)^{22}Na or ^{21}Na(β^+)^{21}Ne(p,γ)^{22}Na. Of these two channels, the latter presents the least uncertainty, since the β^+ decay lifetime and the ^{21}Ne+p capture rate are well known. In contrast the rate of the ^{21}Na(p,γ)^{22}Mg reaction has only previously been based on information taken from comparisons with analogue nuclei [42].

For a given proton number, the isotopes on the neutron-deficient side of stability generally have smaller proton separation energies than the stable isotopes. This means that for compound nuclei formed in proton capture reactions, those which are closer to stability will be formed in a region where the level density is high in the compound nucleus. Thus for stable nuclei or those close to stability, Hauser-Feschbach statistical model calculations can be included in network calculations if experimental data are absent or limited [42]. This is not generally true for radioactive nuclei far from stability, where the compound nuclei are formed in a region where the level density is low (due to the small proton separation energy). In these situations, the reaction rates depend on the contribution of resonances from a few isolated levels and the low energy direct capture probability. Thus, where the statistical model cannot be applied, it is vital to determine the reaction rates for proton-rich nuclei experimentally. This is especially true in the case of the ^{21}Na(p,γ)^{22}Mg reaction, where the reaction rate may depend strongly on the contributions from only a few resonances for which limited data exist.

4.2 Structure of ^{22}Mg

The proton capture on ^{21}Na forms the compound nucleus ^{22}Mg. The proton separation energy of ^{22}Mg is 5.502 MeV, therefore the (p,γ) reaction will form ^{22}Mg excited states with excitation energy $E_x \geq 5.502$ MeV. In this region, nuclear energy levels are sparse, and so the ^{21}Na(p,γ)^{22}Mg rate depends only on the resonant contributions from these few states, and a small direct capture component.

^{22}Mg is an even-even nucleus with four protons in the s-d shell for the Ground state configuration, employing simple shell model arguments. Excited states of ^{22}Mg are known to show strong two-particle structure properties and are populated strongly in two-particle transfer reactions, such as ^{24}Mg(p,t)^{22}Mg, studied in ref. [43]. Most of the structure of ^{22}Mg had been mapped up until recently using the aforementioned reaction and β spectroscopy studies [44] [45], as well as the reaction ^{20}Ne(^{3}He,nγ)^{22}Mg [46]. Recently, due to the increased astrophysics interest in ^{22}Mg, which is important both for the formation of ^{22}Na in novae and the breakout of the hot CNO cycle via the ^{18}Ne(α,p)^{21}Na reaction, other reactions have been used to study its structure. Recently, another study of the ^{24}Mg(p,t)^{22}Mg reaction has been performed [47], leading to the identification of new states in ^{22}Mg. Also, the reactions ^{25}Mg(^{3}He,^{6}He)^{22}Mg [48], ^{24}Mg(^{4}He,^{6}He)^{22}Mg, [49], and ^{12}C(^{16}O,^{6}He)^{22}Mg [50] have been studied.

Table 4.1 shows values of excitation energies in ^{22}Mg above the proton threshold found in various studies. The adopted values were calculated using values from all the previous studies except that of the recent ref. [48]. Of

(p,t) Ref. [47]	(p,t) Ref. [43]	(^{3}He,n) Ref. [51]	(^{3}He,n) Ref. [52]	(^{3}He,nγ) Ref. [46]	(^{3}He,nγ) Ref. [53]	(^{16}O,^{6}He) Ref. [50]	(^{3}He,^{6}He) Ref. [48]	adopted values[a]
5713.9*	5738±35	5699±20	5680±30	5714.4±1.5	5713±2	5711±13	5713.9*	5713.9±1.2
				5837±5				5837±5
5961.9±2.5		5945±20	5980±30					5961.9±2.5
6045.8±3.0	6061±37					6041±11	6051±4	6045.6±2.9
6246.4±5.1[b]	(6281±33)[c]	6263±20[c]	(6220±50)[c]	(6298±50)[c]		6255±10	6246±4	6248.2±4.5[c]
6322.6±6.0	(6281±33)[c]		(6220±50)[c]	(6298±50)[c]			6329±6	6322.6±6.0
6613±7[d]	6645±44	6573±20				6606±11	6616±4	6608.5±5.6
6787±14	6836±44	6770±20	6760±90			6767±20	6771±5	6780.4±9.6
						6889±10	6878±9	

Table 4.1: *Excitation energies (keV) of ^{22}Mg above the proton threshold, resulting from previous experimental studies. Values marked with an asterisk were used as calibration points in their respective experiments.*

[a] average values from ref. [47]
[b] Probably a doublet [47].
[c] The "doublet" states at E_x = 6249 and 6323 keV were not resolved by these measurements.
[d] Possibly a multiplet of states [47].

these known levels, spin-parity assignments have been made in only three cases, two of which are unambiguous [47]. The E_x=5714 keV level has been assigned $J^\pi = 2^+$, the E_x=5837 keV level $J^\pi = (2^+ - 4^+)$, and the E_x=6046 keV level assigned $J^\pi = 0^+$. The remaining levels above the proton threshold have unknown spin-parity. Consideration of spin-parities has been treated mostly in experiments using two-nucleon transfer reactions. Assumptions have been made in these cases that only states in ^{22}Mg of natural parity will be strongly populated, an assumption which will be addressed later in this work. The ^{12}C(^{16}O,^{6}He)^{22}Mg reaction of ref. [50] is thought to proceed via the compound nucleus mechanism, restricting the formation of ^{22}Mg states to those of natural parity only. The reaction ^{25}Mg(^{3}He,^{6}He)^{22}Mg of ref. [48] should populate both natural and unnatural parity states in ^{22}Mg. The resonance strengths of all the states above proton threshold are not known experimentally, and any cases where reaction rates have been estimated have been based on analogue state assignments in ^{22}Ne.

The first three levels above proton threshold are thought to be important contributors to nova nucleosynthesis at the relevant temperatures [39], and previous reaction rate calculations have included these resonances with assumed resonance strengths. Of these three, the existence of the level at E_x=5837 keV has been brought into question since it has only been seen in one experiment, and not others where it should be populated with comparable strength. The fact remains that for nova network calculations, the properties of these three resonances need to be experimentally determined, which includes the spin-parity assignments, proton partial widths and total widths. Less attention has been paid to the higher energy resonances since the focus has been for relatively low temperature nova scenarios. However,

as the temperature rises in other scenarios, the contributions from higher states may become important, especially if they are low orbital angular momentum captures, introducing the possibility also that their influence might extend down into the nova temperature region with comparable strength to the direct capture rate.

4.3 Radioactive beams and resonant elastic scattering

It is imperative to have some sort of direct experimental determination of level properties in ^{22}Mg in order to calculate the ^{21}Na(p,γ)^{22}Mg reaction rate. Because the actual reactions of interest involve radioactive target nuclei, up until recently it has been impossible to measure the rate of these reactions directly, since the target nuclei do not live long enough to bombard with protons using the traditional (p,γ) reaction method. However, developments with accelerated radioactive beams and experiments in inverse kinematics during the last 10-15 years have made it possible to measure the reaction rates of some astrophysical reactions directly, or via the properties of proton resonances.

Equation 2.10 is used to calculate the resonant reaction rate, and the resonance strength, for a (p,γ) reaction, is given by:

$$\omega\gamma = \frac{2J+1}{(2I_1+1)(2I_2+1)}\frac{\Gamma_p\Gamma_\gamma}{\Gamma} \tag{4.3}$$

The direct capture component is dealt with separately, but typically

for these reactions (ie. ^{21}Na(p,γ)^{22}Mg) is extremely small. The important resonant parameters to be measured for Nuclear Astrophysics therefore are J, the spin of the compound nucleus state, Γ_p, the partial proton width of the state, Γ_γ, the partial γ-width of the state, Γ the total width of the state and E_R, the resonance energy of the state.

4.3.1 Inverse kinematics methods

Radioactive beams are in general difficult to produce. The products resulting from bombardment of some kind of stable target have to be separated and accelerated to the energy of choice. The beam particles are also constantly β-decaying, so transport of the beam to the target with sufficient intensity without losses is tricky. Also, the cross-sections in astrophysical capture reactions are usually very small, of the order of millibarns and below, requiring large beam intensities of the order of 10^8 particles/sec. Furthermore, due to the nature of the acceleration methods required to make a radioactive beam, the energies cannot be stepped in small precise increments like with a Van de Graaf generated proton beam.

The recoil separator facility DRAGON at TRIUMF provides the possibility to measure (p,γ) reaction rates directly using radioactive beams on a gaseous hydrogen target. When the reaction occurs over a resonance, the method is analogous to the traditional method which extracts the width by looking at the γ-ray yield in coincidence with recoil nuclei selected by the spectrometer. There are several problems encountered by this method. The beam cannot be stepped in as small increments as can a Van de Graaf accelerator. Instead radioactive beams tend to have associated energy centroid un-

certainties of around 10 keV/nucleon, depending on how they are produced. Also, gaseous targets are difficult to use because the density distribution varies through the target. Such an effect has to be measured to correct for this in the width measurement. To some extent, the spectroscopic structure of the compound nucleus has to be known before a (p,γ) measurement of a specific resonance can be measured; astrophysically important resonances tend to be very narrow and spaced far apart, so that prior information about the resonant structure from some method is important.

The *Centre de Recherches du Cyclotron* at Louvain-la-Neuve, Belgium, pioneered a technique for use with inverse kinematics beams designed to employ elastic proton scattering in order to deduce crucial resonant parameters complementary to the difficult (p,γ) reaction measurements [54] [55] [56] [57] [58] [59] . This technique utilises thick polyethylene ($[CH_2]_n$) targets[4] on which the beam is incident. The beam particles lose energy through the targets, which are typically 250-1000 $\mu g/cm^2$ thick, and scattering can therefore occur at a range of centre-of-mass energies. If there is a resonance present in the energy range scanned by the target, the cross-section of the outgoing protons results in the detected spectrum being greatly modified. Because the energy loss of the outgoing protons is small, and the kinematics of the proton do not vary greatly over angle for inverse kinematics elastic scattering, the spectrum is not greatly degraded by straggling effects. Therefore, the experimental spectrum is very closely equivalent to the type of excitation function that would be measured in a typical elastic scattering normal kinematics experiment where the beam energy is stepped, except in this case,

[4]The subscript n signifies that the type of polyethylene used is low density as opposed to the long-chain polymer high density type.

it is the energy loss in the target which is effectively doing the "stepping".

The experimental proton spectrum in terms of detected proton lab energy can be transformed into the centre-of-mass frame. The relationship between outgoing proton energy and incident centre-of-mass energy for inverse kinematics elastic scattering is given by

$$E_{p,lab} = 4\frac{m_1}{m_1 + m_2} E_{cm} \cos^2 \theta_{lab} \tag{4.4}$$

while the relationship between the lab angle and the centre-of-mass angle is given by

$$\theta_{cm} = \pi - 2\theta_{lab} \tag{4.5}$$

In terms of the centre-of-mass energy and centre-of-mass angle, a theoretical cross-section function can then be fitted to the corrected experimental spectrum. Usually, the absolute energy calibration of the spectrum is made by comparing the data to that of a known resonance scanned using the same method. This also gives information about any small degradation of resolution effects. The free parameters in the fit are effectively the proton width Γ_p, the total width Γ, the resonance energy E_R and the spin of the state J^π. By combining a series of thick target runs at different incident beam energies, a large energy region in the centre-of-mass can be covered, possibly discovering previously unknown resonances and accurately defining the positions of others. In this way, vital information for the (p,γ) measure-

ment can be obtained. However, as a stand-alone method, the determination of E_R, Γ_p, Γ and J^π can put limits on the reaction rate if values of Γ_γ are estimated from, for example, the mirror nucleus. The resonant elastic scattering method described here was chosen in this work to measure some of these parameters for potentially important resonances to the ^{21}Na(p,γ)^{22}Mg reaction.

Figure 4.2 shows a typical variation of an s-wave type resonance over a range of lab angles. The maximum scattering angle for the recoil protons is 90°, which corresponds to 0° in the centre-of-mass system. One can see from the picture that there is a significant variation of the resonance shape over the range $0° \leq \theta_{lab} \leq 45°$, which corresponds to a centre-of-mass angle range of $90° \leq \theta_{cm} \leq 180°$. At $\theta_{lab} = 0°$, the size of the resonance with respect to the Coulomb backGround is greatest.

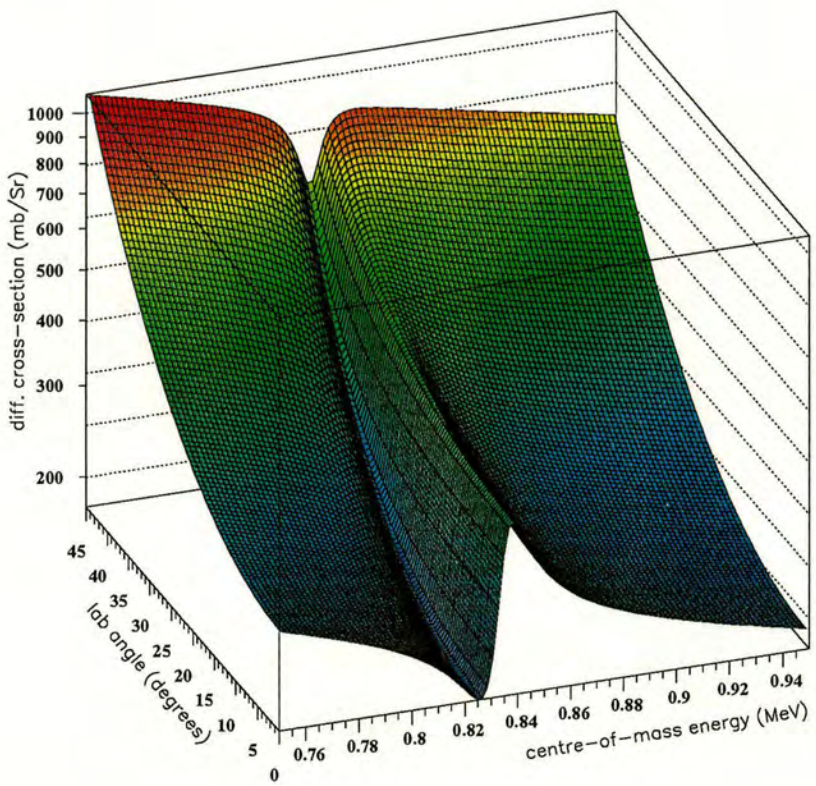

Figure 4.2: *Variation of a typical s-wave resonance over energy and angle.*

Chapter 5

Experimental Procedure

The elastic scattering experiment which is the subject of the remainder of this work utilised the methods described in the previous chapter, and was performed at the **TUDA** facility at **ISAC-TRIUMF**, Vancouver, Canada. **TRIUMF** is the **TRI**-Universities Meson **F**acility, Canada's national particle and nuclear physics lab. The lab is centred around what remains the world's largest sector-focussing cyclotron, capable of accelerating H^- ions up to 520 MeV. Originally used for the production and study of mesons in the field of sub-nuclear physics, the cyclotron is now mainly used for the production of Radioactive Ion Beams in concert with the **ISAC**, (**I**sotope **S**eparator and **AC**celerator), facility.

The **TUDA**, (**T**riumf-**U**.K. **D**etector **A**rray), facility is a multipurpose charged particle Silicon detector array, scattering chamber and instrumentation apparatus, designed for use in radioactive beam facilities such as **ISAC**, where highly segmented, large solid angle detectors provide an experimental advantage over traditional Silicon detector technologies. In the following chapter, the experimental setup of the **TUDA** facility during the

experiment will be detailed. The production and acceleration of the ion beams used in the experiment will be explained, including an overview of the **ISAC** facility itself.

5.1 ISAC

ISAC is a facility for producing post-accelerated radioactive and stable nuclear beams. The facility can be divided into six sections: The beam production apparatus, the Low-Energy Beam Transport (LEBT) section, the Radio Frequency Quadrupole (RFQ) acceleration section, the Medium-Energy Beam Transport (MEBT) section, the Drift-Tube Linac (DLT) linear acceleration section and the High-Energy Beam Transport (HEBT) section. The beam production section consists of a target station for the production of radioactive isotopes and an off-line ion source (OLIS) for the production of various stable ions.

5.1.1 Radioactive ion production

The radioactive production target consists of a water cooled Silicon Carbide (or Tantalum or Niobium, depending on nuclear species required) thick target. The proton beam produced by the main cyclotron is incident on the target at energies between 450-500 MeV, with currents of several micro-Amperes. A menagerie of nuclear reactions occur within the target material, and the radioactive (and stable) species which are the product of these reactions must diffuse out of the target so that they might be separated, isolating the specific required ion of interest. An on-line source provides the ionisation and subsequently the low-energy radioactive ions are extracted

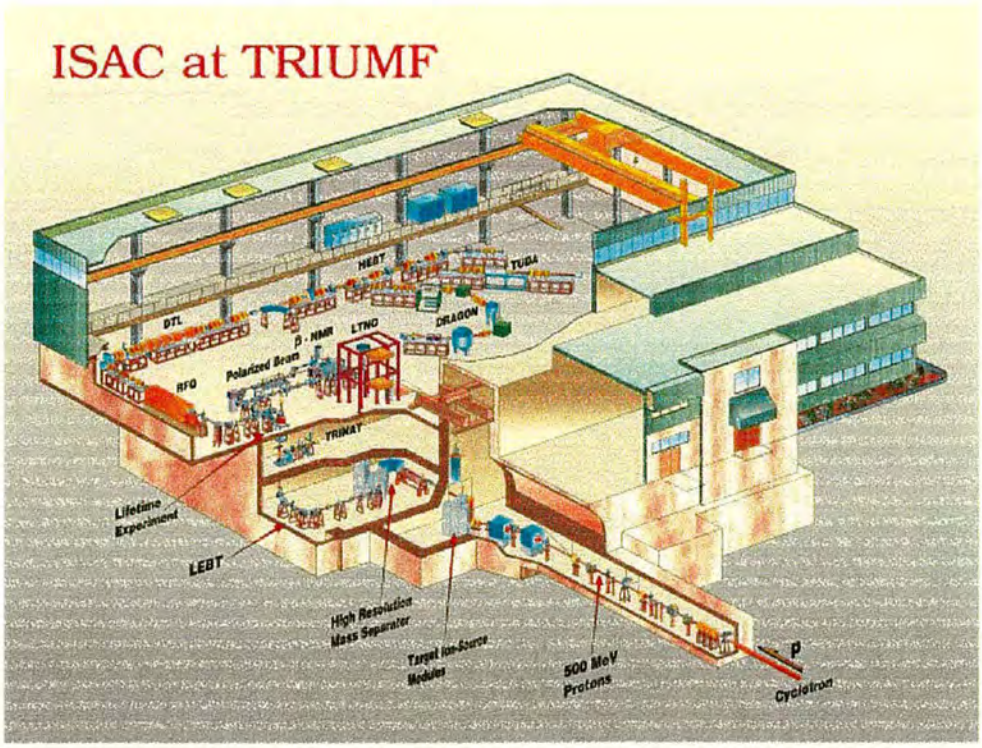

Figure 5.1: *3-dimensional view of ISAC beam hall.*

into a mass-separator. The chosen radioactive species are then transported into the low-energy transport section (LEBT).

5.1.2 Beam transport and acceleration

In LEBT, the beam is pre-bunched, and transported into the eight-metre long RFQ, which provides transverse focussing while the time-varying longitudinal component of the quadrupole field provides acceleration up to a final fixed energy of 150 keV/A [60] [61].

In the MEBT section, the beam is chopped and then stripped within a thin Carbon foil to final charge-to-mass ratios of $1/6 \leq q/A \leq 1/3$. The beam is then rebunched and transported into the DLT, which provides continuously variable acceleration to final energies of up to approximately 1.5 MeV/A via a series of successively larger Copper vacuum tanks, within the skin of which the RF field washes back and forth against the phase of the central anode, providing the accelerating wave structure.

In the HEBT section several quadrupoles and rebunchers maintain the time structure and focus the beam. There are two bunchers operating close to the final achromatic bends in the beamline before the main high energy experimental stations, **TUDA** and **DRAGON**. These bunchers provide timing resolution of better than 1 nanosecond, compared to a beam bunch period of 86 nanoseconds. Prior to the **TUDA** experimental area there is one last set of focussing quadrupoles.

For the production of stable beams, prior to the LEBT section, there is a microwave cavity-resonance gas ion-source able to provide several species of stable ions for acceleration. The system is such that the operators are

able to switch between stable and radioactive beams (once both are set up) with the minimum of inconvenience.

5.2 Experimental setup

5.2.1 General layout of TUDA facility

The **TUDA** facility comprises of a main scattering chamber and an instrumentation shack. The scattering chamber consists of two cylindrical sections, coaxial with the beam, joined either side of a main rectangular section. This section contains the target ladder apparatus, as well as various modifiable entry ports, and a turbo vacuum pump. The detector assembly is designed to sit at a chosen variable position on four support rails, its face perpendicular to the beam axis. The withdrawable rear flange allows the entire detector assembly to be withdrawn from the chamber, making maintenance and modification of the assembly extremely convenient.

The front (upstream) end of the chamber contains a collimator assembly allowing up to six positions. These collimators are positioned immediately after the last quadrupole, so that a variety of different collimator sizes are required for the different speeds of the focus between the quadrupole and the target position. During this experiment a collimator of diameter 10 mm was usually in place.

Between the collimator assembly and target position there is an additional collimator disc to prevent the primary scattered beam from hitting the detectors or target assembly. The target ladder itself is a calibrated linear-drive variable position ladder with up to nine positions. Figure 5.2

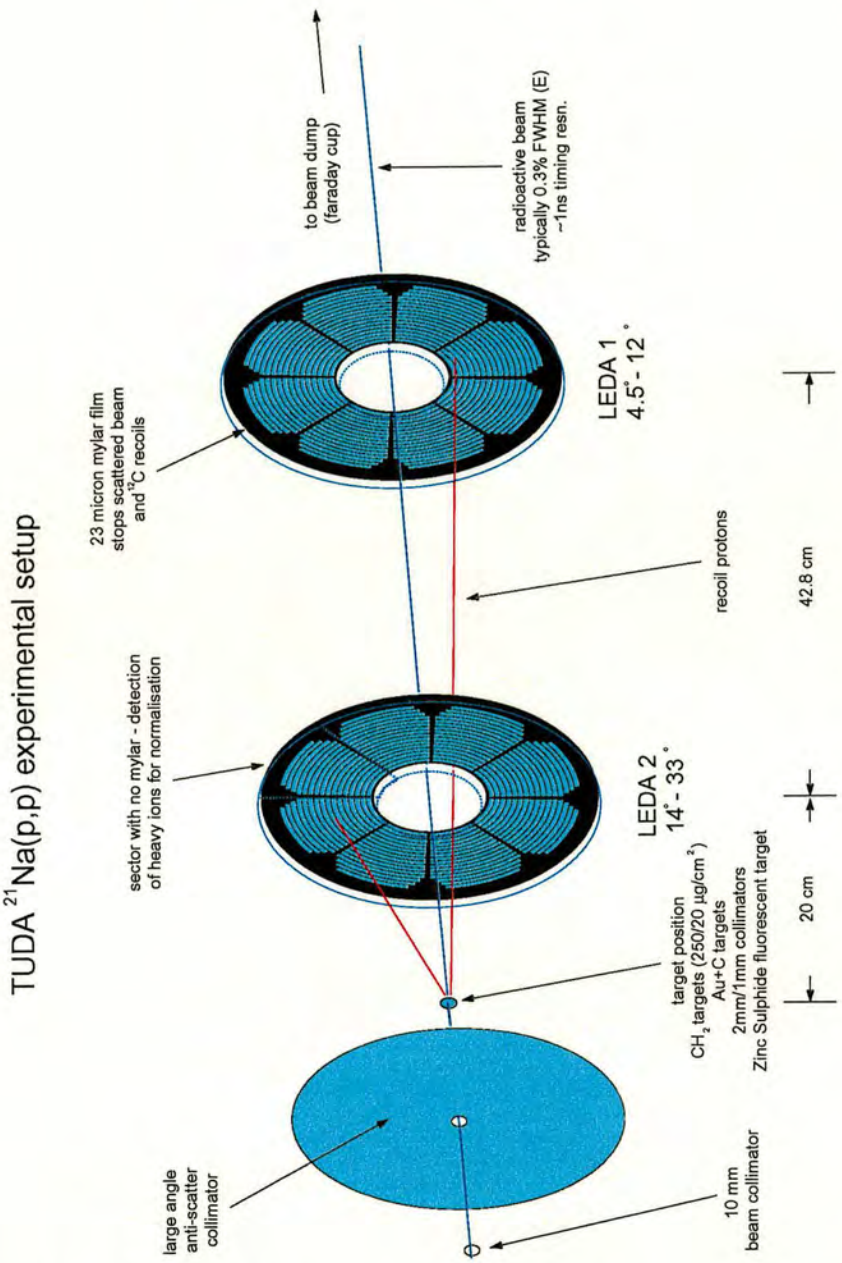

Figure 5.2: *Schematic of the experimental setup inside the TUDA chamber.*

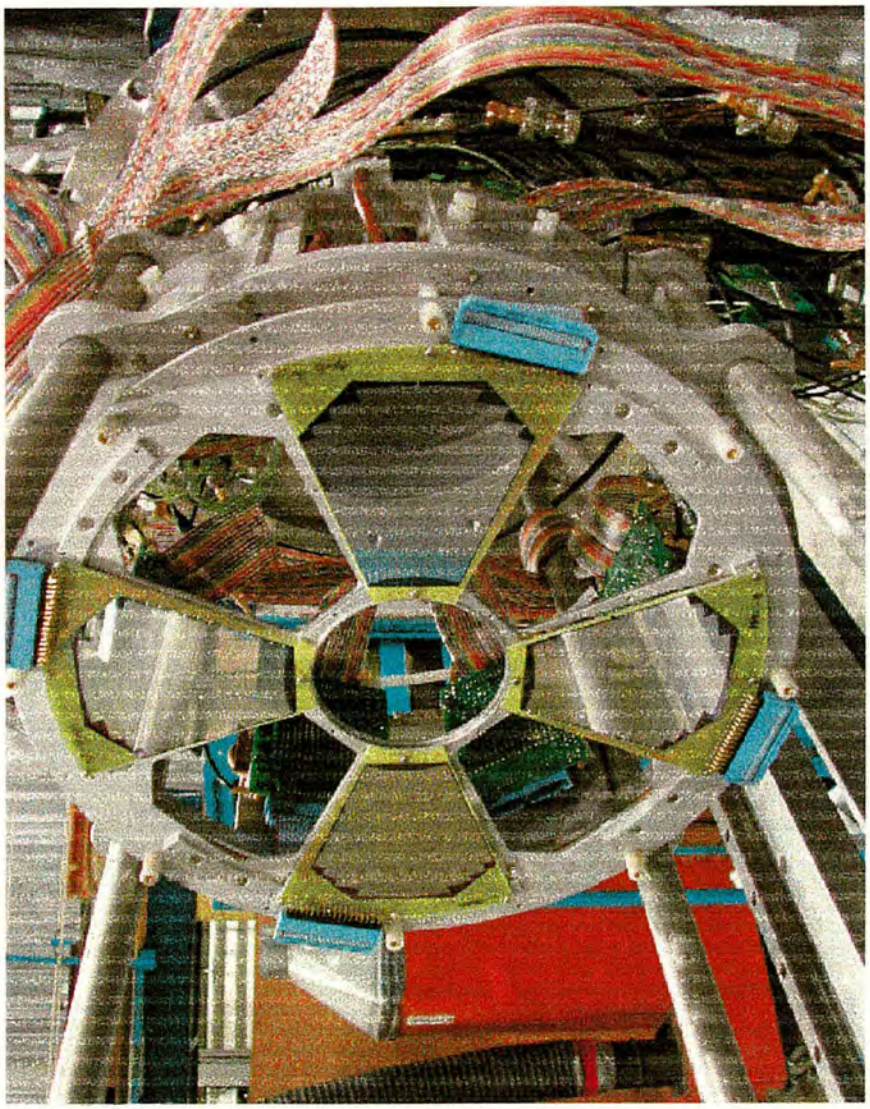

Figure 5.3: *Photograph of four LEDA detector segments withdrawn from TUDA chamber.*

shows a schematic of the setup of the detectors, target ladder and collimators within the scattering chamber, while figure 5.3 shows a photograph of four LEDA segments positioned on the TUDA chamber support rails.

Connected to the rear flange of the chamber is a beam pipe leading to a further set of quadrupoles and a beam dump Faraday cup. The quadrupoles can be optimised to focus an unscattered beam, still in its original charge state, into the Faraday cup for tuning purposes.

5.2.2 Segmented Silicon detector arrays

The facility is based around the use of LEDA-type Silicon detector arrays. These detectors are p-n junction type, reverse-biased strip detectors, arranged in a radially symmetric configuration of sixteen annular strips in each of eight azimuthal segments [62]. The active area of the Silicon is set in a transmission style PCB mount, containing the voltage tracks connecting the strips on the front (junction) side and the back (Ohmic) side via ultrasonically-bonded wires to the output connector, which is of unprotected IDC type.

In this experiment, two detectors were used, positioned at 20 cm and 62.8 cm from the target ladder. In front of each detector, a mylar foil was placed in order to prevent scattered beam particles from hitting the active area, thus reducing the data rate and allowing higher beam currents to be used, while also preventing the detectors from becoming damaged due to the cumulative effects of ion implantation. Various thicknesses of mylar were required according to the beam energies used.

The full eight sectors were used for the LEDA detector positioned at

62.8 cm, while only four were used at the more backward angle detector, giving altogether 192 separately instrumented discrete detector elements. This was because the Coulomb cross-section at these backward angles was higher for recoil protons in the elastic scattering channel. Using only four sectors at these angles would go some way as to equalising the data rate in the forward and backward detectors. One of the four backward sectors was left unprotected by mylar. This was in order to detect the scattered beam from the Carbon in the targets, allowing the possibility of the normalisation of the beam current during each run.

5.2.3 Instrumentation and data acquisition

The detectors are instrumented via IDC cabling to preamplifier units which sit directly behind the detector active area. Because the electronics reside within the confines of the vacuum chamber, conventional fan-assisted cooling is impossible. Instead, hollow copper shrouds encase the ends of the PCB, and the contact is set with thermal paste. An external refrigeration unit then cycles ethyl-glycol coolant through a network of hoses into each copper shroud, efficiently drawing heat from the PCB. The unit is thermostat controlled and is able to maintain the temperature of the coolant at a stable -10°C, while each of the preamplifiers is kept stable at between 20°-50°C.

The detector output signal cabling and services connectors (bias inputs, test signal inputs, thermocouple connectors etc.) exit the chamber through ports in the rear flange of the chamber. The signals then proceed through IDC 16-way cables into the electronics shack, where the instrumentation and acquisition systems are based. The entire shack is lined with

Copper plating, effectively making it a Faraday cage, to reduce any background noise which may interfere with the sensitive instrumentation and detector setup. The shack is electrically isolated from the rest of the open plan experimental area, and is provided with a separate clean grounding line. The scattering chamber is also isolated from the experimental area and shares the ground line with the shack. This way, all noise levels and possible interference can be accurately and confidently controlled by the experimenters.

The primary experimental signals arrive in the shack into a series of junction boxes. These split each 16-way signal into 2× 8-way connectors. These signals are input into the 8-channel RAL shaping amplifiers specifically designed for LEDA detectors. The gain of these amplifiers was set to give an output analogue signal with a dispersion of 0.5 V/MeV. These analogue signals were input into twenty-four 8-channel SILENA 4418 CAMAC-interface ADC units, with an input voltage range of around 100mV-10V, giving a full-scale energy range of around 200 keV-20 MeV. The unprotected sector of the backward angle detector was set with a lower gain to give a full-scale range of 400 keV-40 MeV, in order to be able to detect the higher energy signals from the scattered heavy ions.

The ECL-type digital fast signal generated at the timing output of each RAL amplifier channel is connected to a set of purpose built logic modules, in this case set as the total OR of all channels. This primary experimental trigger then must satisfy the conditions of coincidence with the HF accelerator signal (11.8 MHz, from the low β buncher) and coincidence with the not busy signal generated via the CAMAC acquisition system. An accepted trigger generates an ADC gate allowing signals to be converted

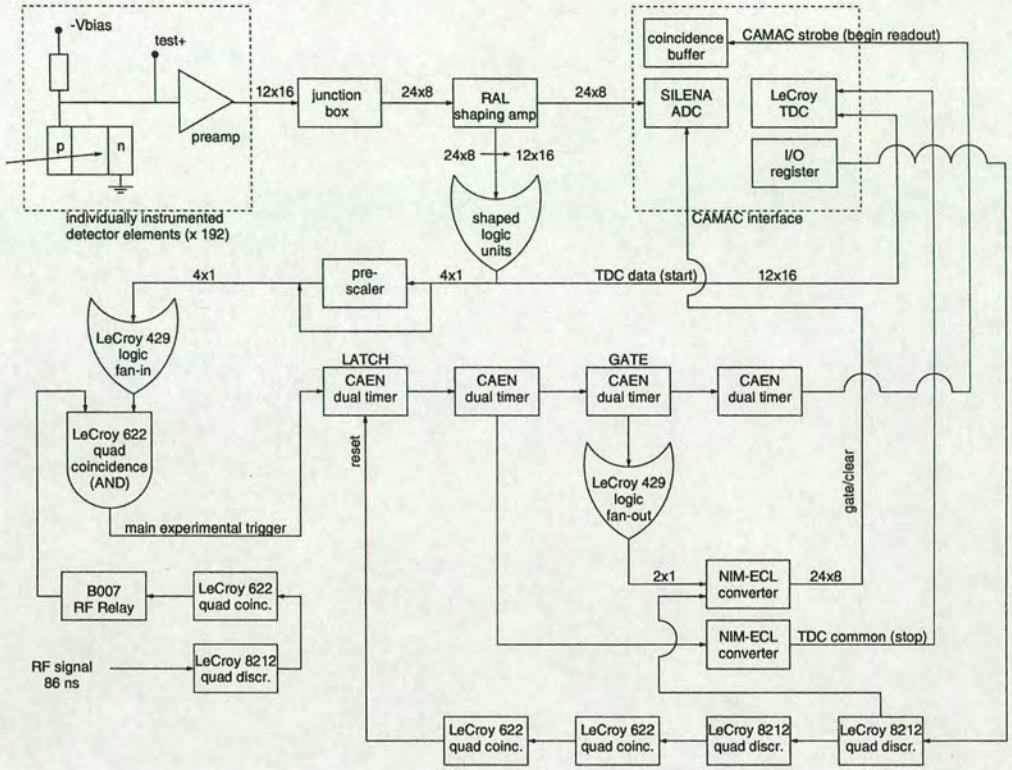

Figure 5.4: *Schematic of $^{21}Na+p$ experiment electronics setup.*

into binary words by the ADCs.

The logic signals also pass into a set of LeCroy 3377 CAMAC TDCs, which are set on common stop mode and are stopped by the accelerator HF signal. This means that the time of flight of detected particles with respect to the beam can be measured for the purpose of particle identification.

The CAMAC crates are interfaced to a VME processor which takes the sequentially read-out data from the CAMAC TDC and ADC conversions and increments the experimental on-line spectra, using the UK MIDAS software system, while also creating a raw data file in the local TRIUMF-MIDAS format.

The read-out time required for the CAMAC crates is a major factor

in the limitation of the data rate that can be accepted by the acquisition system. Dead times rise as the data rate becomes so high that the CAMAC crate becomes increasingly busy. A practical limit of around 3 kHz event rate is usually enough to cause problems in the acquisition, and dead times near this region can be large. Thus, efforts were made to limit the event rate to an acceptable level by the combination of the mylar foil, less backward sectors, and a reduced beam current than that maximally achievable.

5.3 Stable beam test run: ^{21}Ne+p

5.3.1 Beam production and tuning

It was decided to run a stable beam test experiment immediately prior to any radioactive beam measurement. The main reason is for the purpose of the energy calibration of the data using known resonances in the stable beam plus proton system, however, this test also serves as a good diagnostic experience for the experimental system, so that data rates, kinematics and noise levels can be monitored without wasting precious radioactive beam time.

^{21}Ne was chosen for various reasons: a) it is the isobaric equivalent to the proposed radioactive ^{21}Na beam, such that the scattering kinematics in the two experiments will be extremely similar. b) known resonances in the ^{21}Ne+p centre-of-mass energy system in a similar energy range to that of the proposed ^{21}Na+p study will enable calibration of the radioactive beam data. c) A ^{21}Ne beam is easily produced from naturally abundant Neon gas. d) The ^{21}Ne+p system provides a useful comparison for the isobaric analogue

state systems of ^{22}Ne, ^{22}Na and ^{22}Mg via its T=1 isospin states.

The beam was produced by allowing an amount of Neon gas into the OLIS ion-source. Here, a standard magnetron produces coherent microwaves which are guided into the gas chamber causing ionisation. The ions are extracted into the LEBT line and then into the RFQ. The ^{21}Ne is easily separable from other ions in the source because of its charge-to-mass ratio, thus only the desired isotope is accelerated through the RFQ. A final charge state of 5^+ was used in this experiment.

Two ^{21}Ne beam energies of 0.88 MeV/A and 1.35 MeV/A were used in this experiment, such that the energy loss range through the targets used would correspond to the region of selected known resonances in the ^{21}Ne+p system. After the setup of each beam by the accelerator operators, an initial low current tune would be made into the scattering chamber. Firstly, a blank target frame would be positioned at the target position and the current at the rear faraday cup be measured. Once 100% transmission was achieved through this aperture, the frame was replaced by a 2 mm diameter Aluminium collimator, and a further fine tune using the steering magnets and quadrupoles performed. Typical transmissions of 80% or more were achieved through the 2 mm collimator during this experiment.

5.3.2 Run sequence and data

$[CH_2]_n$ targets of thickness 250 μg/cm^2 were used during the two stable beam runs. During the 1.35 MeV/A run, 23 μm of mylar were used over both detectors, while for the 0.88 MeV/A run, 23 μm was used over the forward angle detector and 12 μm over the backward angle detector, to

lessen straggling of the lower energy scattered protons.

Data were taken over approximately 41 hours for each energy. Typical currents during the 1.35 MeV/A run were around 200 electrical pico-Amperes, which for a 5^+ charge state correspond to around 2.5×10^8 particles/sec. During the 0.88 MeV/A run, currents used were lowered at around 1.25×10^8 particles/sec due to the increased Coulomb cross-section at these energies resulting in a higher scattering rate.

Figure 5.5 shows an example of the data obtained from detector elements in the forward and backward angle detectors for the two beam energies. In this energy region, a pair of p-wave resonances are known [63]. We also see two peak structures at the low energy side of the spectrum, which are consistent with resonant inelastic scattering to the first excited state of ^{21}Ne.

5.4 ^{21}Na+p radioactive beam run

5.4.1 Beam production and tuning

The radioactive ^{21}Na beam was produced using the Silicon Carbide production target. Proton currents of around 4 μA were maintained on the target at energies of between 450 MeV and 500 MeV. The beam yield was measured at the ISAC yield station which is located between the mass separator and the LEBT line, where an Aluminised mylar tape is deposited with activity from the beam, and a scintillator and HPGe detector are used to examine β and γ decays in order to determine the amount of ^{21}Na deposited per second on the tape [64]. Several hundreds of millions of particles/sec of ^{21}Na were

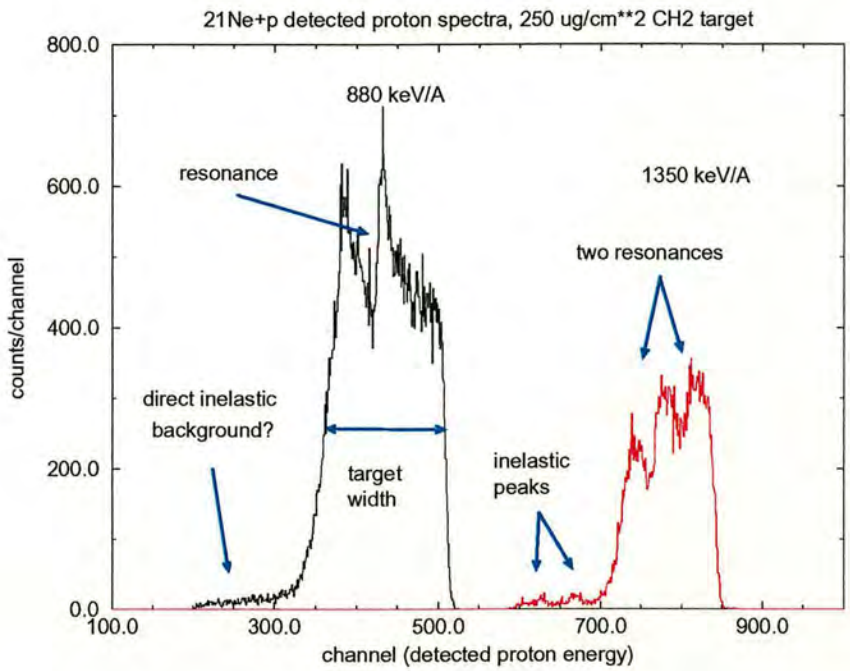

(a) 8.4°

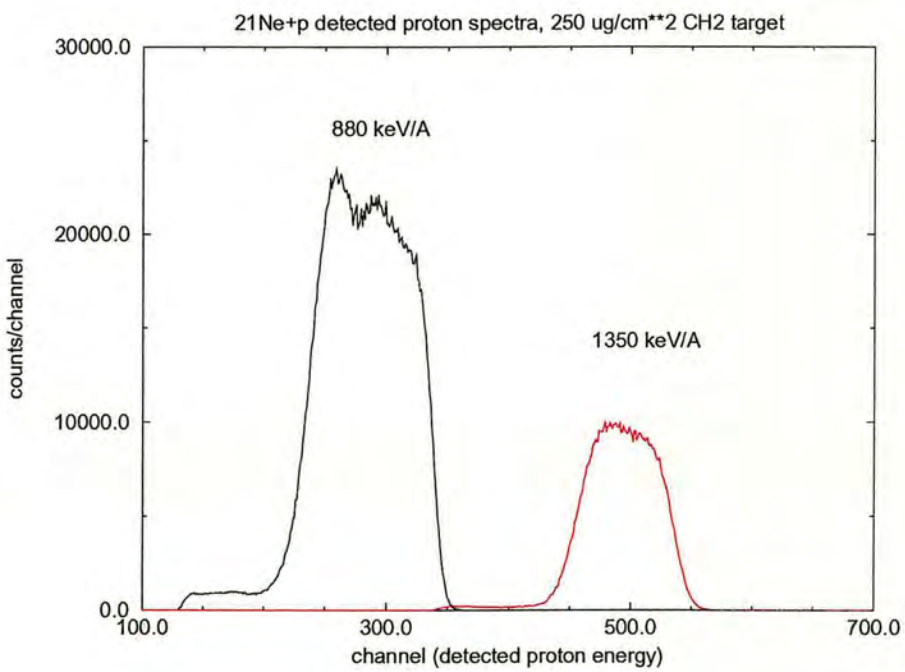

(b) 31.5°

Figure 5.5: *Sample proton spectra from $^{21}Ne+p$ scattering at 8.4° and 31.5° lab angles using the 250 $\mu g/cm^2$ $[CH_2]_n$ target.*

measured at the yield station, with up to 5×10^8 particles/sec measured after acceleration through the ISAC system as deliverable beam. The main diagnostic used to check the beam available to the TUDA chamber was a withdrawable Faraday cup located just upstream of the TUDA chamber.

5.4.2 Run sequence and data

In this experiment, the beam energies used varied between 0.58 MeV/A and 1.56 MeV/A. Because thick targets can scan a certain centre-of-mass energy range, a number of different runs and beam energies were chosen so that successive runs' spectra overlapped with the previous run in terms of the centre-of-mass energy covered by that scan. This resulted in a series of 10 thick target runs with 250 $\mu g/cm^2$ $[CH_2]_n$ targets. The beam energies used were 0.58, 0.69, 0.80, 0.88, 0.99, 1.144, 1.240, 1.340, 1.440 and 1.560 MeV/A. This covers a total centre-of-mass range of around 0.4-1.5 MeV.

Typical currents of around 5×10^8 particles/sec were employed on average during the experiment. The typical time spent at each energy was around 48 hours.

Figure 5.6 shows examples of some of the single-strip proton spectra taken during each of the thick target runs. In most cases, the β background has been removed for clarity, using techniques which will be fully described in the next chapter, however, for the lower energy beam runs, the proton spectra merge with the tail of the β-peak, as can be seen in the spectrum for the 580 keV/A run.

Initially, several features of the spectra are obvious. There are three definite large resonances visible in the spectra. In the 880 keV/A and 990

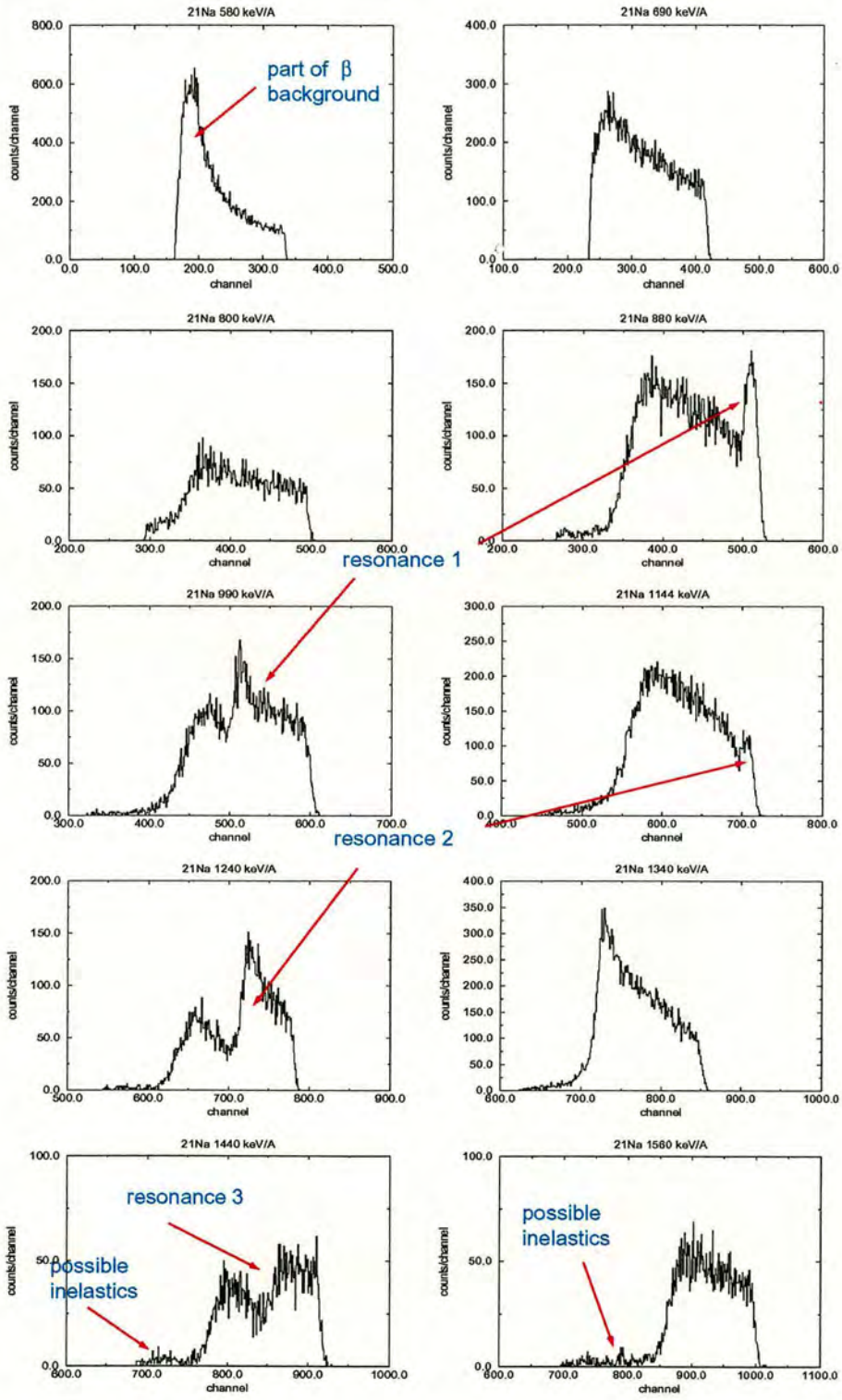

Figure 5.6: *Examples of single-strip proton spectra for all the thick target runs made, at a lab angle of 6.1°.*

keV/A runs, there is a large elastic resonance structure visible in the energy region where the spectra would overlap. In the 1144 keV/A and 1240 keV/A runs, there is a similar large elastic resonance structure in the overlapping region, and in the 1440 keV/A run there is a single elastic resonance structure. Possible regions where inelastic peaks might be observed are at the low energy sides of the 1440 keV/A and 1560 keV/A elastic peaks, although higher statistics are needed to verify this, and this is addressed in the next chapter. Also, inelastics might be expected at the low energy sides of the 1240 keV/A and 990 keV/A proton spectra, since there are elastic resonances there, indicating the existence of a compound nuclear state. Again, techniques must be employed to improve the data in order to reveal any underlying structure in these regions.

In order to try and reveal more structure in the resonance regions, some thin target runs using $[CH_2]_n$ targets of 50 $\mu g/cm^2$ were made at carefully chosen energies. Using the techniques described in chapter 4, it is possible to see inelastic peaks more clearly using these thin targets because with thicker targets, elastic protons from the rear of the target occur with energies similar to that of the inelastic protons, providing a background on which the inelastic peaks sit, while for thin targets, the interaction energy at the rear of the target is not low enough to produce elastic protons at energies as low as the inelastically scattered protons. The result of these thin target runs will be described in the next chapter.

Chapter 6

Data Analysis

In this chapter the procedure for extracting, sorting and calibrating the experimental data is described. The methods used to estimate the experimental resolution are discussed and the results from these used to calibrate the experimental data via the properties of known resonances in the ^{21}Ne+p system.

6.1 Data extraction and detector calibration

The raw data for each of the 192 detector channels were extracted into individual detector element spectra. The runs containing the data for the α-calibration source were then used to calibrate each detector element in energy[1]. Corrections for the energy loss of alpha particles in the Silicon dead layer (nominal manufacturer's figure of 0.35 μm for LEDA detectors) at each strip angle were included.

[1]The source was a standard open ^{239}Pu^{241}Am^{244}Cm α-emitter with a 2π coverage. These isotopes emit α-particles with energies of 5.15659, 5.48556 and 5.80477 MeV respectively.

Data collected using a pulser provides a means to calibrate the ADC offset for each channel. The offset and gain data for each channel are inserted into a FORTRAN user routine in the sort program, and the main experimental data sorted, enabling the energy of the detected particle to be calculated. This is however, the energy normalised to the α-particle calibration. It is known that Silicon detectors have a nonlinear response to ions of different Z. The difference in the pulse height of a proton and an α-particle of the same energy has been measured in ref. [65]. In calculating the true energy of a proton using the gain values of the α-calibration, we therefore include a factor 0.986 difference as suggested in the aforementioned reference.

2-dimensional spectra were produced for each energy run of particle energy versus TDC conversion. Figure 6.1 shows such a 2-dimensional energy versus time-of-flight plot for all strips in the forward angle detector. The isolated structure in the centre is the contribution from the protons, while the left hand side shows the β background from the radioactive beam, uncorrelated in time as expected.

A 2-dimensional gate was taken round the proton group leaving room at the low energy side in case low energy inelastically scattered proton events were present. The individual strip spectra are then only incremented if an event falls into this gate. The background due to the β tail at low energies is therefore substantially reduced.

Strips lying at equal angles in the detector array are considered as one entire entity, since we expect to gain no physical information by using azimuthal (ϕ) angular data in this experiment. Therefore, in the spectrum incremental procedure, events at the same angle are sorted into annular

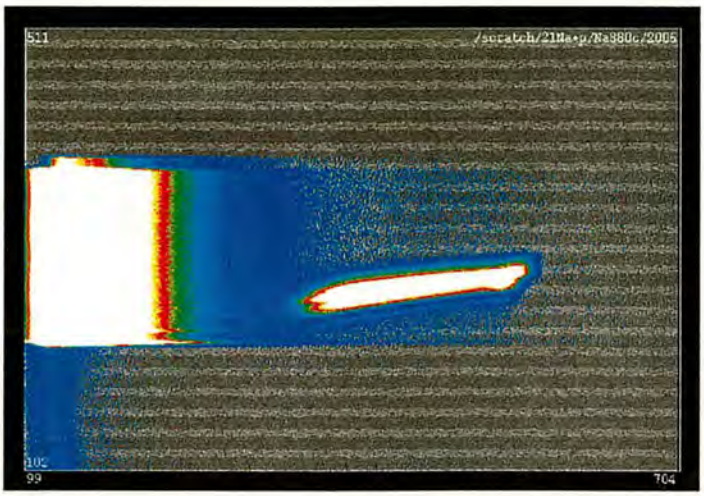

Figure 6.1: *Energy versus time-of-flight plot for the ^{21}Na+p 880 keV/A run.*

spectra, resulting in 32 separate spectra for each energy run.

The proton detected energy is the result of energy loss through the remaining section of the target, the mylar foil and the Silicon dead layer in the detector. Therefore, a reverse energy loss subroutine is implemented for each event to estimate the energy the proton would have after exiting the target. The proton energy after passing through the mylar can be approximated by a quadratic relation over the energy range of interest (see figure 6.2), and so the spectrum of detected protons will not reflect in a linear way the spectrum of scattered protons. Thus a calibration using the target edges as indicators of where the beam energy is would result in the correct centre-of-mass energies at the high energy edge of the target, but increasingly incorrect values towards the rear of the target. Therefore it is important to include an energy loss correction so that the spectrum is approximately transformed into a frame in which the proton lab energy is

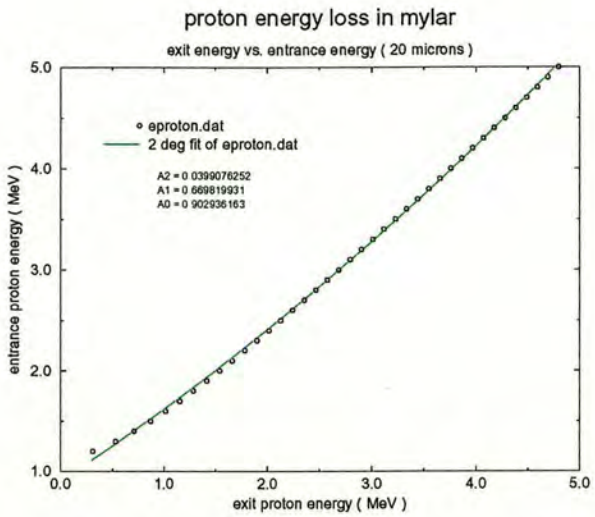

Figure 6.2: *Proton energy after passing through a fixed thickness of mylar foil, fitted with a quadratic relation.*

linear with the centre-of-mass energy, that being the proton lab energy at the moment of creation within the target. Since the energy loss out of the target is small[2], and we cannot be sure where in the target the event came from, we use the approximation that the proton energy on exit from the target is linear with the centre-of-mass energy.

At this point the proton spectra are un-normalised and uncalibrated to centre-of-mass energy. Figure 6.3 shows the uncalibrated and un-normalised spectra from one annulus of the forward angle detector.

[2]For example, a 3 MeV proton travelling through the entire target would lose approximately 30 keV, ie. 1%.

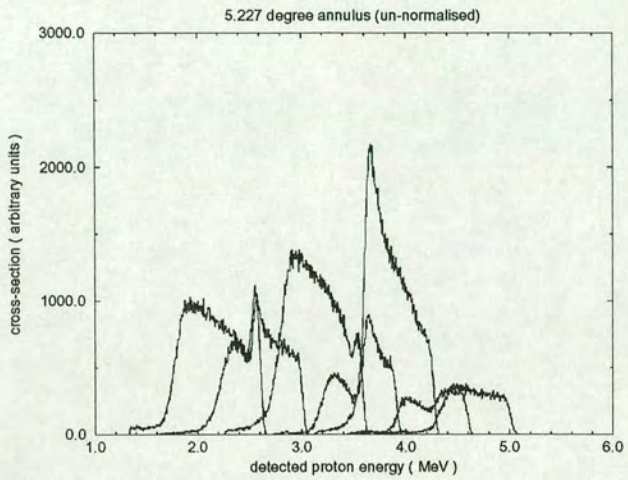

Figure 6.3: *Example proton spectrum at 5.2° before normalisation and calibration to centre-of-mass energy showing the separate thick target runs at different beam energies.*

6.2 Calibration and analysis of spectra

6.2.1 Target effects

In order to be able to calibrate the spectra to the centre-of-mass system, it is essential to try and understand the effects caused by the use of a thick target scan technique as described in chapter 4. In this work, the target itself has been modeled as a top-hat function in the beam energy loss system. For energies from the entrance beam energy down to the mean energy of the beam at the exit of the target, it is assumed there is a uniform distribution of target nuclei available for reaction. This can be transformed into a top-hat function in the centre-of-mass energy system. Effects such as the reduction of Hydrogen at the edges of the target, which could be possible, have been

ignored in this work, and would be difficult to measure[3].

The beam energy distribution can be modeled as a Gaussian with an energy spread corresponding to approximately 0.3% of the total energy for an average beam [60]. Therefore, we term the *target function* a convolution of the beam energy distribution with the top hat function, resulting in a trapezoidal function with edges determined by the convolution of the beam Gaussian with a step. The straggling of the beam in the target has the effect of redistributing the beam energies as the beam travels through it, thus the variance of the convoluting Gaussian increases into the target, resulting in a rear edge which is less sharp than the front edge of the target. Since the straggling variance of a typical ^{21}Na beam into these targets reaches values of only around 50 keV in the lab frame, the plateau top of the target function will remain unaffected since the width of the convoluting Gaussian is small compared to the convolution range over the target.

The effect of reduction in beam flux through the target has been ignored since the number of scattered beam particles at each target depth is very small compared to the total incident flux. (For example a typical beam will have only a few percent at most removed from the flux over the entire target). The resulting *effective yield function* would be a multiplication of the target function (its maximum value being unity) and the differential cross section function.

Figure 6.4 shows the target function, where the beam is convoluted

[3]A suggested method to do this would be to measure the energy spectrum of protons scattered from the target using a well defined beam in a regime where the cross-section is known to be Coulomb. Any deficit in target nuclei at the edges should show as a shape change in the edges of the proton spectrum. No such effect was obvious in this experiment, although there were other effects affecting the target edges which will be discussed.

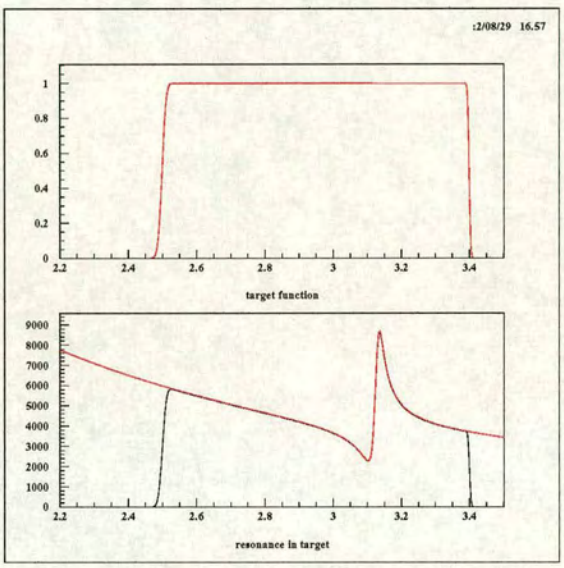

Figure 6.4: *Top-hat type function used to represent the target for a typical beam energy (top), and the effective yield function (black) with the resonance curve used superimposed (bottom).*

with the top-hat function, and the resulting effective yield function[4] after the resonance is multiplied by the target function. This is in effect the yield one would measure if no straggling or energy loss occurred to the proton after it recoiled, and the measurement was made with an ideal point-like detector at a discrete angle.

Several effects then contribute to the further spreading of the experimental data after the proton recoils from the elastic event:

1. The proton loses energy through the remainder of the CH_2 target resulting in a straggling distribution.

2. The proton loses energy through the mylar foil resulting in a straggling distribution.

3. The detector dead layer further reduces and straggles the proton energy before it enters the active part of the Silicon detector.

4. Each strip subtends a finite angular range introducing a kinematic angular spread in the proton energy.

5. The electronic noise inherent in the instrumentation and Silicon dark current produces a further spread in the magnitude of the amplified signal.

The effects associated with energy loss straggling can be estimated by using the Bohr straggling formalism. In this formalism the variance in energy results mainly from electronic collisions in the material where the resulting

[4]Note that y-axis values are expressed in arbitrary units

energy distribution is Gaussian around the mean energy. For nonrelativistic heavy particles this is given by

$$\sigma_0^2 = 0.1569\rho\frac{z^2 Z}{A}x[MeV^2] \tag{6.1}$$

where ρ, Z, A and x are the density [g/cm^2], proton number, mass number and thickness [cm] of the stopping medium, respectively, and z is the proton number of the ion [66]. This rule only applies when the medium is thick enough that large numbers of collisions are made and that the energy loss is small compared to the initial energy.

The effect of angular spreading can be estimated by differentiating the kinematic formula of the energy of a recoiling proton, and is given by

$$\Delta E = 2E\tan\theta_{lab}\Delta\theta \tag{6.2}$$

The electronic noise can be measured directly as the average spread in the peak signals obtained during the pulser calibration. This is estimated at about 8 keV in the lab for a typical channel.

Other effects such as the multiple scattering of the beam and the protons through the target and mylar can contribute to the overall experimental resolution, as can the effect of momentum dispersion in the beam and thickness variation in the mylar foil. In this work these effects, which are difficult to calculate, have not been included explicitly. Instead, the variances of all the contributing factors are added in quadrature resulting in an experimental

Gaussian resolution with variance given by

$$\sigma_{exp} = \sqrt{\sigma^2_{CH_2} + \sigma^2_{mylar} + \sigma^2_{deadlayer} + \sigma^2_{noise} + \sigma^2_{\theta} + \sigma^2_{u}}$$

where σ_u represents unknown factors such as multiple scattering, beam dispersion and thickness variation.

6.2.2 Simulation of experimental data

In order to investigate further the effect of different physical events on the experimental resolution of the final spectra, a Monte Carlo simulation was constructed to simulate the experimental data. The details of the experimental resolution determination procedure are presented in Appendix C. The aim of this simulation was to find an empirical method of determination of the experimental resolution using fits of the high energy edges of the proton spectra.

Table 6.1 shows the resolution parameters resulting from Gaussian fits of the spectrum edges (from here on called target edges) and the resonance fits to the data for each beam energy used in the simulations. Also tabulated are the beam energy spreads used in the simulation[5].

It can be seen that the spread of the target edges increases with beam energy, which is expected due to the increasing energy spread of the beam involved. The resolution[6] determined from the fit of the resonances to the

[5]These beam energy spreads are 1.5 times larger than the actual spreads in the experiment, which are interpolated from Figure 20. in ref. [60].

[6]Defined as the width of the Gaussian required to convolute with the resonance curve in order to fit the data.

Beam Energy (MeV/A)	Target Edge Sigma (keV)	Resolution Fit Sigma (keV)	Beam Sigma (keV)
0.69	7.42	5.75	2.14
0.88	8.09	5.82	2.95
0.99	8.33	5.72	3.46
1.114	8.95	5.75	4.23
1.240	9.26	5.83	4.74
1.340	9.75	5.68	5.30
1.440	10.31	5.86	5.89
1.560	11.01	5.73	6.62

Table 6.1: *Various resolution parameters resulting from fits on simulated experimental data.*

simulated data show only small variation and no systematic trend, and can be considered constant to within 0.2 keV. It can also be seen that the target edge spread is *not* given by the quadratic sum of the resonance spread and the beam spread, as might be expected, but instead is larger. This point is important and attention will be paid to it in section 6.2.5. The results of the simulation are used in section 6.2.5 to estimate the spreading effects present in the real experimental data.

6.2.3 Calibration to centre-of-mass system

In order to use the target edges as an initial means of calibration, we fit the edge of each individual annular spectrum with a Gaussian. This results in a series of values of centroid position[7] with an associated error of around ± 2 channels[8]. This corresponds to ± 10 keV in the proton lab frame.

The proton energy is plotted against the centre-of-mass energies of the

[7]Taken from the mean plus half the full width at half maximum value of the Gaussian fit

[8]Estimated by assuming that when making the Gaussian edge fits, will choose the correct fit lower limit to within ± 3 channels

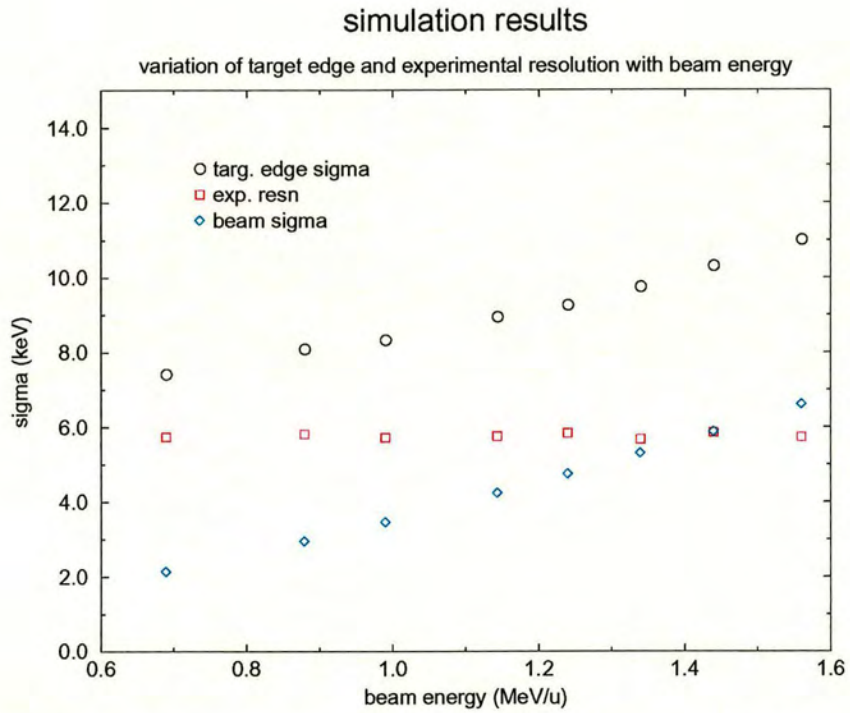

Figure 6.5: *Plot of experimental resolution parameters resulting from fits on the simulated data and beam resolution used in simulation.*

beam. Table 6.2 shows the values in the ^{21}Na + p centre-of-mass system of the beam energies. The combined systematic error in the beam energy value is estimated to be about ±5 keV/A [67]. Since the proton energies have been corrected for energy loss through the mylar and Silicon and not the target material, the form of the proton energy versus the centre-of-mass energy relationship is expected to be non-linear by a small amount. Therefore the target edge data are fitted with a polynomial of order 2 for each annular spectrum. Figure 6.6 shows an example of a typical calibration curve for one detector annulus. The order 2 coefficient is small, and so the fit is almost linear. The quadratic relations derived from the fits are used to transform the spectra into the centre-of-mass frame. The quadratic fit is of the form

$$E_{cm} = aE_{lab,det}^2 + bE_{lab,det} + c$$

The fits also result in a set of errors for the parameters a, b and c. The error in the centre-of-mass calibration is then given by the propagation of errors formula:

$$\sigma_{E_{cm}}^2 = \sigma_a^2\left(\frac{\partial E_{cm}}{\partial a}\right)^2 + \sigma_b^2\left(\frac{\partial E_{cm}}{\partial b}\right)^2 + \sigma_c^2\left(\frac{\partial E_{cm}}{\partial c}\right)^2 \qquad (6.3)$$

Using typical values for the parameter errors, this gives a centre-of-mass energy error at a typical centre-of-mass energy as ±10 keV. This is the error in the centre-of-mass given that actual beam energies could each be incorrect relative to the chosen beam energy by an amount ±5 keV/A.

Beam energy (MeV/A)	Centre-of-mass energy (MeV)
0.69	0.6636
0.80	0.7694
0.88	0.8463
0.99	0.9521
1.144	1.1003
1.240	1.1926
1.340	1.2888
1.440	1.3849
1.560	1.5003

Table 6.2: *$^{21}Na+p$ centre-of-mass system beam energies.*

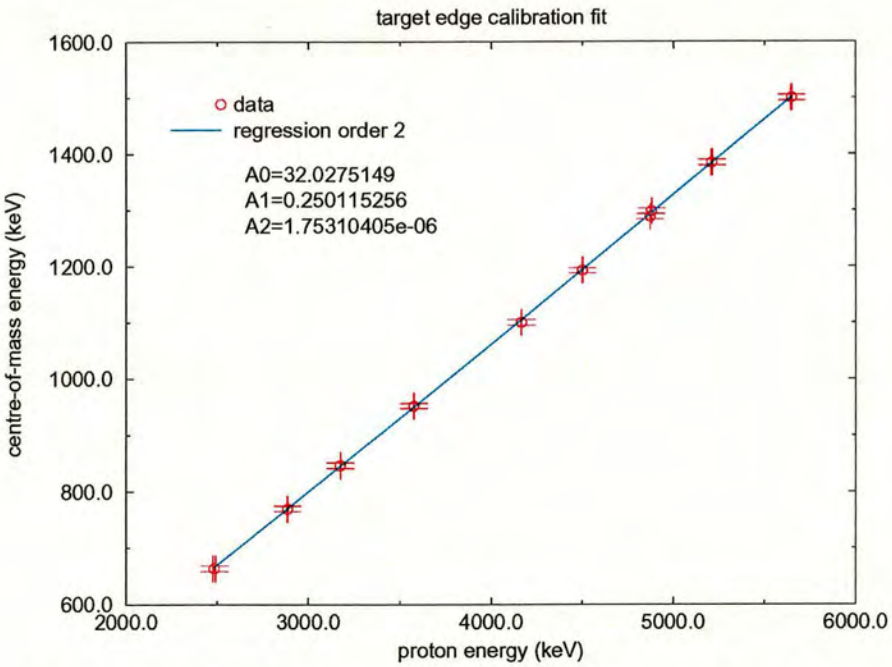

Figure 6.6: *Example of centre-of-mass calibration using target edges.*

6.2.4 Normalisation of thick target runs

In order to deduce resonance parameters from the fitted data, it is essential to fit all of the separate thick target runs simultaneously. This ensures that all resonances present are being included in the fit and therefore interference between all resonances is taken into account using the R-Matrix formalism.

The spectra from separate energy runs are un-normalised due to the different durations and beam intensities used. The sector of the backward angle detector which was unprotected by the mylar foil was used as a means of approximate normalisation. The recoil ^{12}C and proton peaks detected in this low-gain sector were used to estimate the number of incident ions during each run, correcting for the effect of Hydrogen depletion in the target. This normalisation has an estimated associated error of around 10% due to the uncertainties involved in the determination of the integral counts under the ^{12}C and proton peaks, and by uncertainties in the target thickness. Using the target model described in section 6.2.1, we can say that since neighbouring target runs overlap in terms of energy by a significant amount, each run must match its neighbour at the point of overlap. Therefore, adjustments within the estimated 10% error in normalisation can be made until the runs match with each other. These adjustments can be made in the data fitting program. The data are also normalised to take into account the different solid angular areas of each detector annulus.

6.2.5 Determination of experimental resolution

In order to make a correct fit to the experimental data with an appropriate functional form of the theory, the degradation of the yield curve by experi-

mental effects needs to be considered. The processes of proton straggling and angular kinematic broadening described previously are the major contributors to the degradation of the spectra. These effects have been considered in other heavy-ion on proton elastic scattering experiments [59] [57], in which the resultant total degradation of the proton spectrum was modeled by a Gaussian convolution of the theoretical yield curve, the Gaussian having a constant width over the range of the target involved. The data fitting method was then to fit the convoluted yield curve rather than to try and perform difficult deconvolutions of the data. This is essentially the method employed in this work.

Slight differences in approaches between this work and refs. [59] and [57] were introduced in order to try and improve the data fitting. Essentially, the experimental resolution was empirically determined via the study of the Monte Carlo simulation data and the experimental proton spectra. Due to the form of the proton spectra upper edges, it is expected that the shape of the beam energy distribution and the overall experimental resolution determine the shape of this edge. The target edge fits referred to in table 6.1 were used to deduce an empirical relationship between the beam spread, experimental resolution, and target edge fit width. As mentioned in section 6.2.2, the target edge spread, σ_e is not the quadratic sum of the other two parameters, but instead larger. Therefore, an unknown spread function, $f(\sigma_{beam})$ was introduced such that $\sigma_e^2 = f^2(\sigma_{beam}) + \sigma_{exp}^2$, since for a given experimental setup, the edge shape should only vary significantly as a function of beam resolution. Also, as seen in the resonance fits to the simulated data, the experimental resolution does not vary strongly with beam energy since Bohr straggling is an energy-independent process in this scenario.

Figure 6.7 shows a linear approximation to the function $f(\sigma_{beam})$ which was employed since the true functional form of the relationship is unknown. The errors in this fit arise mainly from the uncertainty in the simulation fits themselves. The next step is to use the values of the target edge widths extracted from the real data to estimate the experimental resolution using:

$$\sigma_{exp} = \sqrt{\sigma_e^2 - f^2(\sigma_{beam})} \tag{6.4}$$

In this process the average values of σ_e over the first seven strips of the detector are used[9], and converted into centre of mass values. The propagation of errors gives the overall uncertainty in the estimated experimental resolution as:

$$\Delta_{exp}^2 = \Delta_e^2 + (\Delta_{p_1}\sigma_{beam} + \Delta_{p_2})^2 \tag{6.5}$$

where p_1 and p_2 are the slope and offset of the linear function, f. The major contribution to the errors however is the uncertainty in the target edge spread Δ_e. These uncertainties were found to be very similar over different angles of a given energy run, and so the average of Δ_e from a sample of strips in each run was used in the estimation of Δ_{exp}. The values of the beam resolution used were estimated by interpolating the relationship between beam energy and beam resolution from ref. [60], where the values are quoted for a beam of emittance $\epsilon_z = 1.5$ keV/A·ns, and scaling for a

[9]The angular uncertainty does not increase significantly over this angular range.

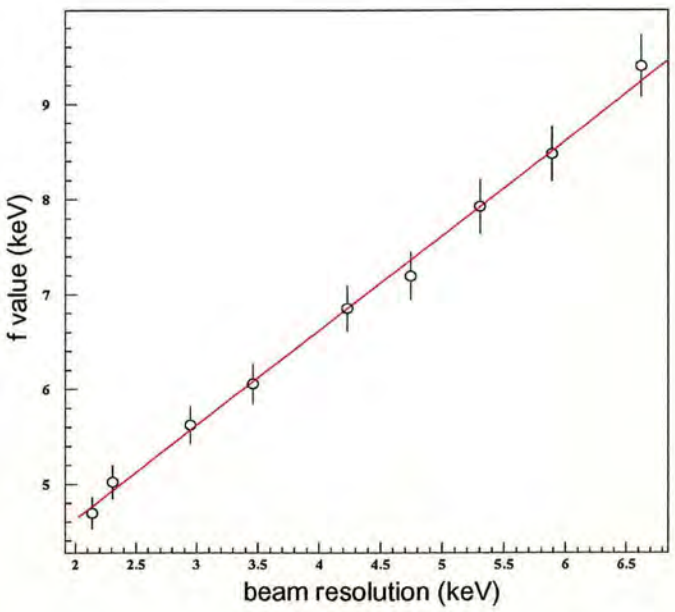

Figure 6.7: *Linear approximation to functional dependence of the unknown function, f, with beam energy resolution.*

beam emittance of 1.2 keV/A·ns as used in the experiment. The resulting estimated experimental resolution parameters and associated errors can be seen in table 6.3.

6.2.6 Calibration using ^{21}Ne+p resonance

The experimental run using the ^{21}Ne beam resulted in data being collected for an s-wave resonance at $E_{cm} \simeq 733$ keV. This resonance has been extensively studied in previous work [68] [63] [69] [70] [71] [72].

The adopted value for the resonance energy is taken from the results

Beam energy (MeV/A)	Estimated exp. resolution (keV)
0.69	4.46 ± 0.54
0.80	4.99 ± 0.68
0.88	5.07 ± 0.73
0.99	5.73 ± 0.77
1.144	5.75 ± 0.71
1.240	5.86 ± 0.81
1.340	5.83 ± 0.86
1.440	6.14 ± 1.11
1.560	9.32 ± 1.52
0.88 (^{21}Ne+p)	5.38 ± 0.66

Table 6.3: *Estimated experimental resolution values at the upper edges of the proton spectra.*

of ref. [68], and is that also used in ref. [72]. The only other independent measurements of the resonance energy using either ^{21}Ne(p,p)^{21}Ne or ^{21}Ne(p,γ)^{22}Na measurements are in refs. [63] and [69], who give values of 736.6 keV and 733.2 keV respectively[10]. Ref. [69] agrees within errors with the adopted value. The accelerator used in this work was calibrated using the reactions ^{13}C(p,γ)^{14}N and ^{27}Al(p,γ)^{28}Si , while ref. [63] used the reactions ^{14}N(p,p), ^{15}N(p,$\alpha\gamma$) and ^{19}F(p,$\alpha\gamma$).

The adopted total width of the state is $\Gamma = 4 \pm 0.4$ keV, while the only information available on the proton partial width of the state is given in ref. [63], where it was deduced as being $\Gamma_p = 2 \pm 1$ keV. However, it is interesting to note that the total width is the result of (p,γ) yield experiments, while the proton width was deduced from fitting elastic and inelastic ^{21}Ne+p scattering data. The latter reference seems to have been ignored in the major compilations, and yet is the most relevant experimental method to be compared to the elastic scattering of this work.

[10]Actual values quoted in these references were in terms of proton beam energy with values of 772±1 keV and 768.4±1.2 keV respectively.

Data from the 880 keV/A ^{21}Ne+p run, which contains the 733 keV resonance, were normalised and calibrated using the methods described in the previous sections. A simple Breit-Wigner formalism similar to that used in the Monte Carlo simulations was used to make a preliminary fit to the resonance. The partial width was set at 2.7 keV, as it was found that this achieved the best fit. The normalisation constant and convolution width (which was set constant over the energy range of the target) were left as free parameters along with the resonance energy. The purpose of this preliminary fit was to find small magnitude correction terms between annular spectra in terms of energy and normalisation. Figures 6.8 and 6.9 show the fit results for the first fifteen annuli of the forward angle LEDA detector. The mean values of the resonance energy and normalisation over all these individual fits were taken, and corrections made in the calibration equation to account for these shifts. The best-fit values of the convolution parameter vary, but the average value over all the 15 strips is 5.39 keV, which agrees well with the average convolution determined for the ^{21}Ne+p target edges of 5.38 keV.

Because there is another resonance close to the 733 keV resonance, it is insufficient to derive the actual resonance properties using a Breit-Wigner formalism. The nearby[11] s-wave resonance lies at 670 keV, and is known to have a partial width $\Gamma_p \leq 2$ keV from ref. [63]. The single-channel R-Matrix code described in the next chapter was used to make a fit to the two ^{21}Ne+p resonances using the experimental resolution parameters determined in section 6.2.5. The fit was made over fifteen angles of the forward LEDA

[11]Note that there is also a p-wave resonance lying at 684 keV, which was not observed in this experiment but which is known to have a total width of $\Gamma = 2.5 \pm 0.5$ keV. This resonance was not included in any of the fits made in this work. It is thought that this resonance was not observed due to its small strength in the elastic channel.

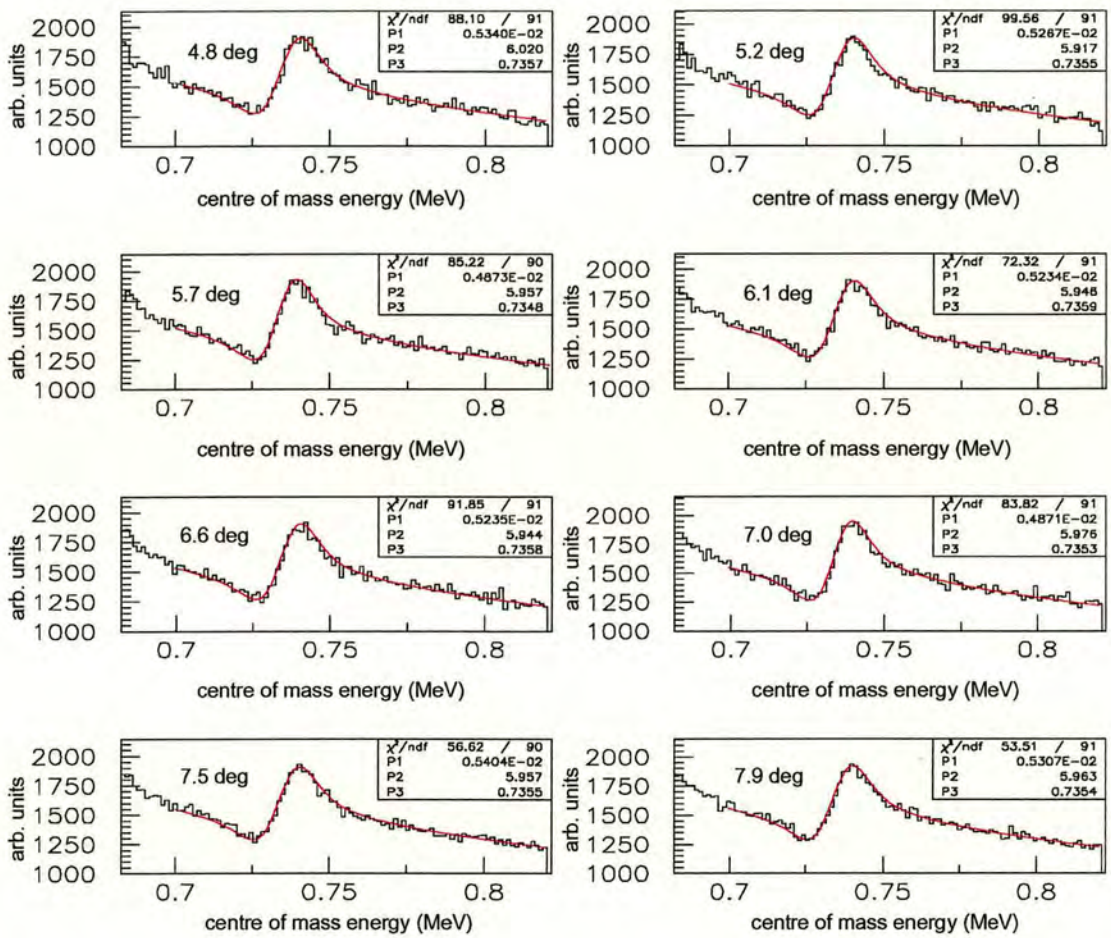

Figure 6.8: *Breit-Wigner fits to the $^{21}Ne+p$ 733 keV resonance for the inner eight annuli of the forward angle detector.*

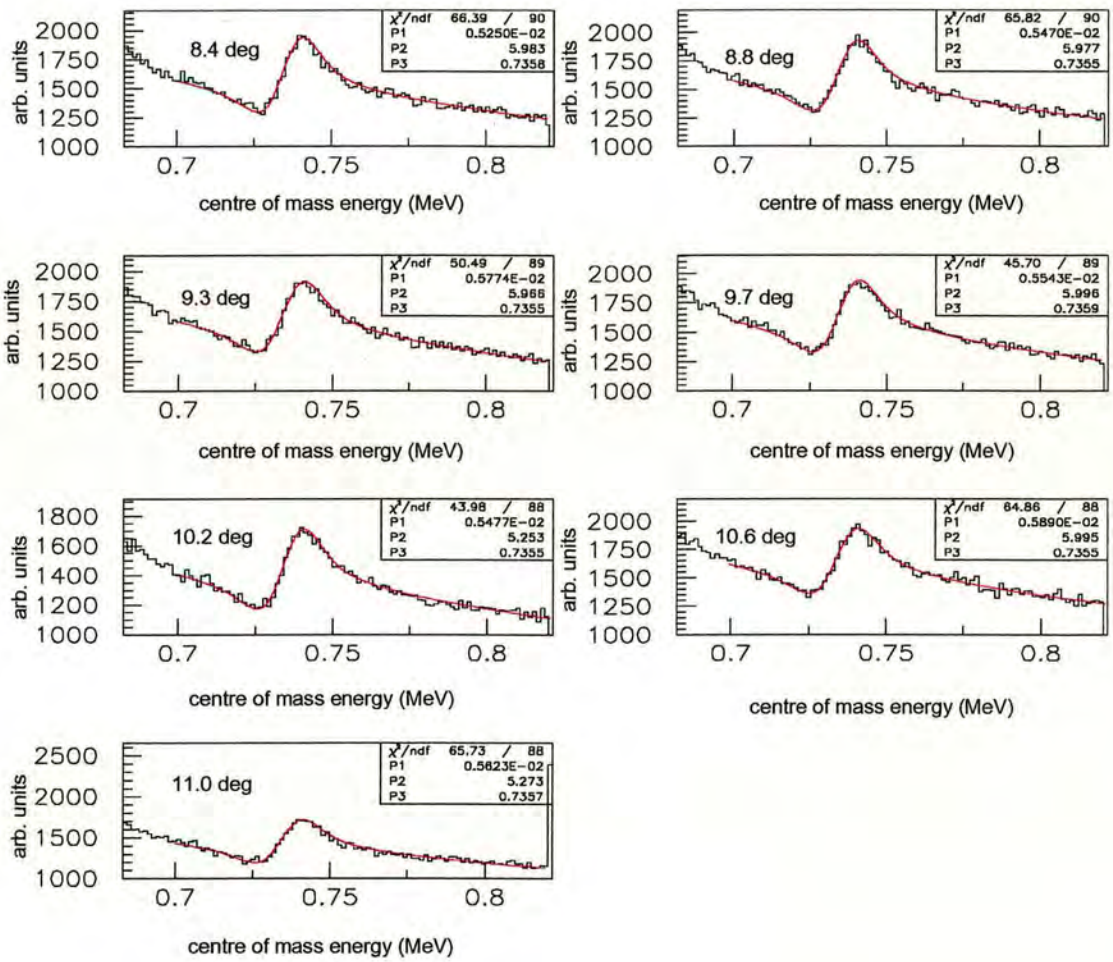

Figure 6.9: *Breit-Wigner fits to the $^{21}Ne+p$ 733 keV resonance for the outer seven annuli of the forward angle detector.*

detector, rejecting the sixteenth due to bad data caused by instrumentation problems in some of the outer annulus detectors. LEDA 2 data was not included in the fit due to the fact that the fitting program is only designed to handle up to sixteen data sets at one time.

The fit resulted in a global reduced chi-squared of $\chi^2_\nu = 1.192$. The R-Matrix state energy corresponding to the 733 keV resonance was $E_1 = 735.06 \pm 0.44$ keV. Because the $\ell = 0$ boundary condition was evaluated at E = 735.05 keV, the state energy is identical with the resonance energy to within 0.01 keV.

The difference between the adopted value of the resonance energy and the fit value is 2.36 ± 0.94 keV, taking into account the ± 0.5 keV error on the adopted value. This difference was then used to apply offset corrections to the ^{21}Ne+p and ^{21}Na+p data.

6.2.7 Inelastic corrections

Peaks on the low energy sides of the proton spectra were identified as protons from inelastic scattering with the first excited state of ^{21}Na at 331.93 keV. In order to correct kinematically into the *incident* centre-of-mass energy frame, the following procedure was adopted:

The spectra were calibrated as were the elastics, using the quadratic target edge relations derived from the target edges, and using the same calibration corrections derived from the ^{21}Ne+p fits from above. This places the data in a frame of elastic centre-of-mass energy events. By doing this we are "pretending" that the protons are actually from an elastic event, in order to work back from the quadratic fit what their actual energies were

after scattering. No physical properties of the inelastic events are changed in this way, we are simply using the calibration mapping to infer the actual proton energies in the primary spectrum.

The relation between the energy of an inelastically scattered proton and the incident centre-of-mass energy, E, is given by (see Appendix B):

$$E_{p'} = \left[\frac{\cos\theta_{lab} \left(\frac{m_1+m_2}{m_1} E \right)^{1/2} + \left(\cos^2\theta_{lab} \frac{m_1+m_2}{m_1} E - (1+m_2/m_1)E_x \right)}{(1+m_2/m_1)^2} \right]^2 \tag{6.6}$$

This can be rearranged for E, allowing the centre-of-mass energy in the entrance channel of the inelastic event to be inferred. The spectra were corrected in this way, and where required, normalised to the corresponding thick target data.

Chapter 7

Results and Interpretation

In this chapter the specific procedure of fitting the data using a single-channel R-Matrix code is described. The code is used with the ^{21}Ne+p scattering data to extract a width and resonance energy corresponding to a T=1 state in ^{22}Na. The ^{21}Na+p scattering data is then analysed in an attempt to extract widths and resonance energies corresponding to states in ^{22}Mg. The inelastic scattering data is also considered, leading to estimations of resonance total widths where elastic assignments are not possible.

Using the information gained from the analyses, the ^{22}Mg nuclear structure aspects are briefly discussed, with reference to each state observed in the experimental data. A discussion of the astrophysical implications of these ^{22}Mg structure properties then follows.

7.1 Development of single-channel R-Matrix code

The single-channel R-Matrix code used in this work was based on an existing code which included the spin-zero formalism of ref. [73]. The code was largely modified and customised to fit the particular physical scenario of ^{21}Ne or ^{21}Na scattering on protons. Appendix B contains the derivation of the single-channel $\ell = 0$ form of the general R-matrix equations from ref. [11], and the resulting equations were used to calculate the energy dependent differential cross-section in the code.

The experimental resolution values determined in the previous chapter were used in the code to provide a physically correct form of modification of the theoretical yield curve, with the width of the convoluting Gaussian varying with energy, depending on which beam energy run the data comes from.

An arbitrary boundary energy E_{bnd} is chosen at the beginning of the program, and the values of the penetration, $\mathcal{P}$, and shift, S, are calculated at this energy. The boundary parameter is defined as $\mathcal{B} \equiv S(E_{bnd})$. All values not dependent on the R-Matrix parameters are then calculated for each data point, such as the Sommerfeld parameter, the wavenumber, penetration and shift, and the hard-sphere and Coulomb phase-shifts. These values are associated with their respective data points.

At this point the main program calls the minimisation routine to minimise the χ^2 of the cross-section with respect to the data points, using the single-channel expressions. Inside the subroutine, for each data point, the cross-section is calculated using the relevant Coulomb, Resonant and Inter-

ference terms, and combined with the convolution and a free normalisation parameter. The χ^2 is calculated, and the results passed to the minimisation routine.

Any number of free parameters can be included in the fit. In this work the main free parameters were the state energies and reduced particle widths of the R-Matrix. The ℓ-value of each resonance and therefore the spin-parity assignment of each state in the fit is set as an input parameter. A normalisation free parameter is required to ensure matching of the spectra with the absolute cross-section values.

Once the minimisation has occurred, the state energies and widths are transformed into the resonance energies and proton widths using the formalism of ref. [74]. It can be stated that for every set of R-Matrix formal parameters (state energies, widths) associated with a given boundary parameter, there exists a complementary set of parameters associated with a different boundary parameter which result in the same physical values of the cross-section. This transformation is done by constructing a matrix with the elements [12]

$$C_{\lambda\mu} = E_\lambda \delta_{\lambda\mu} - \sum_c \gamma_{\lambda c}\gamma_{\mu c}(\mathcal{B}_c - \mathcal{B}'_c) \tag{7.1}$$

where λ, μ denote state properties and c is the channel index. $\mathcal{B}'$ and $\mathcal{B}$ represent the new basis and current boundary parameters respectively. Since we fit with a single-channel formalism, the sum is dropped. The eigenvalues and eigenvectors $D_\lambda, \mathbf{K}$ of the matrix are calculated, so that the new set of R-Matrix parameters are given by

$$E'_\lambda = D_\lambda, \gamma' = \mathbf{K}\gamma \tag{7.2}$$

The state energy is equal to the resonance energy when the boundary parameter is equal to the shift function evaluated at the resonance energy. Thus the procedure is to iterate the boundary energy, calculating the new values of state energy and width, until the state energy is equal to the boundary energy for that resonance. Then the procedure is repeated for the next resonance etc.

The observed proton width of a state is given by equation 2.32, and so on convergence of the state energy and boundary energy, the proton width is calculated using the current value of the reduced width. Note that other methods exist [75] for multi-state boundary calculations which facilitate the use of the observed widths and energies in the calculation rather than the formal parameters. However, these methods involve the handling of prospectively large matrices within the program substructure. Approximations to the above method also exist for the R-Matrix *single level approximation*, where the observed widths and energies can be calculated iteratively without the construction of large matrices [76].

7.2 Data fitting: ^{21}Ne+p

The single-channel R-Matrix code was first used to re-fit the calibrated and corrected ^{21}Ne+p data over the fourteen inner angles. Values of the minimised χ^2_ν for different convolution parameters were investigated around the

mean value of 5.38 keV estimated in section 6.2.5. Table 7.1 shows the resultant values for these fits. In column 1, the actual value of the experimental resolution at the target edge entered into the fitting program is shown. Column 2 shows this same value in terms of its difference in units of σ, the standard deviation error calculated from the target edge fits, from the mean value. It is seen that the resonance energy as calculated using the boundary transformation techniques detailed in the previous section, is constant over this range of input convolution parameters. Figure 7.1 shows the χ^2_ν and proton width variation for these different values of convolution parameter. It can be seen that the χ^2_ν function is minimised at around a value of $\sigma_{exp} = 5.49$ keV, corresponding to a value of $\Gamma_p = 2.51$ keV. The proton width varies monotonically with the convolution parameter. It is expected that the error in Γ_p may be a complicated function of all the variables involved in the fit. However, the fact that the width varies monotonically with the convolution parameter, and the χ^2_ν follows a valley-like function, allows the error in Γ_p to be associated with the error in σ_{exp}.

For this series of fits, the convolution parameter which minimised the χ^2_ν was $\sigma_{exp} = 5.49$ keV. The 1σ error values of σ_{exp} are given as 4.72 keV and 6.04 keV, so that the values of Γ_p corresponding to these limits provide our 1σ error points for proton width. Thus, the value of the proton width of the 732.7 keV resonance can be written as $\Gamma_p = 2.5 \pm 0.2$ keV.

The results of these fits confirm that the calibration offset of the data using the previous R-Matrix fit is succesful in that the adopted resonance energy value of 732.7 keV is derived from the fits. Also, the fitted proton width agrees with the published value within the 1 keV error associated with that value. The results also add confidence to the method of determining the

σ_{exp} (keV)	$\sigma_{exp} - \sigma_{mean}$	E_R (keV)	Γ_p (keV)	χ^2_ν
4.06308	-2σ	732.7	2.155	1.954
4.39308	$-3\sigma/2$	732.7	2.215	1.717
4.72308	-1σ	732.7	2.331	1.397
5.05308	$-\sigma/2$	732.7	2.425	1.227
5.21808	$-\sigma/4$	732.7	2.447	1.201
5.38308	0	732.7	2.470	1.198
5.49308	$+\sigma/6$	732.7	2.509	1.170
5.54808	$+\sigma/4$	732.7	2.544	1.174
5.60308	$+\sigma/3$	732.7	2.550	1.179
5.71308	$+\sigma/2$	732.7	2.568	1.195
6.04308	$+1\sigma$	732.7	2.657	1.269
6.37308	$+3\sigma/2$	732.7	2.693	1.380
6.70308	$+2\sigma$	732.7	2.808	1.558

Table 7.1: *^{21}Ne+p R-Matrix fit results.*

experimental resolution using the target edges, showing that the estimated value is very close to that which provides the best fit.

Note that although the 670 keV resonance was included in the fit, very few of the data points actually lie over this resonance. Consequently, the values of the resonance energy and width for this state have been omitted from this work. It is expected that an additional thick target run of 150-200 keV lower beam energy would be required to provide data points sufficient to cover the region of this resonance, enabling a determination of energies and widths.

In the literature, in particular, the compilation of ref. [77], there is an ambiguity present in the spin-parity assignments in the compound nucleus ^{22}Na. The particular levels of interest to the ^{21}Ne+p fit, as mentioned above, correspond to excitation energies of E_x=7239 and 7277 MeV respectively. In ref. [77], these have been assigned spin-parities of (2^+ to 4^+) and (1^-,2^+) respectively. These assignments are mainly based on studies of (p,γ) resonance

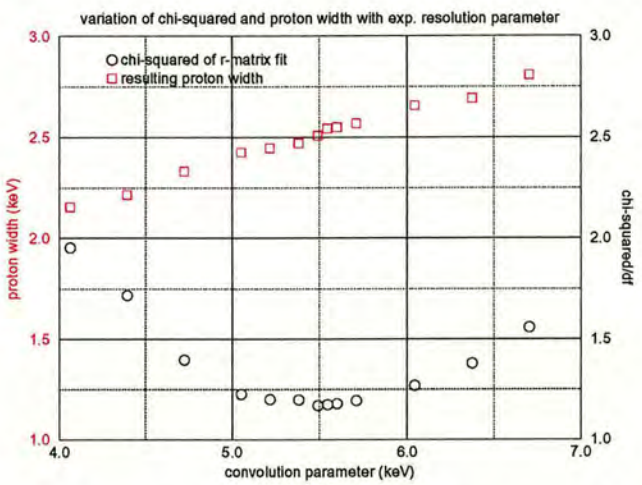

Figure 7.1: *Variation of χ^2_ν and Γ_p with convolution parameter for ^{21}Ne+p 733 keV resonance.*

strengths from, for example, ref. [70]. This generally involves extracting J^π from the resonance strength, $\omega\gamma$, However, the compilations have completely ignored previous work done on ^{21}Ne+p scattering, that of ref. [63]. In that particular experiment, no inelastics were observed, suggesting either a closed inelastic channel or small partial widths for inelastic scattering. The partial γ-width is small also, and to first order, the total width is mostly made up from the elastic partial width. In ref. [70], inelastic scattering was observed for these resonances, but with relatively small yields. This leads to the assumption that the proton partial width is indeed close to the value of the total width, and a single channel formalism is justified in fitting the ^{21}Ne+p resonances in this work.

The spin assignments of ref. [63] were based on fits to elastic resonances in ^{21}Ne+p, taking into account the resonance shape changes over a

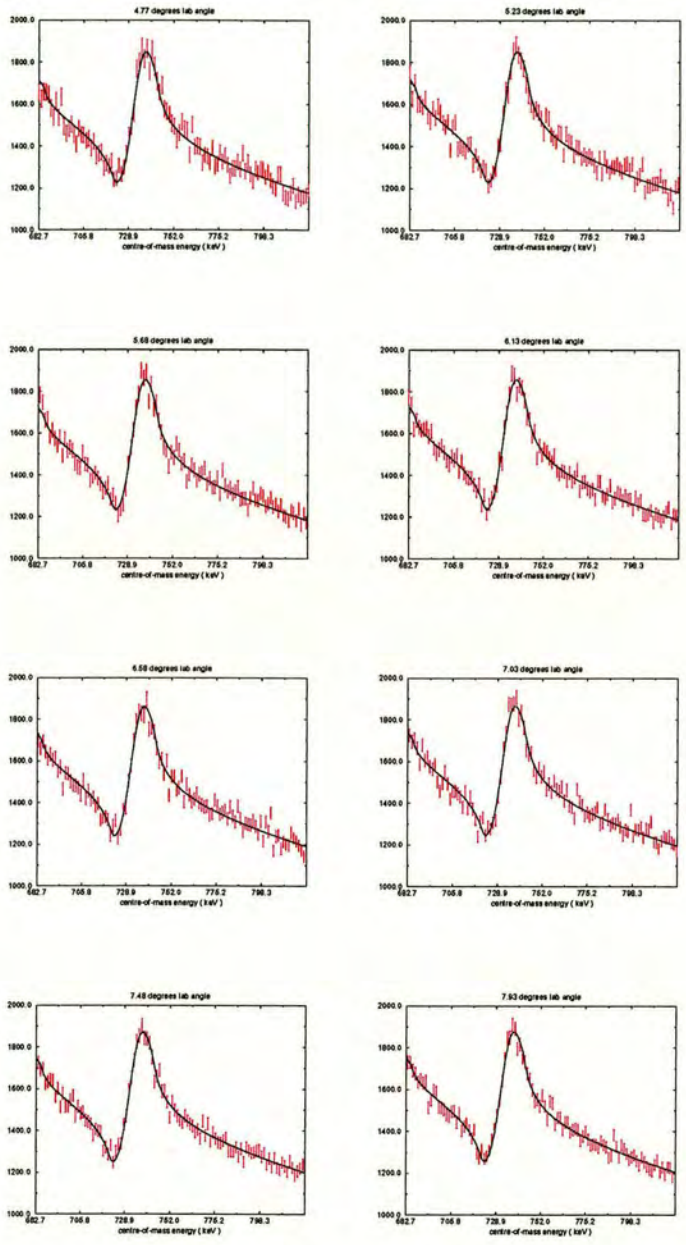

Figure 7.2: *Yield curves for the $^{21}Ne+p$ R-Matrix fits against the experimental data for annuli 0-7.*

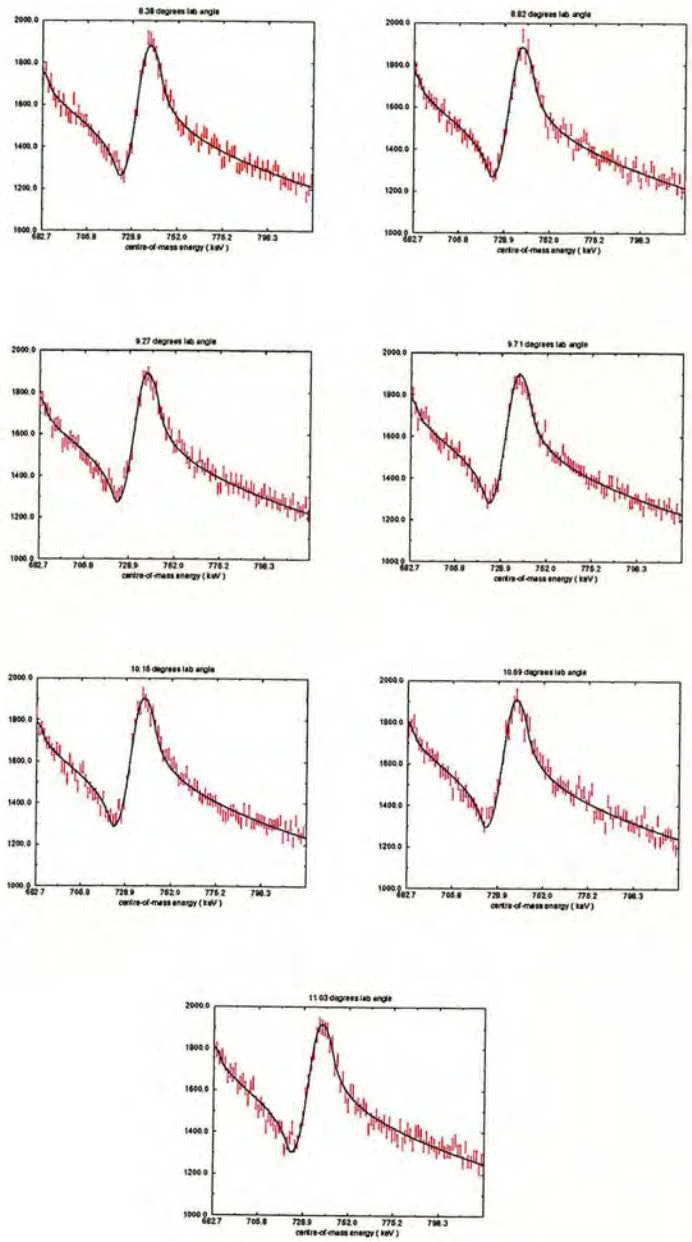

Figure 7.3: *Yield curves for the $^{21}Ne+p$ R-Matrix fits against the experimental data for annuli 8-14.*

wide range of angles. Protons of angular momentum ℓ=0 were seen to populate the states of interest, leading to tighter restrictions on the possibility of the state assignments. In this work, I have chosen to take into account the spin assignments made in that reference, being both $(1,2)^+$, based on the fact that an s-wave proton can only populate states in ^{21}Ne+p of these spin-parity combinations. Since the problem of ^{21}Na+p scattering involved the same spin-parity combination restrictions, it is prudent to refer closely to the resonant properties of the T=1 analogue levels in ^{21}Ne+p scattering.

7.3 Data fitting: ^{21}Na+p

After the corrections had been applied to the elastic and inelastic data, the result was a collection of 32 elastic excitation functions and 16 inelastic excitation functions[1]. Figure 7.4 shows representative elastic and inelastic excitation functions for the forward angle detector. Excitation functions for other angles in the same detector were extremely similar, a result of the slow kinematic variation in the outgoing proton energy. Three strong broad resonances of the order of tens of keV wide are seen in the elastic spectrum, and are hereby referred to as resonances 1, 2 and 3, starting from the lowest energy. In the inelastic excitation function, three peak-like structures are seen. The lowest energy pair of peaks corresponds to the 1170 keV/nucleon thin target run, designed to cover the region corresponding to elastic resonance 2. The small peak on the right hand side of this pair is closely matched in energy with the centre of elastic resonance 2, suggesting

[1]The inelastic data from the backward angle detector was deemed too broadened to be of significant benefit to the analysis.

this peak is an excitation of the same state. The larger peak of the pair is at a lower energy than the centre of elastic resonance 2. It corresponds to inelastic excitation of a state which has weak or nonexistent excitation in the elastic channel. These peaks have been labelled inelastic resonance 2a and 2b to refer to the fact that they are closely associated to elastic resonance 2. The large inelastic peak marked inelastic resonance 3 results from the 1440 keV/nucleon thick target run. Because this resonance is broad, the thin target run at 1420 keV/nucleon did not cover the whole range of the peak. There is however, a background from the elastic spectrum target edge on which this peak sits, making the peak appear stronger.

In order to begin fitting the elastic data, consideration has to be given to the following. 1) Is the use of an s-wave only formalism justified given the physical constraints on the ^{21}Na+p system, and the phenomenology of the data? 2) Is the use of a single-channel formalism justified given the qualities of the inelastic data?

The ^{21}Na+p system has an incident channel spin of s=1,2, given that the ground state spin-parities of ^{21}Na and ^{1}H are $3/2^{+}$ and $1/2^{+}$ respectively. The parity of the incident channel is defined as positive. The allowed spins of the compound nucleus states are then found by vector addition of the incident ℓ-value of the system and the channel spin, with the parities given by $\pi = (-)^{\ell}$. The maximum energy in the centre-of-mass used in this experiment was around 1.5 MeV. Using this value, the maximum probable ℓ-value in any reaction can be estimated with the angular momentum relation $L_z = \ell\hbar = |\vec{r} \times \vec{p}|$, which gives the maximum ℓ-value as

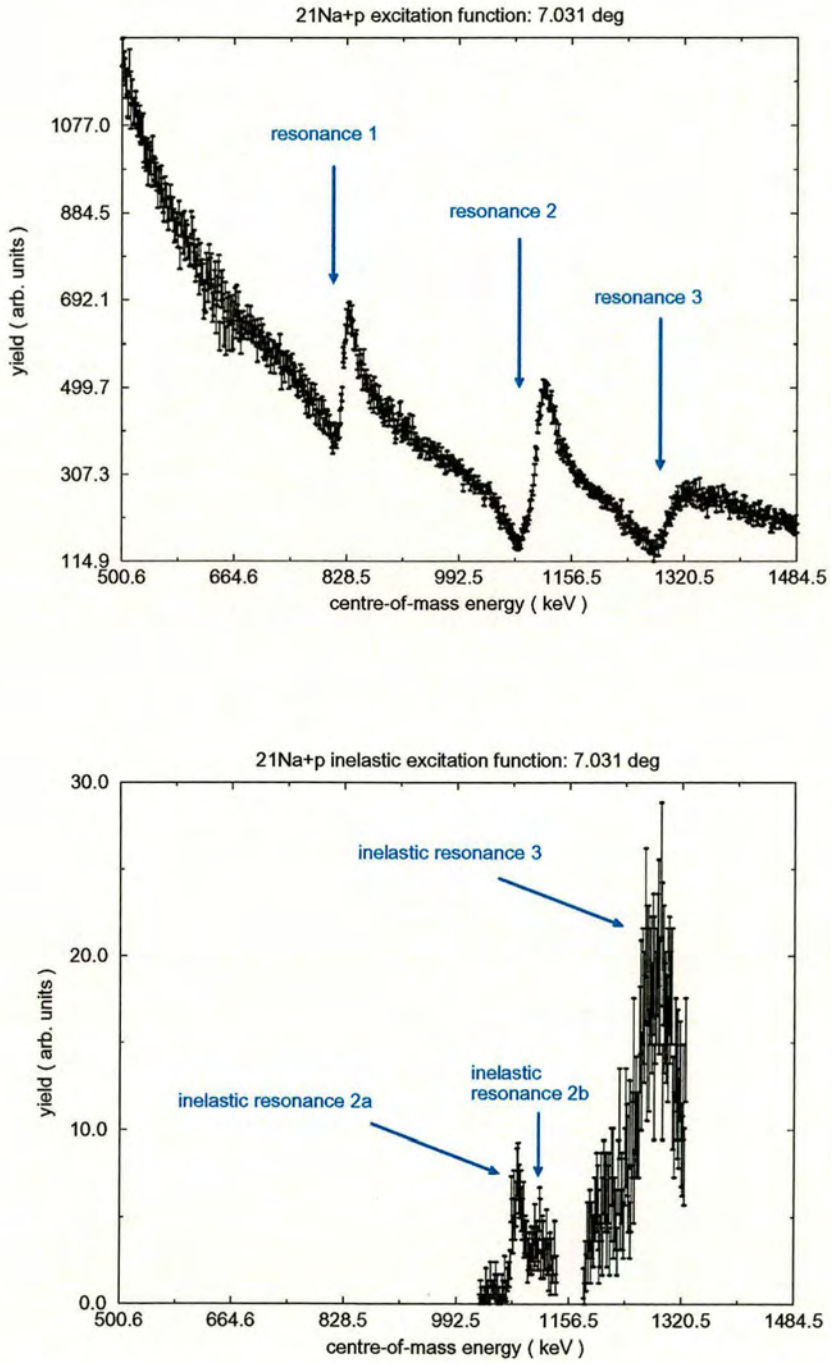

Figure 7.4: *Representative elastic and inelastic excitation functions from the forward angle detector, showing three strong elastic resonances and three inelastic peaks.*

$$\ell \leq \frac{r\sqrt{2\mu E}}{\hbar} \tag{7.3}$$

where μ is the reduced mass and r is the sum of the nuclear radii involved. Using r=4.51 fm, this gives $\ell \leq 1.18$. This is a semi-classical estimate, and suggests that $\ell \leq 1$ at these low energies. To take into account the possible contribution of peripheral reaction beyond the grazing radius, ℓ-values up to $\ell = 2$ are considered. One can also consider the Wigner limit for the width of a single particle state [39], which is the largest width a pure single particle state can have based on penetrability arguments, and is given by:

$$\Gamma_p^W = \frac{3\hbar^2 \mathcal{P}_\ell(E = E_R, a)}{\mu a^2} \tag{7.4}$$

where a is the channel radius, given by $1.2(A_1^{1/3} + A_2^{1/3})$, μ is the reduced mass, and $\mathcal{P}_\ell$ is the penetrability for a given ℓ-value, energy and channel radius. Using this argument for E=1.5 MeV arrives at the following Wigner limits:

ℓ	$\mathcal{P}_\ell$	Γ_p^W (MeV)
0	0.138	0.882
1	4.424×10^{-2}	0.283
2	4.929×10^{-3}	3.151×10^{-2}
3	2.421×10^{-4}	1.548×10^{-3}

Since the states are likely to be more complicated than single-particle

ℓ	s	J^π
0	1	1^+
	2	2^+
1	1	0^-
		1^-
		2^-
	2	1^-
		2^-
		3^-
2	1	1^+
		2^+
		3^+
	2	0^+
		1^+
		2^+
		3^+
		4^+

Table 7.2: *Incident spin and orbital angular momentum combinations for* $^{21}Na+p$.

states, the widths will be some fraction of the Wigner limit. This makes it unlikely to see states corresponding to $\ell = 3$ based on sensitivity and strength arguments, especially at lower energies, where for example at E = 0.825 MeV, the Wigner limit is more like $\Gamma_p^W = 0.03$ keV.

Considering up to $\ell = 2$, this then makes the likely possible spin-parities resulting from combinations of ℓ and s as in table 7.2.

Inelastic scattering to the first excited state of ^{21}Na with E_x=332 keV and $J^\pi = 5/2^+$ can be considered by the allowed outgoing orbital angular momentum and channel spin combinations. Choosing only combinations with ℓ and ℓ' less than or equal to 2 results in the values given in table 7.3.

Thus, for example, a 1^+ state formed via an incident elastic channel at these energies is semi-classically unlikely to decay via an inelastic channel due

ℓ	s	J^π	s′	ℓ'
0	1	1^+	2	2
			3	2
	2	2^+	2	0
			2	2
			3	2
1	1	0^-	X	X
		1^-	2	1
		2^-	2	1
			2	1
	2	1^-	2	1
		2^-	2	1
			3	1
		3^-	2	1
			3	1
2	1	1^+	2	2
			3	2
		2^+	2	0
			2	2
			3	2
		3^+	3	0
			2	2
			3	2
	2	0^+	2	0
			3	0
			2	2
		1^+	2	2
			3	2
		2^+	2	0
			2	2
			3	2
		3^+	3	0
			2	2
			3	2
		4^+	2	2

Table 7.3: *Possible exit-channel spin and orbital angular momentum combinations for $^{21}Na+p$ inelastic scattering to the first excited state.*

to the requirement of a large outgoing orbital angular momentum, whereas a 2^+ state formed via the same mechanism can decay via the inelastic channel with $\ell' = 0$. This assumption becomes important in the consideration of spin-parity assignments to be included in any fit.

Armed with this information, s-wave single-channel fits were investigated for the elastic excitation functions over a range of angles. A single-channel, spin-zero formalism fit was investigated at an earlier stage in this analysis [78], finding preliminary estimates of resonance energies and widths which are highly formalism-dependent. In the spin-zero approximation, the effective spin statistical factor used is equal to 1. This incorrectly represents the relative intensity of neighbouring resonances of different J^π, leading to estimates of resonance widths and energies which are likely to be substantially different than the actual properties of the states. Thus we have included the effects of spin-dependence in this formalism, leading to a more correct and physical interpretation of the data.

Fits were investigated using the resolution parameters derived previously. It was found that the data required the spin-parity assignments of resonance 1, $J^\pi = 1^+$ and resonance 2, $J^\pi = 2^+$ to ensure a good fit, other combinations of J^π unsatisfactorily reproducing the data. This assignment is strengthened by the inelastic constraints mentioned above, combined with the fact that no inelastic resonances were seen in the region of resonance 1, while resonance 2 clearly does have resonant inelastic structure associated with it.

An s-wave investigation of resonance 3 concluded that it was difficult to reproduce the shape of this resonance with either $J^\pi = 1^+$ or 2^+ assigned to the state in the fit. The main problem arises from the inability to generate

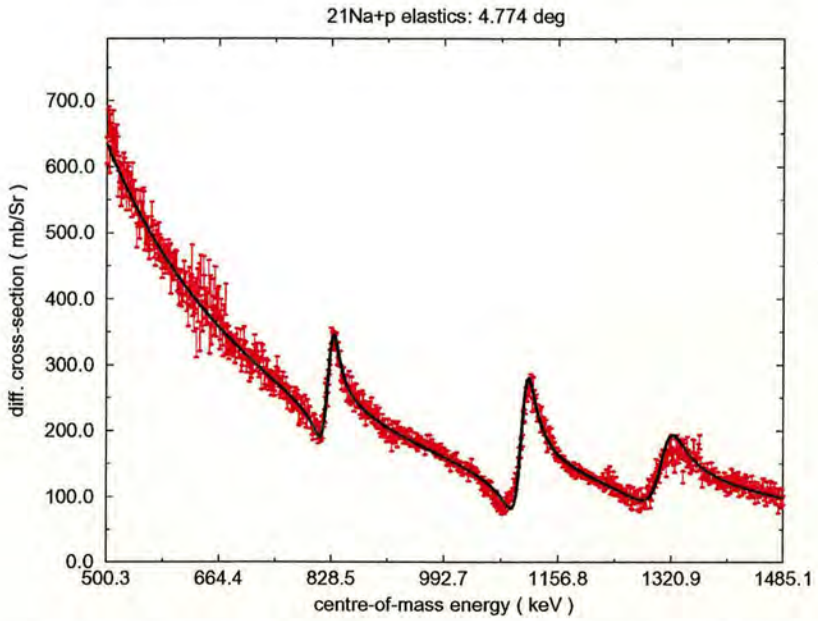

Figure 7.5: *Single-channel s-wave R-Matrix fit to 4.774° data using experimental resolution parameters derived from target edges.*

both the width and the amplitude, with any reasonable combination of width or the known possibilities of experimental resolution. This lends to the theories that this resonance may either proceed via a higher order ℓ than the others, or proceed via an s-wave and have its elastic amplitude severely damped by the broad strong inelastic contribution.

Figure 7.5 shows a single angle R-Matrix fit of the 4.774° data with three s-waves. Resonances 1 and 2 were fitted with $J^{\pi} = 1^{+}$ states, and resonance 2 with a $J^{\pi} = 2^{+}$ state. The experimental resolution parameters used were those listed in table 6.3. The fit was made with the boundary energy set to 0.825 MeV, and the global chi-squared per data point was $\chi^2_{\nu} =$

1.477. A large contribution to this was the fit in the regions of resonances 2 and 3. The chi-squared per data point over the region of resonance 1 was $\chi^2_\nu = 0.900$. This indicates that the fit for resonance 1 is satisfactory, but problems arise in the fits for the other two resonances.

Figure 7.6 shows a close-up of each resonance for the attempted s-wave only fit. Resonance 1 has been reproduced well in shape by the fit, and is therefore justifiably described by the s-wave fit according to the constraints detailed in the previous section.

Resonance 2 has not been so well reproduced by the fit. Here, the R-Matrix curve is narrower in extent compared to the data. However, at the minimum of the data there seems to be a shape structure which suggests possible interference from another resonance. This would be consistent with the inelastic data which suggests a dual resonance structure in this energy region. Since the inelastic strengths are non-zero for these resonances, it is concluded that a single-channel s-wave only fit cannot be used to extract the width of the resonances in this region.

Resonance 3 bears a resemblance to an s-wave in some respects, but is not reproduced extremely well by the fit. The large strength of the inelastic channel for this resonance suggests the need for a multi-channel fit as with resonance 2. Also, in this fit, an extra normalisation adjustment was introduced in order to facilitate the attempted s-wave fit. However, the adjustment seems to introduce a small mismatch in the data between the 1340 keV/u and 1440 keV/u runs, giving the illusion of a small peak at around 1220 keV. When the single-channel fit is attempted without the adjustment, the minimum of the resonance cannot be reproduced. Therefore, in all subsequent fits, the data was left unadjusted pending a multi-channel

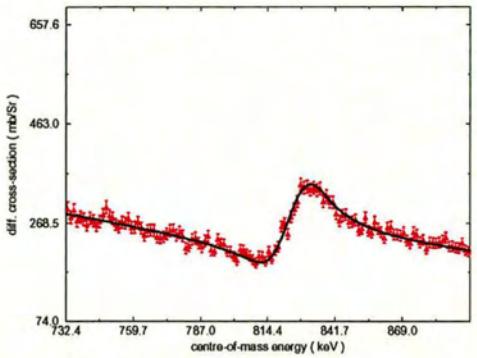

(a) Resonance 1

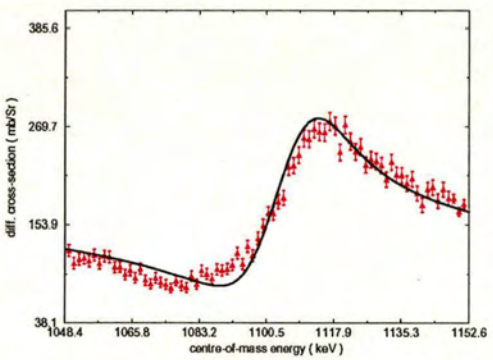

(b) Resonance 2

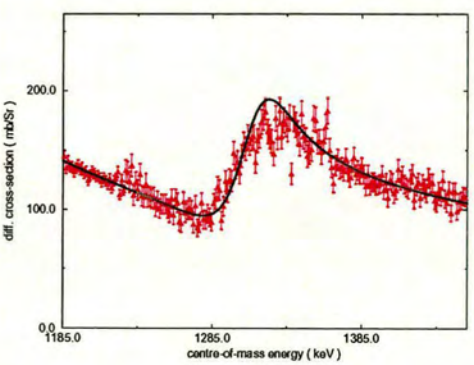

(c) Resonance 3

Figure 7.6: *Close-up of best-fit R-Matrix curve for the three separate resonances for an attempted s-wave only fit .*

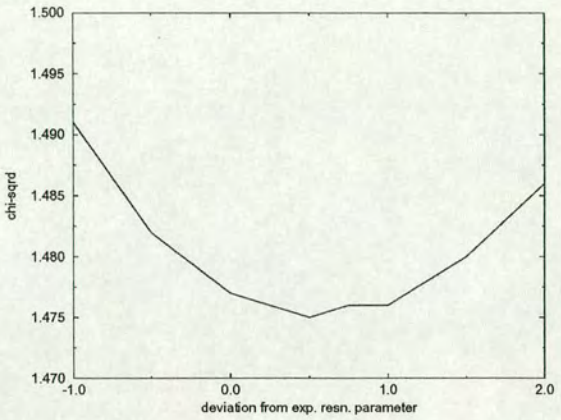

Figure 7.7: *Variation of chi-squared with the experimental resolution parameter for resonance 1 with a channel radius of 5.3 fm .*

treatment.

7.3.1 Width and energy extraction of elastic resonance 1

In order to extract the best-fit proton width and resonance energy from resonance 1, the variation of the chi-squared was investigated around the region of the derived experimental resolution parameter using data from twelve angles. This was achieved by fixing the parameters of resonance 2 and 3, and allowing the parameters of resonance 1 to vary, for different values of the experimental resolution at the target sections in the region of the resonance. The radius was also set at several particular values in order to find the value of channel radius for which the data is best represented.

Figure 7.7 shows the variation of the global chi-squared per data point

with the experimental resolution in the region of resonance 1 when the channel radius is set to $a_c = 5.3$ fm, which corresponds to $1.4(A_1^{1/3} + A_2^{1/3})$, as suggested in ref. [11]. The units on the x-axis are in terms of multiples of the error in the experimental resolution parameter. It can be seen that there is a definite minimum close to $\sigma = \sigma_{exp} + (1/5 \times \Delta\sigma)$ where $\Delta\sigma$ is the error on the experimental resolution parameter, σ_{exp}.

The multi-angle χ^2 behaviour for different values of the channel radius around the value $a_c = 5.3$ fm was investigated by fixing the experimental resolution and the radius over resonance 1 and performing a fit. This was made for several values of a_c from 4.0 fm to 7.0 fm, and several values of the experimental resolution. The average χ^2_ν is calculated over the region of resonance 1, and this information is then used to interpolate values on a χ^2_ν surface over the resolution-radius space. The minimum χ^2_ν was found to be between the values $5.1 \leq a_c \leq 5.5$ fm and for $\sigma = \sigma_{exp} + (1/5 \times \Delta\sigma)$.

Figure 7.8 shows the 3-dimensional interpolated χ^2 surface over the region of resolution and radius values considered. The shallow minimum around $a_c = 5.3$ fm can be seen as the blue area. The best-fit resonance 1 internal parameters for this fit were:

Channel Radius	a_c	5.3 fm
Boundary Energy	E_b	0.825 MeV
Pole Energy	E_1	0.82449 ± 0.00008 MeV
Reduced Width	γ_1	0.68411 ± 0.00278 MeV$^{1/2}$
Reduced Width On-Resonance	γ_1^0	0.68385 ± 0.00278 MeV$^{1/2}$

The above values result in a partial proton width of $\Gamma_p = 13.6 \pm 1.4$ keV. The errors here have taken into account the variation in this value due

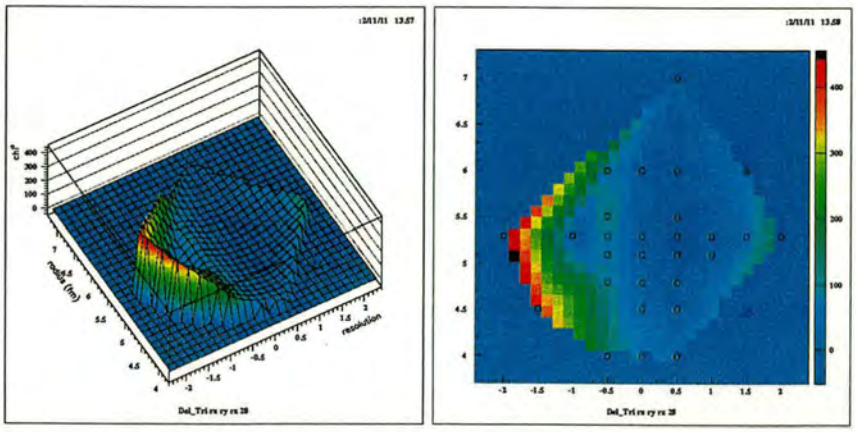

(a) surface plot

(b) 2-dimensional plot showing points used in interpolation

Figure 7.8: *3-dimensional χ^2 distribution of twelve angle fit in radius-resolution space.*

to the uncertainty in the resolution parameter, the radius value, and also the errors introduced by fitting over twelve angles due to differences in the data. The resonance energy resulting from the boundary transformation is $E_R = 824.6 \pm 1.5$ keV, where the error takes into account both the fit uncertainties and the calibration error.

The results of these fits can be seen in figures 7.9 and 7.10. The normalisation constant used in the fitting program to shift the R-Matrix cross-sections in units of millibarns/steradian into the arbitrary yield units was found to be 1.8727. Figure 7.11 shows the excitation function for $\theta_{lab} = 4.774°$ in units of mb/Sr.

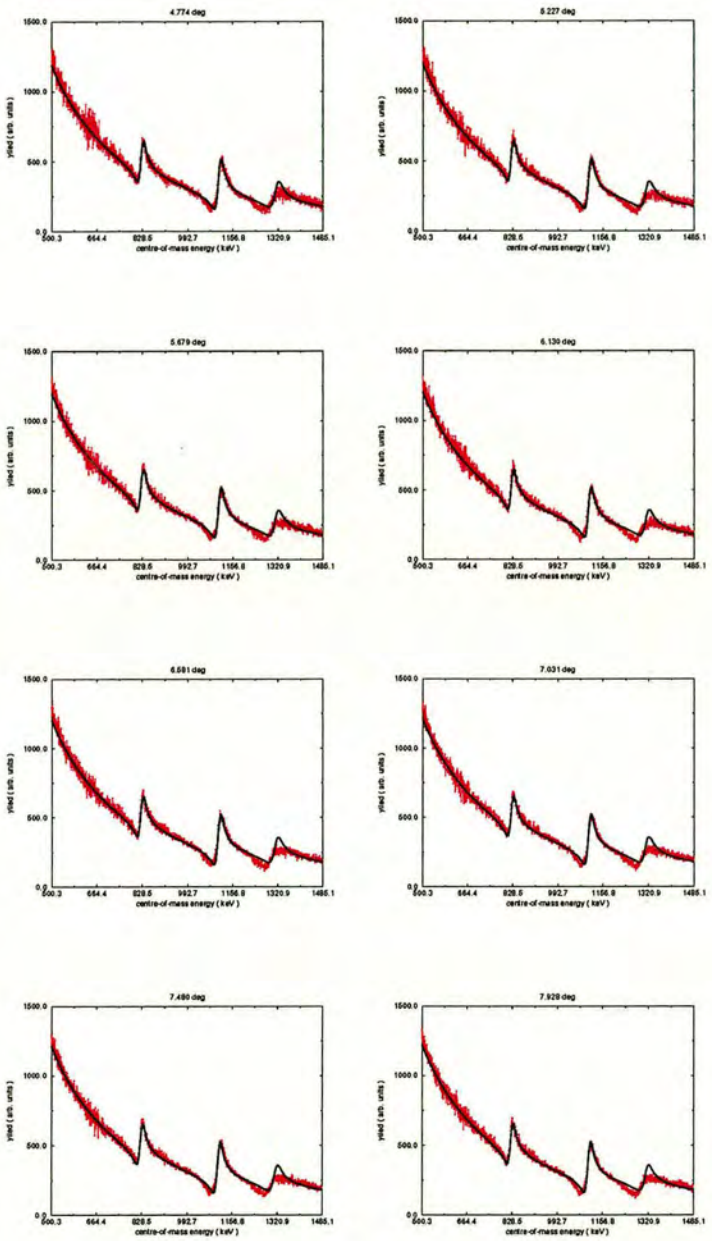

Figure 7.9: *Yield curves for the $^{21}Na+p$ R-Matrix fits against the experimental data for annuli 0-7.*

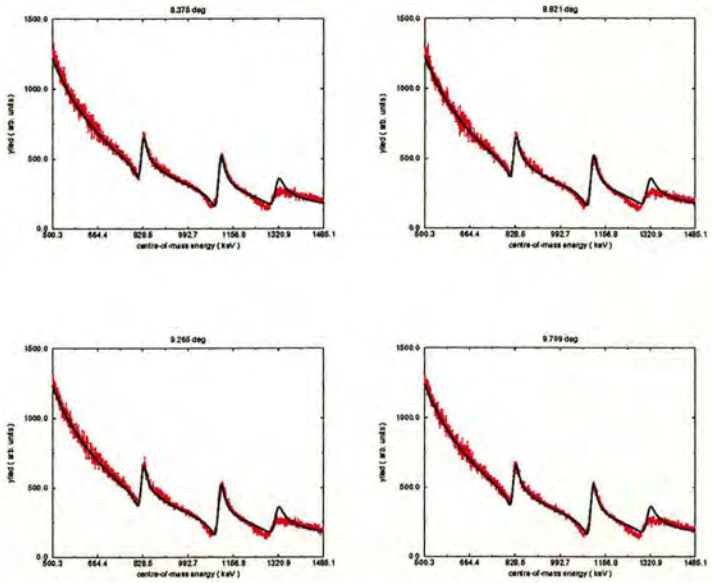

Figure 7.10: *Yield curves for the $^{21}Na+p$ R-Matrix fits against the experimental data for annuli 8-11.*

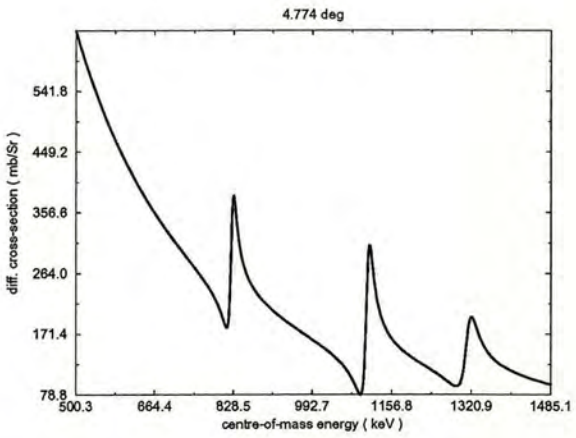

Figure 7.11: *R-Matrix excitation function for 4.774° in units of mb/Sr.*

7.3.2 Estimation of resonance parameters using inelastic peaks

The inelastic excitation function was summed over all 16 angles of the forward detector, and was used to estimate the resonance energies of the peaks contained therein. The two lower energy peaks were treated as a doublet and so were fitted simultaneously as the sum of two Lorentzians. Figure 7.3.2 (a) shows the best fit superimposed on the data. The free parameters were the centroid energy, the width, and the strength of each Lorentzian peak. The fit resulted in the centroid energies of 1079 ± 8 keV and 1107 ± 11 keV respectively. The errors are linear combinations of the fit errors, the spectrum shift error due to the ^{21}Ne+p calibration, the differential calibration error and the errors induced by transformation between incident centre-of-mass energy, detected lab energy and inelastic centre-of-mass energy frames.

The same fit procedure for the higher energy inelastic resonance resulted in a resonance energy of 1279 ± 9 keV. Note that some points were omitted from the fit as can be seen in figure 7.3.2 (b), due to the uncertain nature of the spectrum background contributions around the resonance.

The Lorentzian widths used in the fits for these inelastic resonances can be used as an estimation of the total width of the resonances. Using these values, and correcting for the convolution effects, we arrive at the following values for the total width:

Resonance energy (keV)	estimated width (keV)
1079 ± 8	9 ± 3
1107 ± 11	49 ± 12
1279 ± 9	61 ± 11

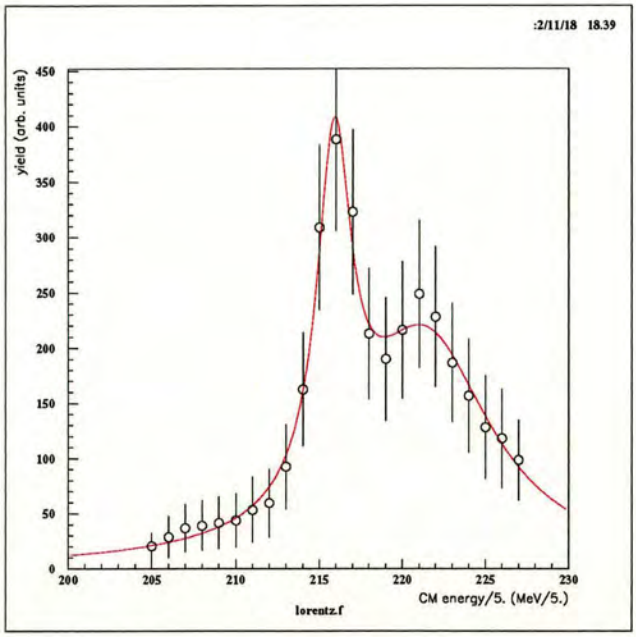

(a) Rebinned summed inelastic data from 1170 keV/nucleon thin target run, fitted with a double Lorentzian structure to extract centroid energies.

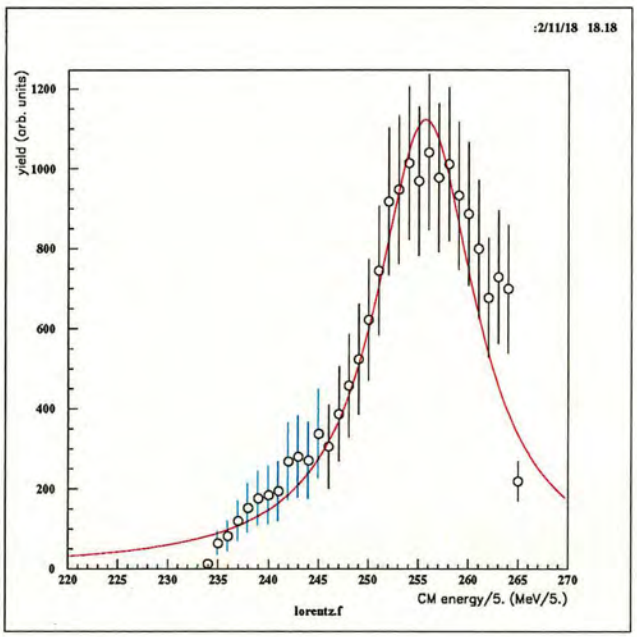

(b) Rebinned summed inelastic data from 1440 keV/nucleon thick target run, fitted with a single Lorentzian structure to extract centroid energy.

Figure 7.12: *Summed rebinned inelastic proton spectra.*

Resonance Energy (keV)	Excitation Energy (keV)	Total Width (keV)	(p,p)	(p,p′)	J^π
824.6 ± 1.5	6326.6 ± 3.0	13.6 ± 1.4	X		1^+
1079 ± 8	6581 ± 10	9 ± 3		X	
1107 ± 11	6609 ± 13	49 ± 12	X	X	
1279 ± 9	6781 ± 11	61 ± 11	X	X	

Table 7.4: *^{21}Na+p resonance properties. An* **X** *denotes that the resonance was observed in the specific channel listed in the column.*

The errors are large in the estimated resonance widths, and would be expected to be reduced during a multi-channel R-Matrix fit. In such a fit, the elastic and inelastic data would constrain the parameter set of each other, leading to tighter restrictions on the fitted parameter values. It also allows scope for corrections to the spectra such as allowing the inelastic data set to shift in energy and magnitude to determine if the fit relative to the elastic resonances is improved by this.

7.4 Discussion of ^{22}Mg nuclear structure and the T=1 analogue system

In total, four resonances in the ^{21}Na+p system were discovered in the energy region covered by this experiment. The values of the widths and/or resonance energies of these are summarised in table 7.4.

7.4.1 825 keV resonance

The 825 keV resonance was found to have a satisfactory fit with a single-channel s-wave formalism. The spin-parity possibilities were $J^\pi = 1^+, 2^+,$

but the best fit was found for $J^{\pi} = 1^{+}$. This makes the state unnatural parity. This state is identified as the $E_x = 6323$ keV state as seen in refs. [47] and [48] and unresolved in other experiments. In the (p,t) reaction of ref. [47], the assumption was made that only states of natural parity would likely be formed in ^{22}Mg. This assumption is based on the premise that if states are populated with similar intensities to known natural parity transitions, then they are likely to have been formed by the two nucleons being in a relative s-wave state during transfer and have the outgoing triton spin oriented in the same direction as the final ^{22}Mg spin , ie. the proton serves as a "spectator". However, it is also possible that unnatural parity states can be populated via a spin-flip mechanism. If the particle width of the compound state is large, then the reaction will proceed with high probability, regardless of the parity change. A DWBA fit to an angular distribution of the reaction would likely yield the parity assignment of the state if a unique angular momentum transfer could be seen. Therefore, the natural parity assignments of ref. [47] can only be regarded as "weak" arguments, given that no detailed angular distribution was fitted.

In the ^{12}C(^{16}O,^{6}He)^{22}Mg reaction of ref. [50], it is also assumed that only states of natural parity would tend to be selected by the reaction process, which is thought to be a compound nucleus process. Here however, the selection is perhaps more strongly apparent than in the (p,t) reaction, since the ^{22}Mg spin-parities are determined by the breakup ℓ-value primarily, the compound nucleus states being formed with natural parity. Indeed, this reaction failed to see the state in question yet saw other nearby natural parity states of similar strength, suggesting either that the experimental spin-selectivity is indeed active and the state is unnatural parity, or that

the resolution in the experiment was insufficient to resolve this state from the nearby $E_x = 6248$ keV state. The assignment of $J^\pi = 1^+$ to this state therefore does not contradict previous experimental data.

One aspect of this assignment to be considered is the placement of this state within the isospin T=1 triplet analogue system of ^{22}Ne, ^{22}Na and ^{22}Mg. Figure 7.13 shows the known T=1 states in the analogue system. Where spin-parities are known, they have been indicated on the diagram. The four resonances measured in this experiment are also marked on the diagram, the 6327 keV state marked with the 1^+ assignment. The analogue of this state in the ^{22}Ne system must also be a 1^+ state. The nearest 1^+ state is the $E_x = 6854$ keV state in ^{22}Ne. If this is indeed the analogue of the 6327 keV state, the Thomas-Ehrmann shift between the states is fairly large (527 keV). However, the assignment of the ^{22}Ne $E_x = 6120$ keV and ^{22}Mg $E_x = 5714$ keV 2^+ states as analogues provides a Thomas-Ehrmann shift of 406 keV in the same system, which is not far removed from the value of 527 keV. Of course, the shift depends on the various nuclear properties of the state, and so we can estimate the order of magnitude shift caused by a pair of states for different values of the *dimensionless width*.

The dimensionless particle width, θ_p, of a state is a measure of how wide a state is compared to the maximum possible value in single-particle terms, given by the Wigner limit. Using this time, a value of $a = 5.3$ fm for the radius, as determined by the R-Matrix fits, we arrive at an $\ell = 0$ Wigner limit value of around $\Gamma_p^W \approx 90$ keV for the 825 keV resonance. The dimensionless width is the square root of the ratio of the true width to the

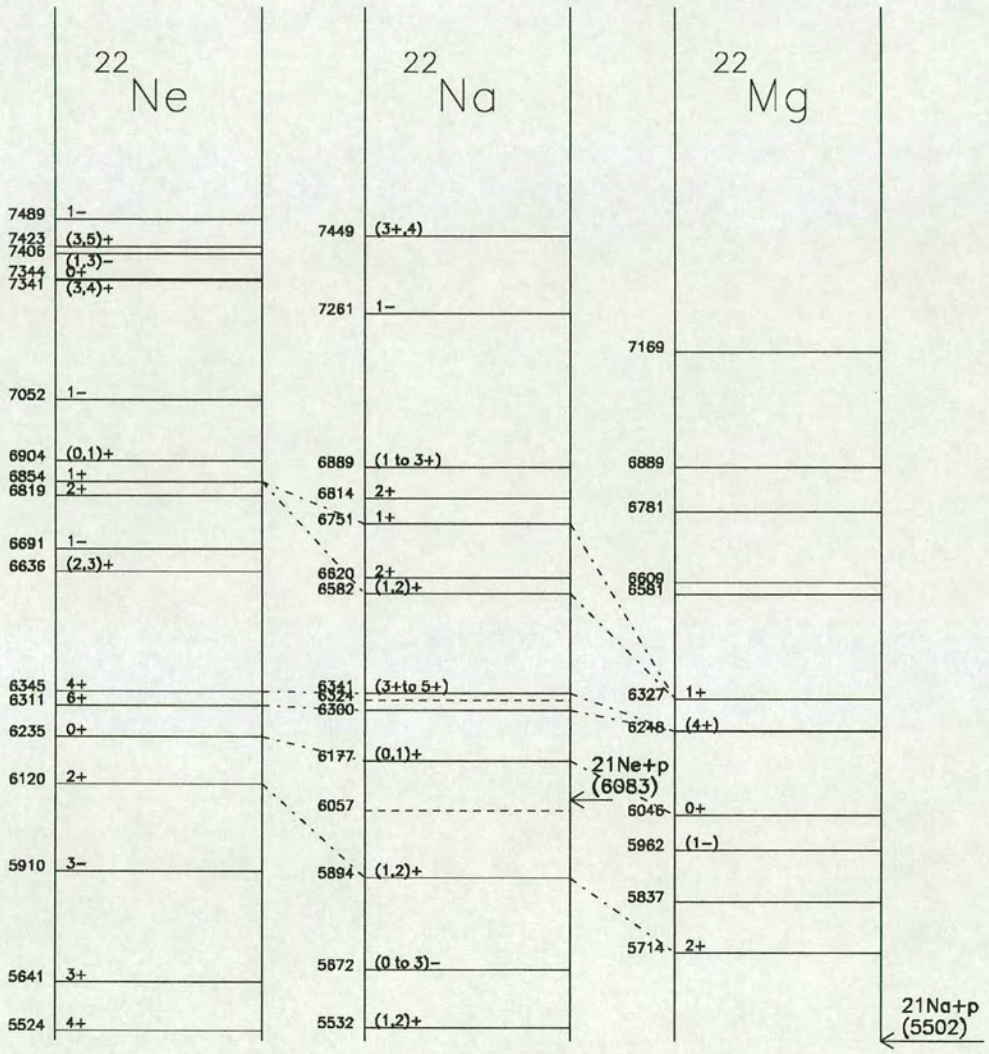

Figure 7.13: *The T=1 isospin triplet analogue system of ^{22}Ne, ^{22}Na and ^{22}Mg. Spin-parities have been marked where known. Dashed energy level lines in ^{22}Na indicate states which have ambiguous T=1 assignments. The dash-dotted lines show suggested possible analogue assigments.*

Wigner limit[2], and in this case gives

$$\theta_p = \sqrt{\frac{\Gamma_p}{\Gamma_p^W}} \approx 0.4 \tag{7.5}$$

for this resonance. In order to estimate the level shifts, we consider the energy shift of the $E_x = 6854$ keV bound state in ^{22}Ne, which is given by (ref. [79])

$$\Delta_b = -\frac{3}{2}\frac{\hbar^2}{\mu a^2}\theta_b^2 \rho \frac{W_\ell'}{W_\ell} \tag{7.6}$$

where W_ℓ and W_ℓ' are the Whittaker function and its derivative, respectively. The level shift in ^{22}Mg, of the analogue state with resonance energy E_R, is given by

$$\Delta_R = -\frac{3}{2}\frac{\hbar^2}{\mu a^2}\theta_R^2 S_\ell \tag{7.7}$$

where S_ℓ is the shift function. We assume that $\theta_b = \theta_R$. We can then iterate values of θ until the equality $E_b - E_R = \Delta_b - \Delta_R$ is satisfied, where E_b is the neutron separation energy of ^{22}Ne minus the state energy. In this way, we find that with a value of $\theta \approx 0.5$, we can produce a shift of sufficient size to place the resonance energy of the ^{22}Mg state at 0.825 MeV. This would correspond to a proton width of about 25 keV. This is a simplified

[2]The dimensionless width can also be given in terms of the reduced width, and shift derivative by $\theta_p = \sqrt{2\mathcal{P}\gamma_p^2/\Gamma_p^W(1 + S'\gamma^2)}$.

picture, since the nuclear properties of the analogue states are never likely to be the same, and various admixture properties in each state can alter the shift. However, this result seems to show that the level shift observed is not unusual in any way, instead is compatible with the simple Wigner limit and Thomas-Ehrmann shift restrictions.

The ^{22}Mg state energy implied by the resonance, $E_x = 6326.6 \pm 3.0$ keV, agrees well with previously measured values. The most accurate measurements were those of refs. [47] and [48], with values of 6322.6 ± 6.0 keV and 6329 ± 6 keV respectively, which places our value in the overlapping region of the error bars of each of these measurements, leading to a new adopted value of 6326.0 ± 2.6 keV.

7.4.2 1079 keV and 1107 keV resonances

The 1079 keV resonance ($E_x = 6581$ keV) has not been previously observed in any experiment. Here, it was seen strongly in the inelastic channel, while there was slight evidence for it in the elastic channel in the form of a shape distortion near the low energy minimum of the second elastic resonance. Although at this point, without a multi-channel fit, we are unable to make a spin-parity assignment, restrictions can be put on the possible qualities. The state must have a spin-parity which encourages greater probability of the inelastic exit channel than the elastic exit channel. This could occur for various situations where the outgoing orbital angular momentum is low, cf. table 7.3. For example, positive parity states could be formed via $\ell = 0, 2$ in the entrance channel, then proceed via $\ell' = 0, 2$ in the inelastic exit channel. However, if the leading partial wave was an s-wave, then the resonance

would be larger in the elastic channel in terms of shape, given the width of this resonance as deduced from the inelastic data. Negative parity states could be formed with $\ell = 1$ in both the entrance and exit channels, with the subsequent elastic shape being weaker than the equivalent width s-wave. Certainly there are candidates for both analogue positive and negative parity states in ^{22}Ne, notably the $(2,3)^+$ at 6636 keV, the 1^- at 6691 keV, and the 2^+ at 6819 keV. The total width of this state was estimated as 9 ± 3 keV, however, without a multi-channel fit, we cannot yet say anything about the partial elastic and inelastic strengths.

The 1107 keV resonance ($E_x = 6609$ keV) is identified as the $E_x = 6608.5$ keV (adopted value) state observed in several previous measurements. The shape of this resonance resembles an s-wave, and indeed its strength is similar to that of the 825 keV resonance. The spin restrictions on this state would then be $J^\pi = 1^+, 2^+$, although the attempted elastic fit seemed to suggest a 2^+ state. However, without confirmation from a multi-channel fit, no assignment will be made here. The total width of this state as suggested by the inelastic peak fit is around 49 ± 12 keV. During attempted elastic fits, the suggested proton width was of the order of 20 keV, making it likely that the inelastic width and elastic width are of similar strength. The state energy implied by this resonance is 6609 ± 13 keV. The previous adopted value was 6608.5 ± 5.6 keV, which is in very good agreement.

7.4.3 1279 keV resonance

The 1279 keV resonance ($E_x = 6781$ keV) is identified as the $E_x = 6780.4$ keV (adopted value) state measured in six previous experiments. The large

implied total width of around 61 keV is reflected in both a large elastic resonance shape and a large peak in the inelastic channel. The unsatisfactory fit of this resonance with a single-channel s-wave makes it impossible to assign a spin or partial widths to the state, provoking the need for a multi-channel analysis similar to the other resonances. The fact that this resonance could proceed via an odd or even leading ℓ-value means that the state could be either natural or unnatural parity.

7.5 Astrophysical implications for the ^{21}Na(p,γ)^{22}Mg reaction

It has been reported in earlier work [80] [81] [39] that only the first three levels above the proton threshold in ^{22}Mg are significant for the ^{21}Na(p,γ)^{22}Mg rate in novae. However, at higher temperatures, for example in X-ray binary systems, the states at higher energies will become more important. A large uncertainty in the current reaction rate arises from the unknown strength of the resonance associated with the $E_x = 6045.6$ keV state [47]. Using the upper limit of $\omega\gamma \leq 3.7 \times 10^{-1}$ eV for this resonance, and the resonance strengths tabulated in ref. [47], Table X., we can calculate the resonant contributions to the ^{21}Na(p,γ)^{22}Mg reaction. Calculations were made including the first two states above threshold, the first four states above threshold, and the first eight states above threshold (including the four states seen in this experiment). The resonance strengths used for the four upper states were the maximum values suggested by the total widths of the states, and $\Gamma_\gamma = 0.4$ eV was chosen for all these states, given that recent unpublished

experimental evidence from DRAGON [67] suggests a γ-width of around this value for the 825 keV resonance[3].

The widths of the four upper resonances have total widths which are less than 10% of their resonance energy. According to this, the authors of ref. [2] prescribe the treatment of these as *narrow* resonances. In this way, the widths are not treated as energy-dependent quantities but as fixed at their resonance energy value, and the reaction rate can be expressed as the sum of individual resonances using the complete[4] form of equation 2.11:

$$< \sigma \upsilon >= \left(\frac{2\pi}{\mu kT}\right)^{3/2} \hbar^2 \sum_i (\omega\gamma)_i \exp\left(-\frac{E_i}{kT}\right) \tag{7.8}$$

The resulting total resonant reaction rate can be seen in figure 7.14 for the contribution of two, four and eight states. The parameters of the states were set as, including those used in the calculation:

[3]The γ-width of the 1^+, $E_x = 6854$ keV state in ^{22}Ne is known to be $\Gamma_\gamma = 1.7$ eV [82].
[4]The electron screening factor f has been ignored in this work.

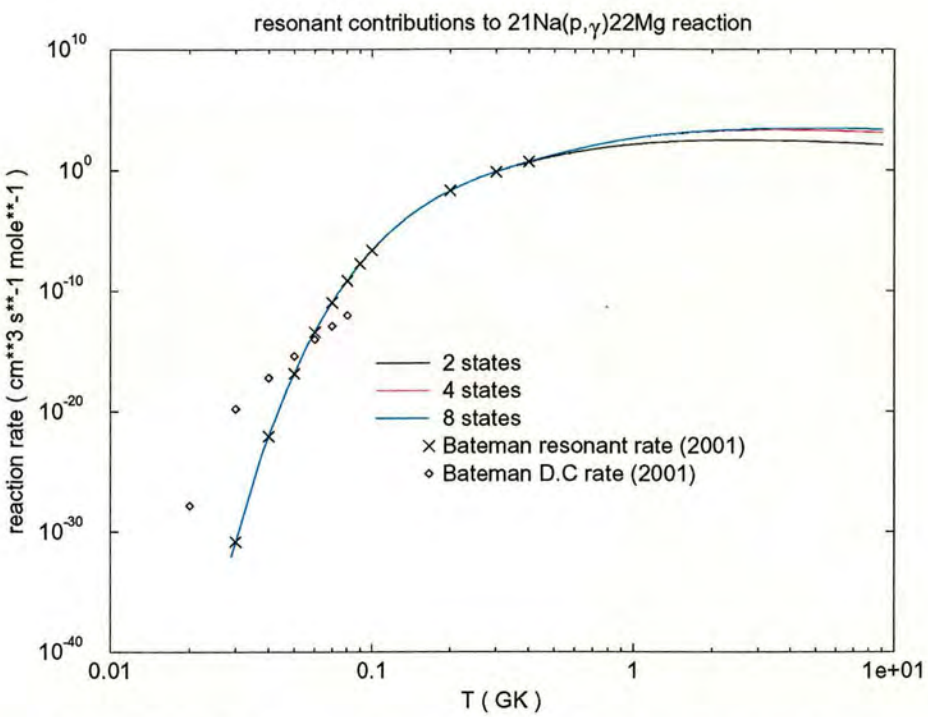

Figure 7.14: *$^{21}Na(p,\gamma)^{22}Mg$ reaction rate including contributions from different sets of resonances. The solid lines are the sum of the resonant contributions. The data are direct and resonant rates tabulated in ref. [47].*

E_R (keV)	E_x (keV)	J^π	Γ_p (eV)	Γ_γ (eV)	$\omega\gamma$ (eV)
212.4	5713.9	2^+	4.6×10^{-3}	2.2×10^{-2}	2.4×10^{-3}
335.5	5837	3^+	4.7×10^{-2}	$\geq 6.6 \times 10^{-2}$	3.2×10^{-2}
460.4	5961.9		$\leq 1.6 \times 10^{2}$	≈ 1	$\leq 3.7 \times 10^{-1}$
544.1	6045.6	0^+	8.8×10^{-1}	1.6×10^{-3}	2.0×10^{-4}
824.6	6326.1	1^+	1.36×10^{4}	0.4	0.15
1079	6581	1	0.9×10^{4}	0.4	0.15
1107	6609	2	0.49×10^{5}	0.4	0.25
1279	6781	2	0.61×10^{5}	0.4	0.25

Also shown in figure 7.14 are the direct capture reaction rate and resonant rate for the four lower states up to 0.4 GK given in ref. [47]. Above around 0.4 GK the rate is uncertain due to the unknown strength of the 460.4 keV resonance. A close up of the high temperature region (fig. 7.15) between 0.1 GK and 10 GK shows the different behaviour of the reaction rates. Up to 0.4 GK, the rates including two, four and eight states agree, ie. the reaction rate is dominated by the lower two resonances and adding higher ones does not make much difference. However, we see that if we add the 460.4 keV resonance (and the 544.1 keV resonance) using its maximum possible value, the rate differs significantly above 0.4 GK. This is the main reason why the strength of the 460.4 keV resonance is much sought after. Adding the four upper resonances makes no significant difference until above 1 GK, when the role of the 824.6 keV resonance becomes important.

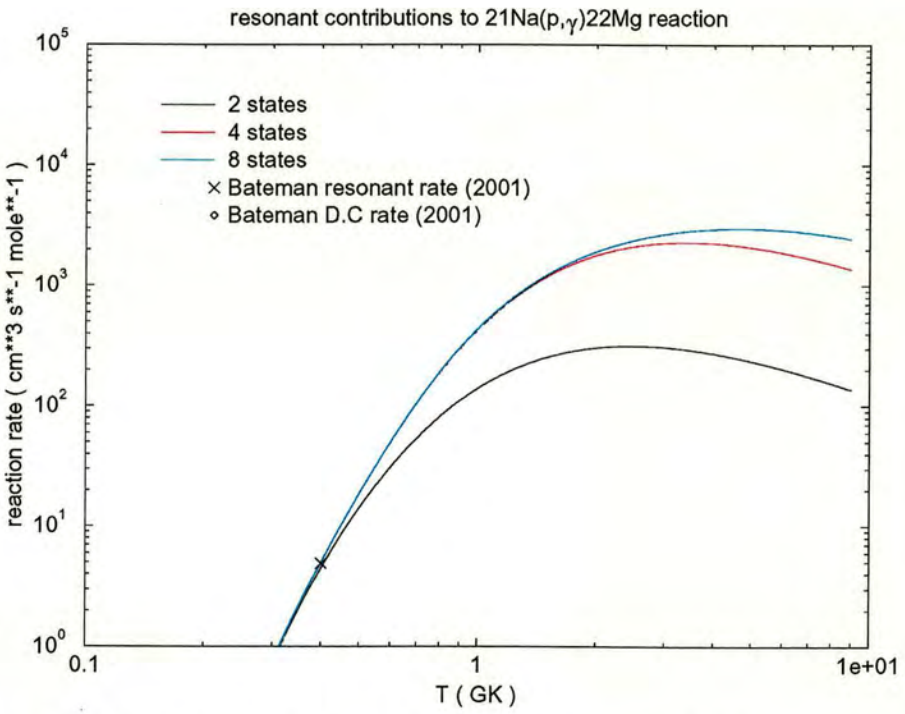

Figure 7.15: *Close up of figure 7.14 in high temperature region.*

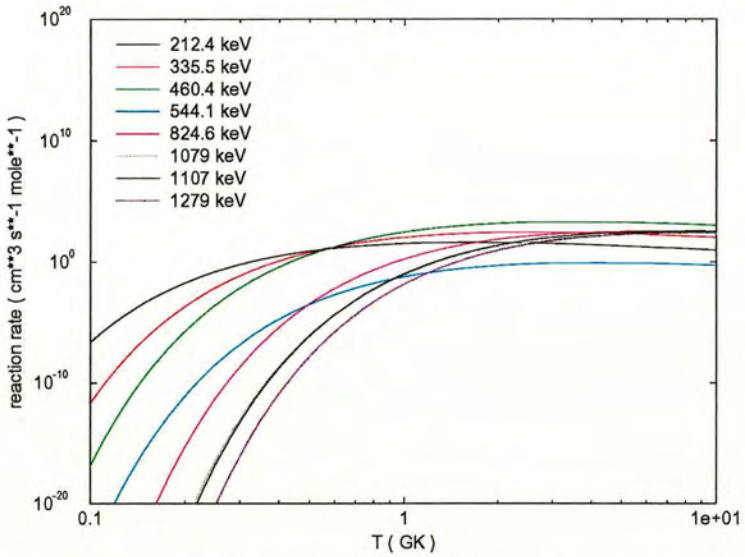

Figure 7.16: *Individual resonance contributions in high temperature region.*

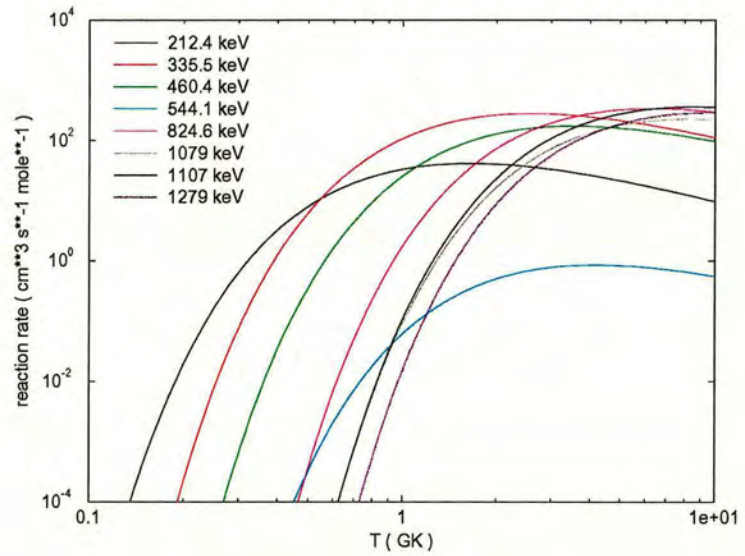

Figure 7.17: *Individual resonance contributions in high temperature region, with* $(\omega\gamma)_3$ *set to* 3.2×10^{-2} *eV.*

We can see the behaviour of individual resonances in the high temperature region by looking at the rate of each individual resonance contribution separately. Figure 7.16 shows the behaviour of the eight resonances between 0.1 GK and 10 GK. It is clear to see that while the 460.4 keV resonance takes on its maximum strength, no other resonance becomes more important in this temperature region. However, it is unlikely that the 460.4 keV resonance will have such a strength. Instead, we can consider the effect on the reaction rate if the 460.4 keV resonance has a similar strength to the 335.5 keV resonance. Setting the strength to 3.2×10^{-2} eV, the rate picture looks very different (fig. 7.17). Here, the influence of the 460.4 keV resonance never becomes stronger than the 335.5 keV resonance, and so the resonances which dominate the reaction in their respective approximate temperature regimes would be:

$$\begin{aligned} &212.4 \text{ keV} \quad 0 < T_9 \leq 0.5 \\ &335.5 \text{ keV} \quad 0.5 < T_9 \leq 3.7 \\ &824.6 \text{ keV} \quad 3.7 < T_9 \leq 6.4 \\ &1107 \text{ keV} \quad 6.4 < T_9 \end{aligned}$$

Results from (p,γ) measurements at DragON are eagerly anticipated therefore in order to primarily reduce the uncertainty of the 460.4 keV resonance strength and confirm the 0.4 eV γ-strength of the 824.6 keV resonance. It must be noted that depending on the relative partial elastic and inelastic widths measured as a result from a multi-channel R-Matrix fit on the data of this experiment, a treatment of the reaction rates using the broad resonance formalism of ref. [2] may change the values obtained substantially. For example, the large width of the 824.6 keV resonance may extend radiative-capture further into the low energy regime. Also, the treatment of radiative

capture of the first excited state of ^{21}Ne using the inelastic cross-sections may further strengthen the reaction at higher temperatures. Beyond the information retrieved during this analysis, it is expected that multi-channel R-Matrix fits would enable the determination of most of the important parameters associated with these different reaction rate contributions.

Chapter 8

Summary and Future Work

8.1 The lifetime of the 4.033 MeV state of ^{19}Ne

The measurement of the $^{15}O(\alpha,\gamma)^{19}Ne$ reaction rate via the E_{cm}=0.502 MeV resonance remains a much sought-after result in Astrophysics. The width of this resonance has a large effect on the rates at which the hot-CNO cycle is broken in explosive astrophysical scenarios, and although experiments have been proposed at international facilities such as ISAC-TRIUMF to measure this rate directly, such difficult measurements are likely not to yield confident and accurate results until many years from now. The recent experimental limits [25] imposed on the α-branching ratio of this resonance make a complementary measurement of the lifetime of the 4.033 MeV state even more important, since these results, together, would provide the first experimental limits on the reaction rate without any analogue nucleus or model assumptions involved. The experiment described in this work is one

of the best possibilities so far for a chance to measure the lifetime, given the indications of this work.

This initial experiment was undertaken to try and establish what is needed in an experimental setup to measure the lifetime. What has been found is that the γ-ray detection efficiency would need to increase substantially in order to enable the detection of the 4.033 MeV γ-rays, with sufficient statistics to be able to detect a centroid shift between successive implanted target runs using different stopping mediums. Based on the data collected in the HPGe detectors, it is expected that an initial improvement of at least 2 orders of magnitude in absolute γ-detection efficiency would need to be made in order to simply see the 4.033 MeV γ-rays. This could be done perhaps by introducing a segmented γ-ray array with high solid angle and anti-Compton rejection capabilities. An example of the kind of facility needed in this experiment is the TIGRESS γ-detector array proposed for TRIUMF-ISAC. This consists of an array of segmented high efficiency Germanium detectors, arranged so as to have an absolute efficiency of more than 15% [83]. The clover-style detectors are able to reject Compton scattered γ-rays using a surrounding BGO shield giving a superior peak-to-background ratio. The segmentation of the detectors also allows the correction of Doppler-broadened γ-rays, which is an important feature in this experiment where the shape of the detected peak is crucial to the lifetime measurement.

The particle telescope should be pixellated in the lifetime experiment. This enables the identification of the excited states via the α-particle energies, but more importantly, allows the angle of the recoiling ^{19}Ne to be determined. In this way, the true angle between the direction of motion of the recoiling nucleus and the emitted γ-ray can be determined, so that the

correct Doppler shift effects can be determined in the analysis.

It is the conclusion of this thesis experiment that the ^{3}He(^{20}Ne,^{4}He)^{19}Ne reaction using ^{3}He implanted targets is a viable method of determining the lifetime of the 4.033 MeV state of ^{19}Ne via the Doppler shift attenuation method. The experimental techniques and facilities to do this have been identified. This knowledge should enable an experiment to be designed which could measure the lifetime. It would be a difficult experiment, but nevertheless of great interest to the field of Nuclear Astrophysics.

8.2 Resonance states in ^{22}Mg and the ^{21}Na(p,γ)^{22}Mg reaction

The resonant elastic scattering experiment described in chapters 4 through 7 of this thesis, identified four states in ^{22}Mg associated with proton resonances in the ^{21}Na+p system. A single-channel $\ell = 0$ R-Matrix code was used to fit the elastic data where possible, resulting in the resonance energy and width of one resonance being measured. This method fails to be able to fit other resonances due to a finite strength in the inelastic channel for scattering to the first excited state of ^{21}Na, creating the need for a multi-channel formalism to be used in future calculations.

The inelastic peaks observed in the experiment were used to estimate the total widths and resonance energies of those resonances which could not be fitted with the R-Matrix formalism.

The spin-parity of one state in ^{22}Mg could be deduced from the R-Matrix fit, allowing tentative assignments for analogue states in the mirror

nucleus ^{22}Ne to be made. This may be helpful in deducing the spins of other states in ^{22}Mg by narrowing down the uncertainty between the two nuclei.

The maximum possible widths deduced from this experiment were used to calculate the ^{22}Na(p,γ)^{22}Mg resonant reaction rate for temperatures up to 10 GK, using information assumed from properties of the mirror nucleus. The rates are unchanged with respect to previous calculations below a temperature of around 4 GK. However the calculations show that the reaction rate would be dominated by one of the lower resonances seen in this experiment above 4 GK, temperatures which perhaps occur in highly explosive scenarios such as X-ray bursters. However, these estimations need to be verified via the (p,γ) measurement of the resonances.

The uncertainty of the contribution of lower energy resonances not observed in this experiment poses the greatest problem for the pinning down of the reaction rate over all temperature regimes relevant to astrophysics. However, the DRAGON measurements underway will provide further information on some of these lower resonances in the near future.

In order to determine the spin-parities and relative elastic/inelastic strengths of the resonances seen in this experiment, it is anticipated that further work will be made outwith the duration of this thesis on a multi-channel R-Matrix code. It is hoped that the γ-ray channel can be included in this formalism, enabling a complete description of the true physical processes involved.

A multi-channel formalism will provide a valuable tool for future work in (p,p) experiments with radioactive beams, complementing DRAGON (p,γ) measurements. In this way many more reactions relevant to the rp-process can be studied via medium-to-low energy proton resonances. There

are still many unknowns in the proton-rich isotope region of interest, and the development of new radioactive beams at ISAC and other international facilities will hopefully usher in an era of unprecedented study of the nuclear properties of these radioactive nuclei.

Appendix A

A.1 Doppler shift attenuation method

The Doppler-shifted energy of a γ-ray emitted at an angle θ_γ to the direction of motion of an excited nucleus with velocity $\beta = v/c$ is given by

$$E_\gamma = E_{\gamma 0}\frac{(1-\beta^2)^{1/2}}{1-\beta\cos\theta_\gamma} \tag{A.1}$$

where $E_{\gamma 0}$ is the energy of the γ-ray in the nucleus rest frame. This can be expanded and to first order in β is given by

$$E_\gamma = E_{\gamma 0}(1+\beta\cos\theta_\gamma) \tag{A.2}$$

A beam of excited nuclei all travelling with initial velocity $v(0)$ will decay at a rate

$$\frac{dN(t)}{dt} = -\frac{N_0}{\tau}e^{-t/\tau} \tag{A.3}$$

where t is the actual decay time measured from the time of creation of the excited state (t=0), and τ is the mean lifetime of the state.

If the excited nuclei are created within a matrix of some stopping material, then the nuclei will be decelerating as they decay, resulting in a range of different velocities at the time of decay, and therefore a range of different Doppler-shifted γ-ray energies. A given type of nucleus with given velocity will have a *characteristic stopping time* in any material, ie. the mean time taken for all the ions to slow down to rest in that material. If the lifetime of the state is short compared to the stopping time, then the majority of nuclei will decay long before the nucleus slows down enough for nuclear stopping effects to become important [31]. This means that during the time before decay, electronic stopping effects are the major contributing factor to the slowing down of the nucleus. The energy loss of the ion before decay can be taken as constant if the lifetime is short enough, and is given by [31]

$$-\frac{dE}{d(\rho x)} \equiv -M\frac{dv}{dt} = K_c(v_i/v_0) \tag{A.4}$$

where ρ is the density of the material, M is the mass of the ion, K_c is a stopping constant, $v_i \equiv v(0)$ is the initial velocity of the ion and v_0 is some

fraction of the speed of light, a convenient unit of velocity[1]. The differential equation can be solved to give

$$V = 1 - \alpha_c^{-1} t \tag{A.5}$$

where $\alpha_c = Mv_0/\rho K_c$ is the characteristic stopping time for the constant energy loss given above. $V \equiv v(t)/v(0)$ is a convenient variable since it exists in the interval [1,0]. When $V = 1$, $v(t) = v(0)$ and therefore $E_\gamma = E_{\gamma 0} + E_{\gamma 0}\beta_0 \cos\theta_\gamma$, ie. the γ-ray energy is Doppler-shifted by the full amount possible at that angle (β_0 is the maximum possible value of $\beta(t)$). At the other end of the range, when $V = 0$, $v(t) = 0$ meaning that the ion has stopped and so $E_\gamma = E_{\gamma 0}$ ie. no Doppler shift.

The Doppler relation given by equation A.2 means that the observed γ-ray energy is linear in $\beta(t)$ and so we essentially see the velocity line shape which is given by the number of decays at a certain velocity per velocity interval:

$$\frac{dN(V)}{dV} = y[e^{-y(1-V)} + y^{-1}\delta(V)e^{-y}] \tag{A.6}$$

obtained from equation A.3, where $y = \alpha_c/\tau$.

To get the experimentally observed lineshape, the detector response function has to be considered. Usually a gaussian, a γ-ray detector response

[1]The expression of the initial velocity as a fraction of v_0 enables the low velocity limit $v/v_0 \leq 1$ to be set for different experimental situations, below which nuclear stopping effects become important [31]

function, $\phi(V)$, has the effect of spreading the detected energy (velocity) about its actual value. The experimental lineshape distribution is then given by convoluting the velocity line shape with the response function:

$$[dN(V)/dV]_{exp} = \int_0^\infty y e^{-y(1-V')} \phi(V - V') dV' \tag{A.7}$$

The δ-function part of equation A.6 has been ignored, as it is not important for $\tau \ll \alpha_c$ [31]. A transformation of variables is made into the γ-ray energy system using the relation

$$V(t) = \frac{E_\gamma(t)/E_{\gamma 0} - 1}{\beta(0)\langle \cos\theta_\gamma \rangle} \tag{A.8}$$

where the substitution $V(t)\beta(0) = \beta(t)$ has been made into equation A.2. Note that the inclusion of the averaged cosine of the γ-ray angle has been included to take into account that a real detector subtends a range of emitted γ-ray angles. This enables a direct relationship between the experimentally observed lineshape, $[dN(E_\gamma(V(t))/dV]_{exp}$ and the variables θ_γ, $\beta(0)$, $E_{\gamma 0}$, α_c and τ.

Figure A.1 shows two different velocity line shapes for the decay of γ-rays at $\theta_\gamma = 0°$ in a medium of characteristic stopping time $\alpha_c = 460$ fs, for mean lifetimes of 20 fs (black) and 90 fs (red). It can be seen that the majority of the nuclei decay instantaneously, meaning the γ-rays are detected with the full Doppler-shift at V=1. The exponential tail then falls off as less γ-rays are emitted at the lower velocities. The shape for the longer

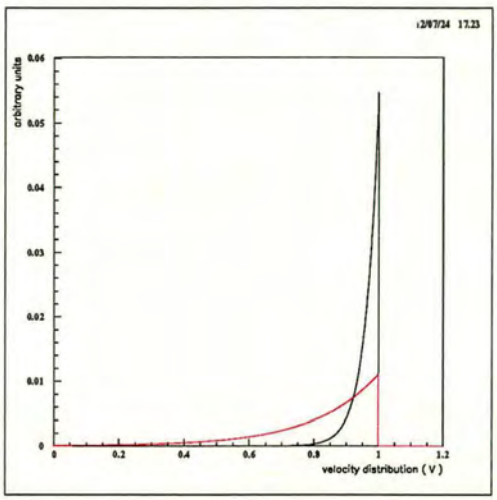

Figure A.1: *Velocity line shapes for decaying nuclei with different lifetimes.*

lifetime is more extended as the probability of decay at a later time, and therefore lower velocity, is enhanced.

Figure A.2 shows the experimentally observed lineshapes when convoluted with a typical detector gaussian response function (3 keV fwhm) for lifetimes of 9 fs (black), 20 fs (red) and 90 fs (blue) in the same medium as above. Note that the detector response convolution has the effect of shifting the centroid position of the observed lineshape.

The extraction of the mean lifetime from the spectrum shape can be done in several ways. A direct fit of the spectrum line shape would yield a measurement of τ if the stopping time of the material is known. It is useful however, to define the quantity the *Doppler Shift Attenuation Factor* as the ratio of the average Doppler shift to the the maximum Doppler shift. This is given by

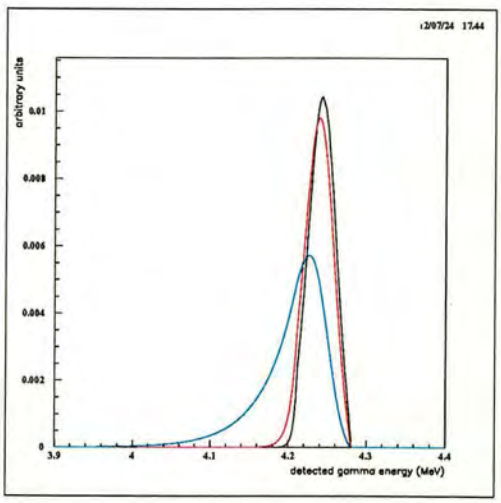

Figure A.2: *Velocity line shapes (transformed into detected γ-ray energy frame) convoluted with detector response function, for different mean state lifetimes.*

$$F(\tau) = \frac{\int_0^1 V[dN(V)/dV]dV}{\int_0^1 [dN(V)/dV]dV}$$

$$= 1 - y^{-1}(1 - e^{-y}) \tag{A.9}$$

which when $\tau \ll \alpha_c$ gives the relation

$$1 - F(\tau) = \tau/\alpha_c \tag{A.10}$$

Therefore, the lifetime could be extracted by measuring the centroid positions of the Doppler-shifted peak for a situation where the nucleus is

decaying in vacuum (ie. full Doppler shift), and decaying in a matrix of known α_e, where the Doppler-shift is attenuated. This gives the measurement of $F(\tau)$. Such a method has been utilised using heavy-ion reactions with backed and unbacked targets [32]. This method is versatile in that it can access nuclei far from stability using a suitable combination of target and projectile, however, it is also limited to the range of self-supporting thin targets that can be made.

A.2 Implantation and analysis of ^{3}He targets

A.2.1 Target implantation

Several concepts must be considered when undertaking the implantation of the ^{3}He into the metal foils. Firstly, as detailed in ref. [30], the ^{3}He is implanted in the stopping material resulting in a distribution of ^{3}He ions over a finite distance. The incoming ^{20}Ne beam will lose energy in the target before reaching the ^{3}He, and because of the energy loss distribution, reactions will occur at a range of different beam energies. Also, the peak of the ^{3}He spatial distribution is where the majority of reactions occur, so as the ^{20}Ne beam loses energy in the beginning of the target, it will interact, with ^{3}He at different mean energies for different target materials due to the difference in stopping powers. It is therefore important to implant the ^{3}He as close as possible to the surface of the target, to minimise the energy loss of the incoming beam, and also to ensure that the ^{3}He is confined to a small distance range inside the target, while also ensuring that the maximum number of ^{3}He ions possible are implanted. In a final DSAM measurement,

the ^{3}He depth profile would need to be known accurately, and folded in with the stopping powers of ^{20}Ne to give the mean interaction energy for each target. This effectively defines the mean velocity of the recoil at the moment of creation, and therefore the maximum Doppler-shift possible for the emitted γ-ray. In ref. [30], the ^{3}He profile was measured using the reaction ^{3}He(^{16}O,p)^{18}F*(1.04 MeV), for which the relevant cross-sections were known, and using experimental stopping powers of ^{16}O ions [84] in the various metals, expressing the ^{3}He profile in terms of energy loss of the incoming beam.

For the reaction test experiment in this work, it was decided to implant three types of foil with ^{3}He ions for the purpose of: a) testing the implantation technique and b) testing the ^{3}He(^{20}Ne,^{4}He)^{19}Ne reaction using the foils with an experimental setup close to that needed for a DSAM measurement. In an initial implantation using the 500 kV ion-implanter machine at the Surrey Centre for Research in Ion Beam Applications, University of Surrey, UK, 3 μm thick targets of Tungsten and Tin and Aluminium were implanted with ^{3}He ions at an energy of 300 keV through an Aluminium degrader foil of thickness 0.8 μm. Despite the low Coulomb barrier for Aluminium, it was used in the test experiment to investigate how much background would result from fusion using this material. The low stopping power of Aluminium makes it an attractive choice for the DSAM experiment, if indeed the background contribution is not too high. The 500 kV implanter was limited to energies of around a few hundred keV because its optics are optimised for those energies. Therefore the inclusion of the degrader was required to ensure the ^{3}He ions were incident on the target material at low energy. The degrader thickness was dictated by the available self supporting material

available from suppliers, and therefore the beam energy was chosen to be 300 keV so that the ^{3}He ions would be implanted in the materials at a mean depth of around $\sim$0.2 μm. A beam spot scan pattern was used during the implantation in order to ensure a uniform implantation areal density over the implanted area, which was chosen to be 1 cm^2.

The implanted dose in the targets was measured by integrating the collected charge on the foils over time. A dose of 3×10^{17} ions/cm^2 was aimed for, over the 1 cm^2 area. This dose, equivalent to about 16 μA·h of ^{3}He$^+$ beam, was successfully used in the DSAM experiment of ref. [30] to measure a fast lifetime. Doses of ^{4}He twice this magnitude were used in the studies of ref. [31], where the effects of the fractional volume change of the target foil caused by the implantation were considered and ^{4}He retention after implantation was also measured, the results showing that the Au and Al foils lost up to 50-60% of the implanted dose, while the Ta and Mg foils retained 100% [31]. The implantation of the Tin target was unsuccessful, its low melting point making it unsustainable under the $\sim 5\mu$A beam currents required to allow the implantations to be performed in the allotted time.

Two other sets of targets were prepared. The second set included Gold and Tungsten and doses of 3×10^{17} and 1×10^{18} ions/cm^2 were implanted in each type over an area of 1 cm^2. This set was implanted using the Danfysik DF 1090 200kV Ion Implanter, also at the University of Surrey. This machine is able to produce good quality ^{3}He beams at low energies, hence no need for a degrader foil. The targets were implanted at 25 keV, also ensuring a mean depth of around $\sim 0.2\mu$m. An X-Y ^{3}He scan pattern of $\sim$ 0.5 Hz was used to ensure the uniformity of the distribution, while currents with an average of 80 μA were sustained on target. A third set of Tungsten targets were

prepared with the same machine with doses of 3×10^{17} ions/cm^2.

In the final DSAM measurement it would be imperative to know the ^{3}He distribution inside the target foils in order to be able to calculate the modified stopping power due to the presence of the implanted ions. In ref. [31] the reaction ^{4}He(^{18}O,nγ)^{21}Ne was used to determine the implantation distributions. While a similar method would eventually be required in order to determine the distribution of the implanted ^{3}He in this work, it is also important to know how much ^{3}He is retained after implantation (to ensure the required implanted dose is met) and after bombardment with ^{20}Ne in the main experiment. For this analysis, the reaction ^{3}He(d,p)^{4}He was used.

A.2.2 Foil analyses

A deuteron beam of 500 keV was produced using the ALTAIS tandetron machine at the LARN laboratory, University of Namur, Belgium. This was incident on the implanted side of the targets, where the mean depth is 0.2 μm. The beam current was integrated directly from the target holder, and a +ve suppression voltage was applied to the target holder in order to ensure secondary electrons did not escape from the target. A PIPS detector was placed at 160° lab angle to detect the back-scattered beam particles from the target as a means of normalisation. A 1.5 mm thick PIPS detector was placed at 90.45 mm from the target at an angle of 135°, in front of which was placed a 12 μm thick mylar foil to allow the transmission of protons from the reaction ^{3}He(d,p)^{4}He while stopping any heavier particle. The target doses were calculated using

$$N_{target} = \left(\frac{d\sigma}{d\Omega_{lab}} d\Omega_{lab} \right)^{-1} \frac{N_{det}}{N_{inc}}$$

where the number of incident particles, N_{inc}, is derived from the backscattered deuterons. The differential cross-section for this reaction, which is almost isotropic in the CM frame, was taken from ref. [85]. The analysis was performed for target sets 2 and 3, both implanted using the Danfysik machine. Set 2 had the analysis performed after exposure to a 10 nA, 57 MeV ^{20}Ne beam over periods of around 10 hrs each, while set 3 had the analysis made both prior to and post experiment, where they were also bombarded with a ^{20}Ne beam of 50 MeV at ~10 nA. The targets of set 2 had been left undisturbed for almost six months prior to the experiment, while set 3 were implanted less than a week before exposure to the beam. Table A.1 shows the results obtained from the ^{3}He(d,p)^{4}He measurement. We can see that the measured dose of the target in set 2 which was supposedly implanted with 3×10^{17} ions/cm^2 has dropped by a factor of 3 as the result of exposure to the heavy-ion beam and diffusion over time. However, we do not know the actual dose that was implanted here. The other target in set 2 was thought to have been implanted with 1×10^{18} ions/cm^2, and was subsequently measured as containing 1.84×10^{17} ions/cm^2. However, set 3, measured less than a week after implantation and prior to exposure to the heavy-ion beam, show that although a dose of 3×10^{17} ions/cm^2 was aimed for, only 1.04×10^{17} and 1.14×10^{17} ions/cm^2 were present. After exposure to the heavy-ion beam, doses of 1.04×10^{17} and 1.08×10^{17} ions/cm^2 were recorded, respectively. The indication here is that, although 3×10^{17} ions/cm^2 were thought to have

Target set	Material	Pre-experiment dose (ions/cm^2)	Post-experiment dose (ions/cm^2)
2	W	(nominal 1×10^{18})	1.84×10^{17}
2	W	(nominal 3×10^{17})	1.01×10^{17}
3	W	1.04×10^{17}	1.04×10^{17}
3	W	1.14×10^{17}	1.08×10^{17}

Table A.1: *Results from the $^3He(d,p)^4He$ reactions performed at Namur, showing the foil contents pre- and post-experiment.*

been implanted in most cases, much less was actually measured after only a short time. The diagnostics of the implantation process could possibly be out by a factor 3, or perhaps an initial large percentage of ^{3}He is lost immediately after implantation, then settling down into a relatively stable state. If so, then the indication is also that the targets which had more in them at the beginning seem to have lost relatively more ^{3}He, perhaps implying that there is a distortion of the metal matrix at these higher densities enough to allow excess ^{3}He to diffuse out quickly. However, without more information, it is difficult to say for certain what is actually occurring inside these implanted targets. For the purposes of the experiment, it has been confirmed that there was at least 1×10^{17} ions/cm^2 in all these targets during the time of exposure to the heavy-ion beam.

Appendix B

B.1 Kinematics

We begin with the general situation of a heavy beam particle (m_1) colliding with target particle (m_2). The detected light recoil (m_4) is scattered at a lab angle θ_{lab}, while the heavier scattered particle, which can be excited with excitation energy E_x is scattered at an angle ϕ_{lab} (figure B.1).

From conservation of linear momentum and conservation of total kinetic energy, we can express the lab kinetic energy of the recoil, T_4, as a function of the reaction Q-value, θ, ϕ, the masses, and the beam energy, T_1:

$$T_4^{1/2} = \frac{1}{m_3}\cos\theta_{lab}(m_4 m_1 T_1)^{1/2} / \left(1+\frac{m_4}{m_3}\right) \pm$$
$$\left[\frac{1}{m_3^2}\cos^2\theta_{lab}(m_4 m_1 T_1) - \left(1+\frac{m_4}{m_3}\right)\left(\left(\frac{m_1}{m_3}-1\right)T_1 - q\right)\right]^{1/2} / \left(1+\frac{m_4}{m_3}\right) \tag{B.1}$$

where $q = Q - E_x$. For inelastic and elastic scattering, we make the substitution $m_1 = m_3, m_2 = m_4$. Then $Q = 0$ and $q = -E_x$.

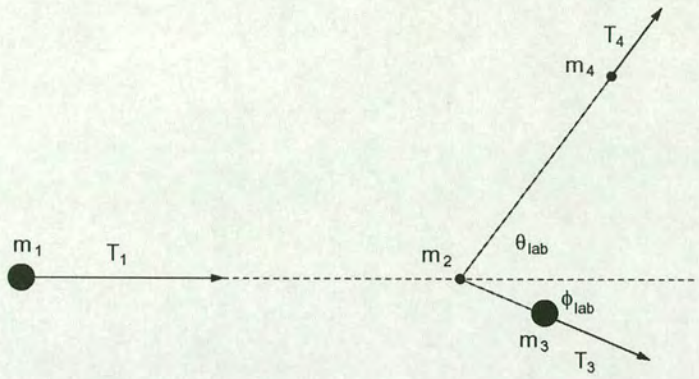

Figure B.1: *Geometry of inverse kinematics reaction.*

For elastic scattering ($E_x = 0$) equation B.1 reduces to:

$$T_4 = 4\cos^2\theta_{lab}\frac{m_1 m_2}{(m_1+m_2)^2}T_1 \tag{B.2}$$

Using the beam energy to centre-of-mass conversion $E = T_1 m_2/(m_1 + m_2)$ we can then write:

$$T_4 = 4E\frac{m_1}{m_1+m_2}\cos^2\theta_{lab} \tag{B.3}$$

We can express the kinetic energy T_4' of an inelastically scattered particle at angle θ_l arising from a collision of initial centre-of-mass energy E, in terms of its relationship to an elastically scattered particle kinetic energy T_4 at the same angle, arising from the same initial centre-of-mass energy E, by substituting equation B.2 into equation B.1:

$$T_4' = \left[\frac{\left(\frac{T_4(m_1+m_2)^2}{4m_1^2}\right)^{1/2} \pm \left(\frac{T_4(m_1+m_2)^2}{4m_1^2} - (1+m_2/m_1)E_x\right)^{1/2}}{1+m_2/m_1} \right]^2 \quad \text{(B.4)}$$

The centre-of-mass energy versus beam energy relation can also be used to express T_4' as a function of centre-of-mass energy, as in equation 6.6.

B.2 R-Matrix single-channel cross-section derivation

Here we focus on the derivation of the single-channel (elastic only) differential cross-section in order to fit the elastic scattering excitation functions. Although the scattering of ^{21}Na+p is a multi-channel problem due to the possibility of inelastic excitation to the first excited state of ^{21}Na, this will be an approximation to a multi-channel fit. The R-Matrix formalism of ref. [11] is used, as described in section 2.2.

We begin with the general multi-channel equation for differential cross-section of a process $\alpha \rightarrow \alpha'$ given in ref. [11] section VIII:

$$\frac{d\sigma_{\alpha\alpha'}}{d\Omega_{\alpha'}} = [(2I_1+1)(2I_2+1)]^{-1} \sum_{ss'} (2s+1) \frac{d\sigma_{\alpha s,\alpha' s'}}{d\Omega_{\alpha'}} \quad \text{(B.5)}$$

where

$$\frac{d\sigma_{\alpha s,\alpha' s'}}{d\Omega_{\alpha'}} = \frac{\pi}{(2s+1)k_\alpha^2} \times (CT + RT + IT) \tag{B.6}$$

The Coulomb term, CT, is given by

$$CT = (2s+1)\left|\frac{1}{\sqrt{4\pi}}\eta_\alpha \sin^{-2}(\theta_\alpha/2)\exp[-2i\eta_\alpha \ln\sin(\theta_\alpha/2)]\right|^2 \delta_{\alpha s,\alpha' s'} \tag{B.7}$$

using Euler's relation $\exp i\theta = \cos\theta + i\sin\theta$, we can expand the Coulomb term by multiplying the expression in the vertical brackets by its complex conjugate to eliminate the imaginary part:

$$CT = (2s+1)\frac{1}{4\pi}\eta_\alpha^2 \sin^{-4}(\theta_\alpha/2)\delta_{\alpha s,\alpha' s'} \tag{B.8}$$

which in the case of s=0, gives the Rutherford cross-section when multiplied by the π/k_α^2.

The resonant term, RT, is given by

$$RT = \frac{1}{\pi}\sum_L B_L P_L(\cos\theta) \tag{B.9}$$

The B_L coefficients are given by

$$B_L = \frac{1}{4}(-)^{s-s'} \sum_{J\ell} \bar{Z}(\ell_1' J_1 \ell_2' J_2, s' L)\bar{Z}(\ell_1 J_1 \ell_2 J_2, sL)(T^J_{\alpha' s' \ell_1', \alpha s \ell_1})(T^J_{\alpha' s' \ell_2', \alpha s \ell_2})^* \tag{B.10}$$

The summation integer L is a summation over $|\ell_i - \ell_i'|$, as in ref. [86], which in our case of single-channel s-waves always equals zero. Thus the summation over L is dropped here and greatly simplifies some of the terms in the cross-section formulae.

The $\bar{Z}$ coefficients are related to the Racah[1] coefficients, W by the relation

$$\begin{aligned}\bar{Z}(\ell_1 J_1 \ell_2 J_2, sL) = (2\ell_1 + 1)^{\frac{1}{2}}(2\ell_2 + 1)^{\frac{1}{2}}(2J_1 + 1)^{\frac{1}{2}} \\ \times (2J_2 + 1)^{\frac{1}{2}}(\ell_1 \ell_2 00|L0)W(\ell_1 J_1 \ell_2 J_2, sL)\end{aligned} \tag{B.11}$$

where $(\ell_1 \ell_2 00|L0)$ are the Clebsch-Gordan coefficients. These terms are also related to the Z coefficients of Blatt and Biedenharn as [11]

$$\bar{Z}(\ell_1 J_1 \ell_2 J_2, sL) = i^{\ell_1 - \ell_2 - L} Z(\ell_1 J_1 \ell_2 J_2, sL) \tag{B.12}$$

so in our case of s-wave scattering with L=0, the terms are equivalent and can be simplified as in ref. [5]:

[1]General analytic expressions for these coefficients can be found in ref [87]

$$Z(0J_10J_2, s0) = (-1)^{J_1-s}(2J_1+1)^{\frac{1}{2}} \tag{B.13}$$

where because $J \equiv J_2 = J_1$ and $\ell = 0$, $J - s = 0$. Thus in equation B.10 the two $\bar{Z}$ terms become equal to $(2J+1)$ in the special case of s-wave single-channel scattering.

The transition matrix element $T^J_{\alpha' s' \ell', \alpha s \ell}$ can be written as

$$T^J_{\alpha' s' \ell', \alpha s \ell} = \exp 2i\omega_{\alpha' \ell'} - U^J_{\alpha' s' \ell', \alpha s \ell} \tag{B.14}$$

$U^J_{\alpha' s' l', \alpha s l}$ is the collision matrix, which is given by

$$U^J_{\alpha s \ell, \alpha s \ell} = \exp 2i(\omega_{\alpha \ell} + \delta^J_{\alpha s \ell}) \tag{B.15}$$

for on-diagonal elements (elastic scattering). It is this simplification which results in the single-channel formula since only on-diagonal elements contribute to the expression. Again, we can expand the complex terms in the expression and multiply by the complex conjugate to arrive at the single-channel expression for the resonance term:

$$\begin{aligned} RT = \frac{1}{4\pi} \sum_{J\ell} (2J+1)\{&[\cos 2\omega_\ell - \cos 2(\omega_\ell + \delta^J_\ell)]^2 \\ &+ [\sin 2\omega_\ell - \sin 2(\omega_\ell + \delta^J_\ell)]^2\} P_\ell(\cos\theta) \end{aligned} \tag{B.16}$$

The interference term, IT, is written[2]

$$IT = \delta_{\alpha s\ell,\alpha' s'\ell'} \frac{1}{\sqrt{4\pi}} \sum_{J\ell} (2J+1) 2Re[i(T^J_{\alpha s\ell,\alpha' s'\ell'})^* C_\alpha P_\ell(\cos\theta)] \tag{B.17}$$

which, with the same method of algebraic manipulation, can be expressed as

$$\begin{aligned} IT = & \frac{1}{2\pi} \sum_{J\ell} (2J+1)\eta_\alpha \sin^{-2}(\theta/2) \times \\ & \{\sin(2\eta_\alpha \ln\sin(\theta/2))[\cos 2\omega_\ell - \cos 2(\omega_\ell + \delta^J_\ell)] + \\ & \cos(2\eta_\alpha \ln\sin(\theta/2))[\sin 2\omega_\ell - \sin 2(\omega_\ell + \delta^J_\ell)]\} \times \\ & P_\ell(\cos\theta) \end{aligned} \tag{B.18}$$

The phase shifts δ^J_ℓ are given by

$$\delta^J_\ell(E) = \arctan \frac{\mathcal{P}_\ell(E)}{(R^J_\ell)^{-1} + B_\ell + S_\ell(E)} - \phi_\ell \tag{B.19}$$

R is the R-Matrix, and is constructed by

$$R^J_\ell = \sum_{Ji} \frac{\gamma^2_{Jli}}{E_i - E} \tag{B.20}$$

[2]Note that in the cross-section terms, CT and IT, there exist Kronecker delta symbols which are identical to unity if the exit channel and entrance channel are identical, ie. elastic scattering., and which are zero otherwise, ie. the occurrence of reactions.

with γ_{Jli} the reduced widths and E_i the state energies as in chapter 2.2. The summation integer ℓ is then dropped from these equations since the assumption of only $\ell = 0$ partial waves is being used in this formalism. The essential difference between this formalism and the spin-zero, single-channel formalism used in ref. [73] is that the spin-parity dependence of the absolute differential cross-section is correct for our combination of target and projectile spins, since the ref. [73] formalism practically assumes a spin-statistical factor, $\omega = 1$ for s-wave scattering.

Appendix C

C.1 Simulation of experimental data

Simulations were made representing the actual data taken in the experiment, for the ^{21}Na beam at energies of 690, 880, 990, 1144, 1240, 1340, 1440 and 1560 keV/A. An artificial s-wave resonance was positioned in the centre of each thick target proton spectrum in order to be able to determine how the original yield function is modified by the experimental effects. Each resonance was calculated using a proton width of $\Gamma_p = 8$ keV and a spin statistical factor, ω of $\frac{5}{8}$ representing a compound state of $J^\pi = 2^+$, and the single channel Breit-Wigner parametrization detailed in ref. [54].

Simulated proton spectra were plotted for the innermost annulus of the forward angle detector, with high statistics, and the results analysed.

Figures C.1 and C.2 shows the simulated proton spectra for the eight beam energies fitted with gaussian functions at the edges. The actual functional form of the edge will not in general be gaussian, since it is a convolution of a step with two gaussians. However, a gaussian fit reproduces the target edge shape approximately. The beam energy centroid position is

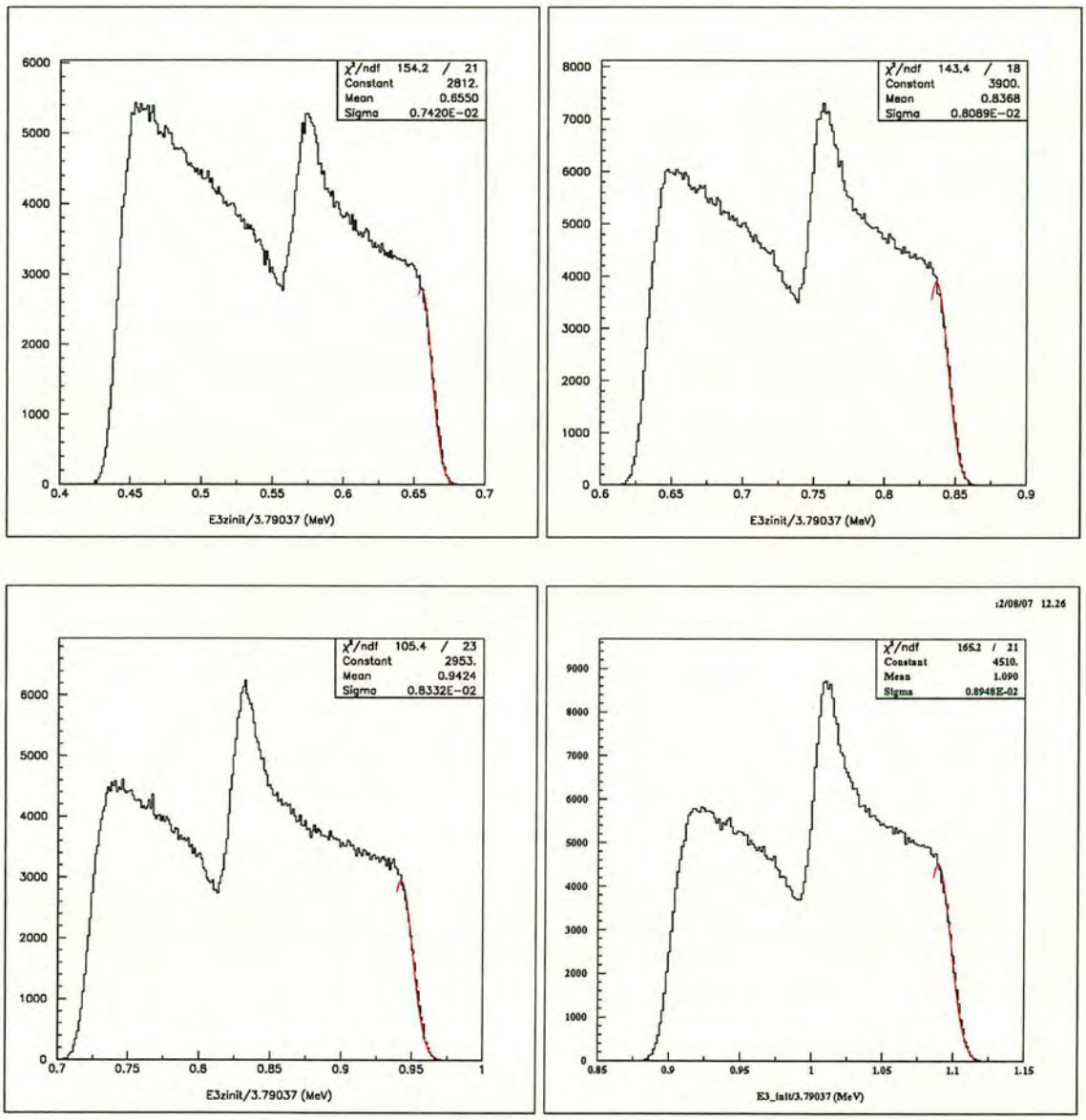

Figure C.1: *Gaussian fits to the edges of the simulated proton spectra for a range of incident beam energies. The x-axes show centre-of-mass energy while the y-axes show counts per channel.*

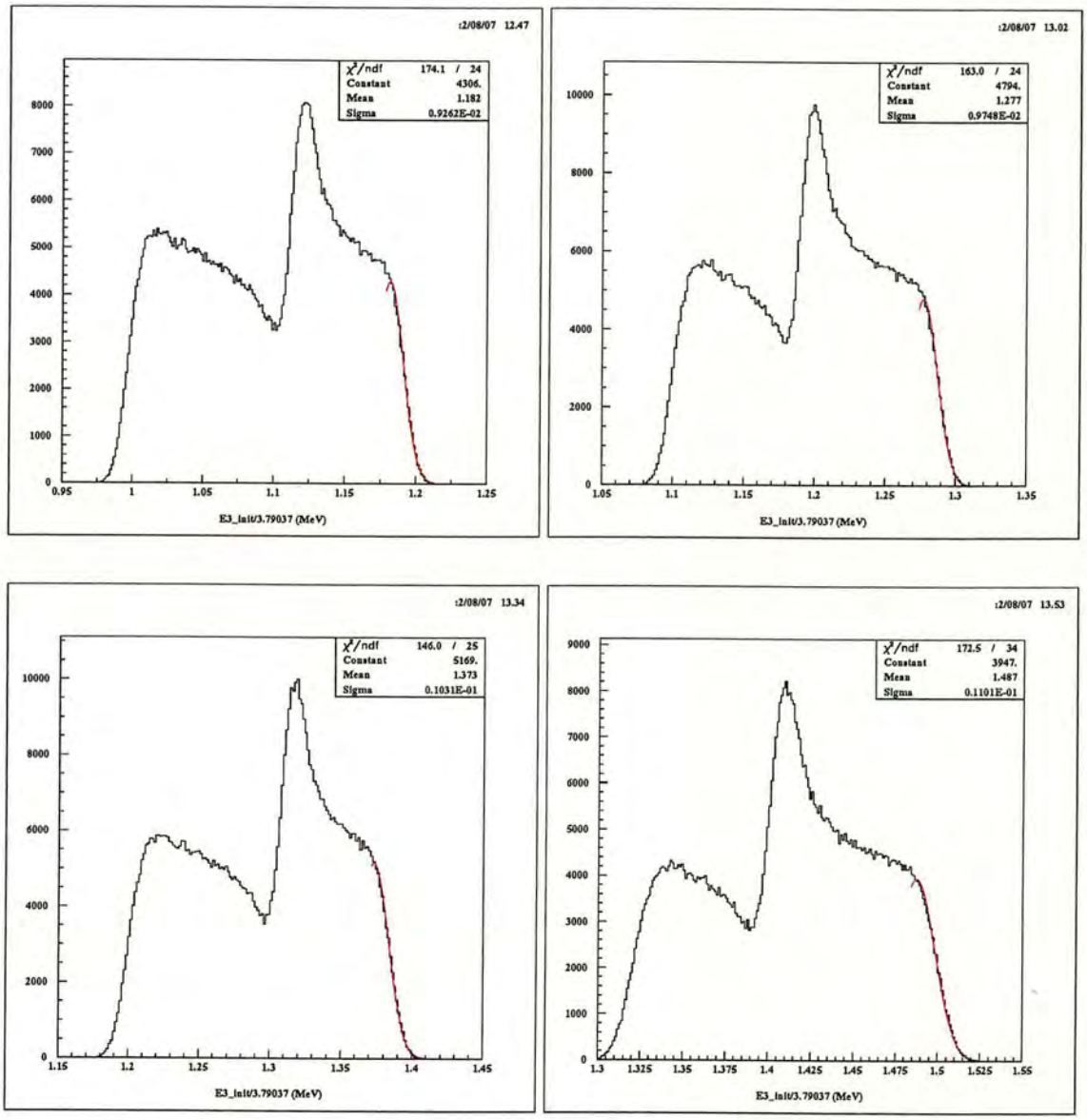

Figure C.2: *Gaussian fits to the edges of the simulated proton spectra for a range of incident beam energies. The x-axes show centre-of-mass energy while the y-axes show counts per channel.*

closely reproduced by taking the half maximum point of the gaussian slope, ie. $\tilde{x}+2.35\sigma/2$ where $\tilde{x}$ is the mean of the gaussian and σ is the variance[1].

Figures C.3 and C.4 shows the result of fitting the spectra with a resonance curve using **MINUIT** in **PAW**. In each case, the resonance energy, width and spin of the resonance is fixed, and only the normalisation and experimental resolution allowed to vary.

The results of these fits are listed in table 6.1 and shown in figure 6.5.

[1]It must be noted that the correct gaussian which reproduces the beam energy centroid via this method is not necessarily the one which minimises the χ^2, since by fitting from further down the target edge we include less data points and therefore can easily find a gaussian to give a small χ^2. However, by taking the fit limits from roughly at the maximum counts of the target edge, the beam energy centroid is reproduced within 1 keV in the centre-of-mass.

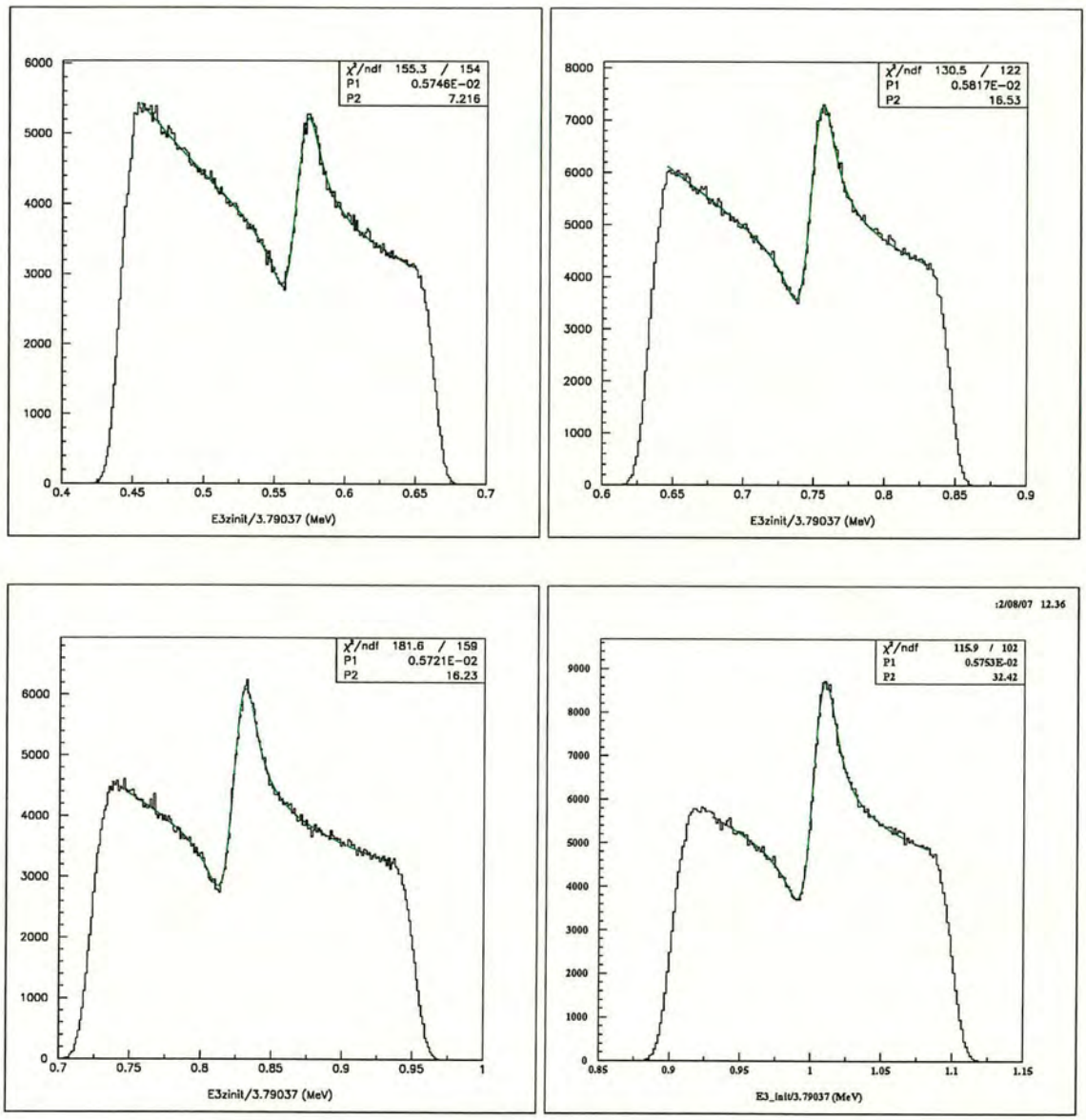

Figure C.3: *Resonance fits to the simulated proton spectra for a range of incident beam energies. The x-axes show centre-of-mass energy while the y-axes show counts per channel.*

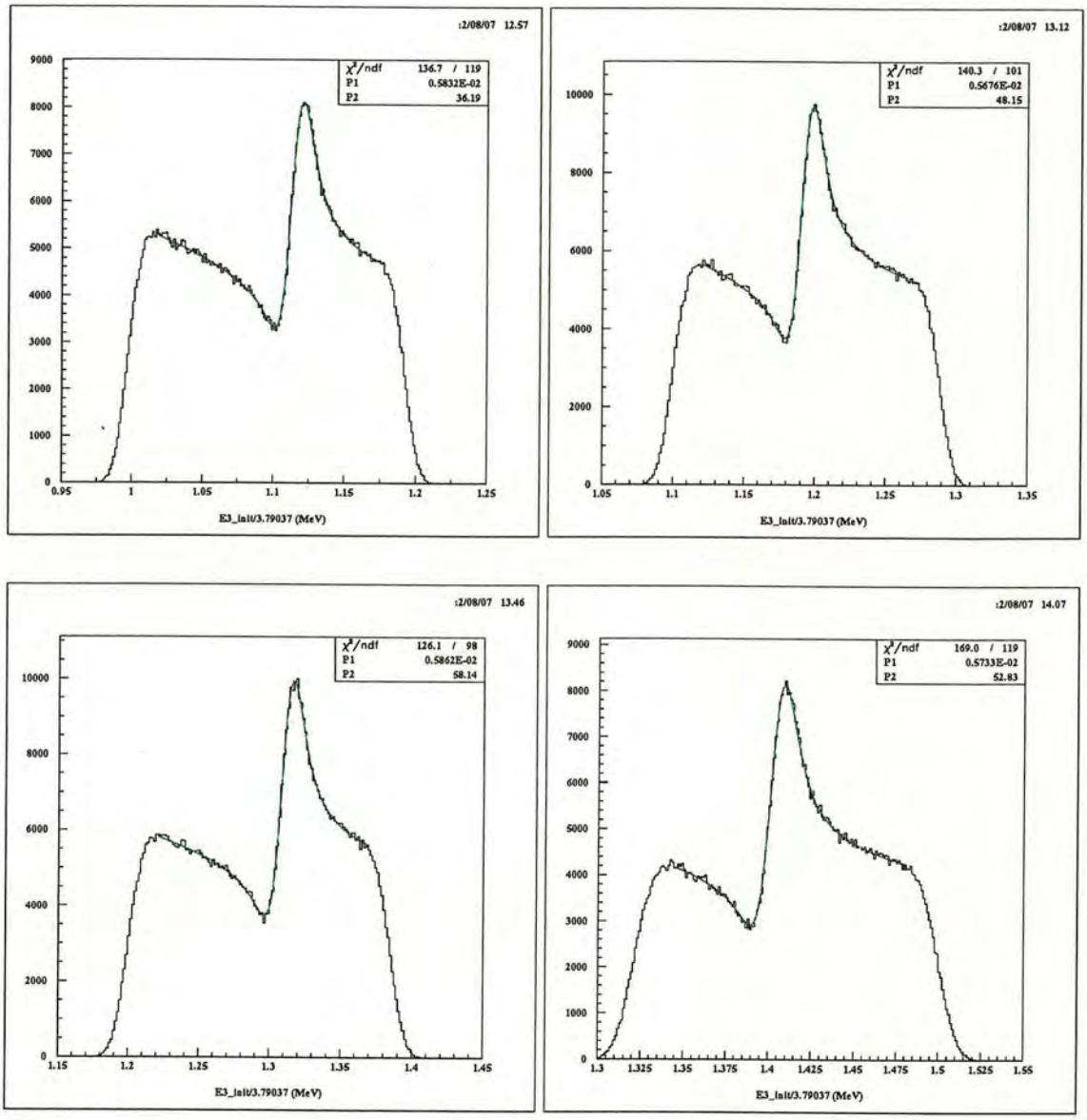

Figure C.4: *Resonance fits to the simulated proton spectra for a range of incident beam energies. The x-axes show centre-of-mass energy while the y-axes show counts per channel.*

Appendix D

D.1 Large angle data

Data from the detector at larger laboratory angles, from the ^{21}Na+p experiment, were omitted from the analysis due to the difficulty in reproducing the experimental smearing effects at these large angles, and also because of the inability to include more than 16 angles in the R-Matrix fitting program due to memory constraints.

In figure D.1 are shown four spectra (uncorrected against the ^{21}Ne+p resonance, unlike the data from the other detector) representative of the data from the large angle detector. Gaps in the data mean that the target runs did not overlap properly in these regimes due to excessive smearing.

D.2 Trigger logic

The trigger logic functionality for the ^{21}Na+p experiment is shown in figure D.2.

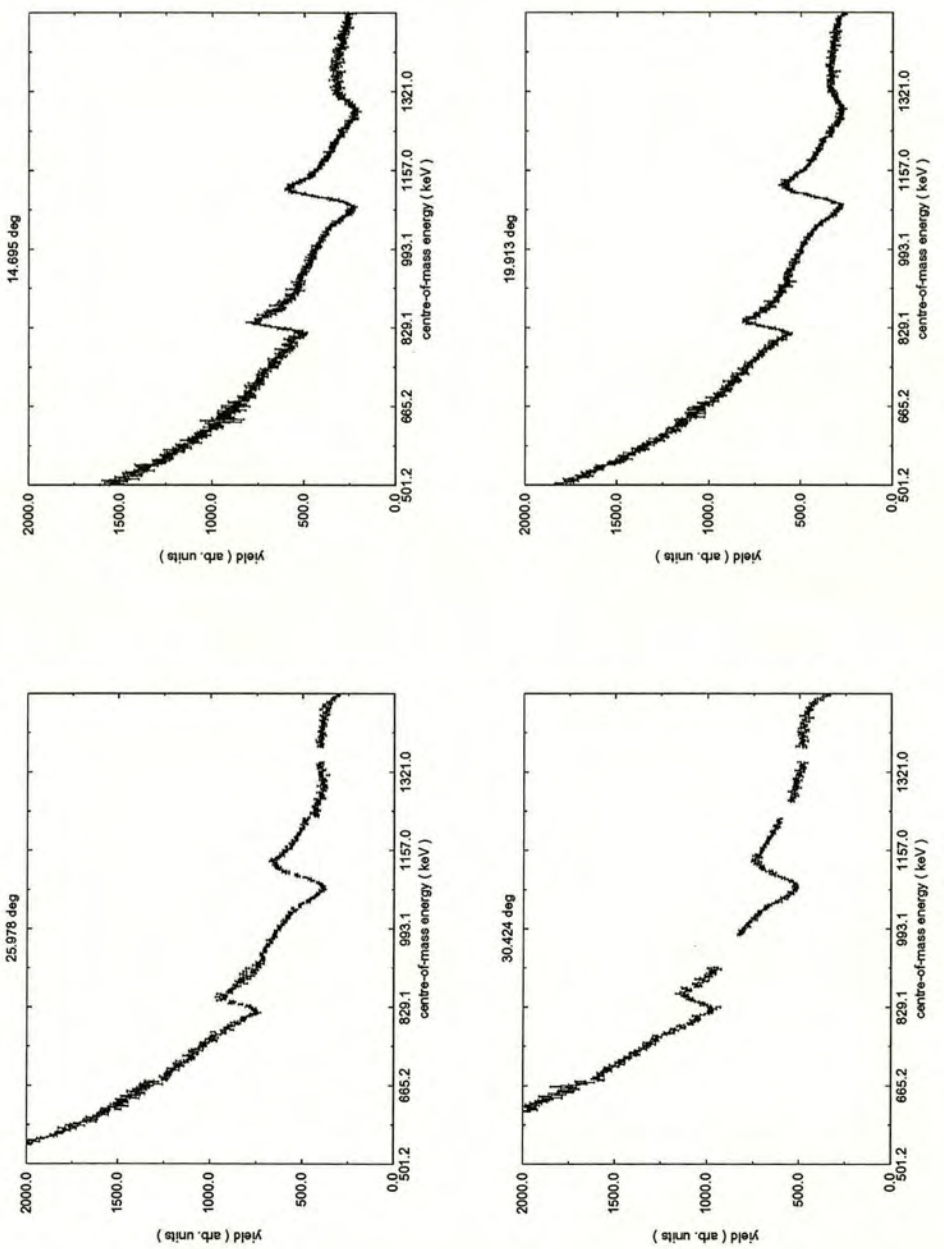

Figure D.1: *Representative spectra from the LEDA detector closest to the target in the $^{21}Na+p$ experiment.*

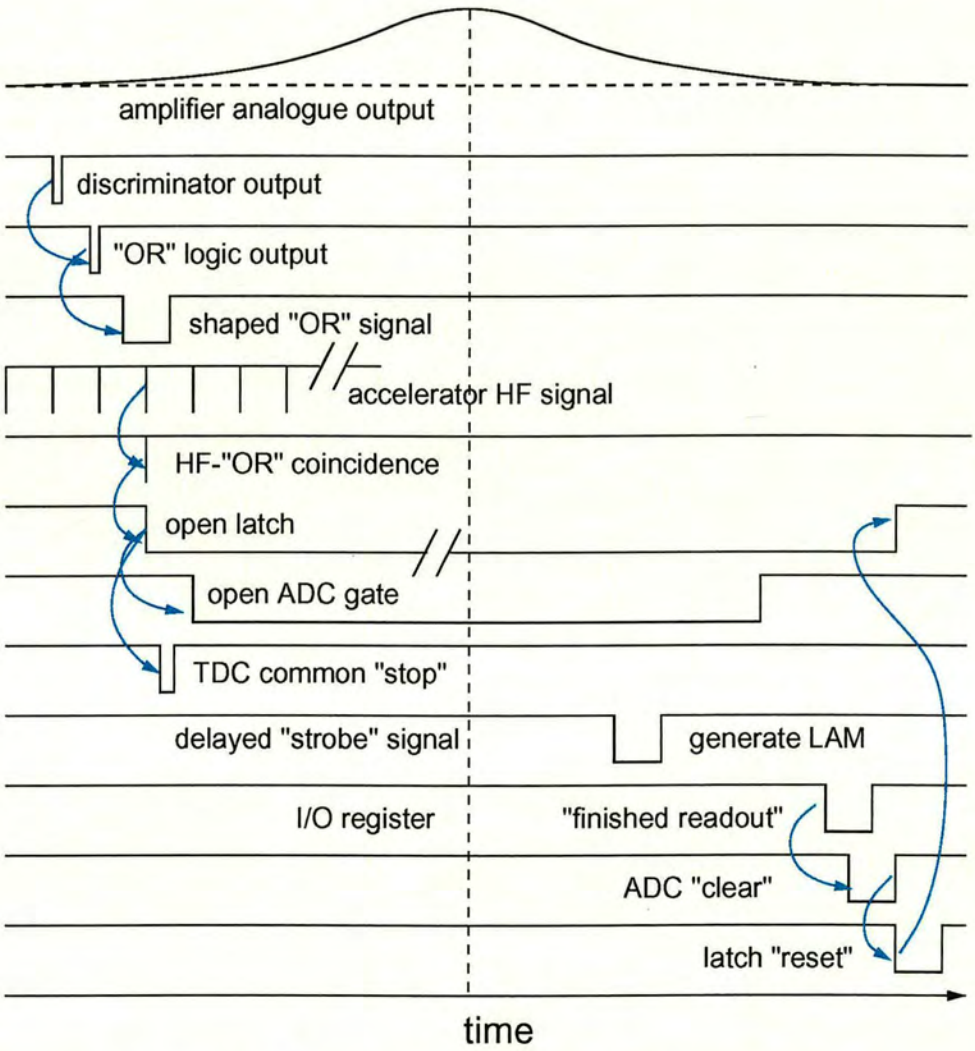

Figure D.2: *$^{21}Na+p$ experiment trigger logic functionality.*

Bibliography

[1] M. Zeilik, S. A. Gregory, and E. v. P. Smith. *Introductory Astronomy and Astrophysics.* Saunders College Publishing, (1992).

[2] Claus Rolfs and William S. Rodney. *Cauldrons in the Cosmos.* The University of Chicago Press, (1988).

[3] J. Dunlop. Undergraduate lectures in astrophysical cosmology. Edinburgh University, (1998-99).

[4] Map Science Team. C.O.B.E website: http://map.gsfc.nasa.gov, (2002).

[5] Darren Groombridge. *Breakout from the hot-CNO cycle via the $^{18}Ne(\alpha,p)^{21}Na$ reaction.* PhD thesis, University of Edinburgh, (2001).

[6] T. P. Snow. *The Dynamic Universe.* West Publishing Co., (1991).

[7] W. Bradfield-Smith. *Measurement of the $^{18}Ne(\alpha,p)^{21}Na$ reaction rate: and its implications for Nuclear Astrophysics.* PhD thesis, University of Edinburgh, (1999).

[8] C. Angulo *et al.* A compilation of charged-particle induced thermonuclear reaction rates. *Nuclear Physics*, **A656**:3–183, (1999).

[9] Erich Vogt. *Resonance Reactions, Theoretical: Nuclear Reactions.* North Holland, (1959).

[10] James David Powell. *Constraints on the low-energy E1 cross section of* $^{12}C(\alpha,\gamma)^{16}O$ *from the* β*-delayed* α *spectrum of* ^{16}N. PhD thesis, University of Toronto, (1995).

[11] A.M. Lane and R. G. Thomas. R-Matrix Theory of Nuclear Reactions. *Reviews of Modern Physics*, **30**:257–353, (1958).

[12] L. Buchmann. Notes about multi-channel, multi-state reaction theory. Unpublished, (2002).

[13] G. Wallerstein *et al.* Synthesis of the elements in stars: forty years of progress. *Reviews of Modern Physics*, **69**:995–1084, (1997).

[14] F.K. Thielemann *et al.* Element synthesis in stars. *Prog.Part.Nucl.Phys.*, **46**:5–22, (2001).

[15] W. Bradfield-Smith *et al.* Nuclear trigger for x-ray bursts. Unpublished.

[16] P.V. Magnus *et al.* Measurement of $^{15}O(\alpha,\gamma)^{19}Ne$ resonance strengths. *Nuclear Physics*, **A506**:332–345, (1989).

[17] A.E. Champagne and M. Wiescher. Explosive hydrogen burning. *Annual Review of Nuclear and Particle Science*, **42**:39–76, (1992).

[18] M.W. Greene and E. B. Nelson. Energy levels of ^{19}Ne. *Physical Review*, **153**:1068–1070, (1966).

[19] K. Gul, B. H. Armitage, and B. W. Hooton. The energy levels of ^{19}F and ^{19}Ne. *Nuclear Physics*, **A122**:81–96, (1968).

[20] J.D. Garrett, R. Middleton, and H. T. Fortune. Hole states in ^{19}Ne. *Physical Review C*, **2**:1243–1254, (1970).

[21] D.A. Hutcheon et al. The dragon facility for nuclear astrophysics at triumf-isac. In *Proceedings of the 7th International Symposium on Nuclei in the Cosmos - Tokyo, Japan*, (2002).

[22] P.V. Magnus *et al.* Measurement of the $^{15}N(\alpha,\gamma)^{19}F$ resonances at E_{cm}=536 keV and 542 keV. *Nuclear Physics*, **A470**:206–212, (1987).

[23] A.M. Laird *et al.* The $^{18}Ne(d,p)^{19}Ne$ reaction: A way to measure $^{15}O(\alpha,\gamma)$? In *Proceedings of the 5th international symposium on Nuclei in the Cosmos - Volos, Greece*, (1998).

[24] A.N. Ostrowski *et al.* Study of ^{19}Ne α-decay properties related to the hot-CNO breakout reaction $^{15}O(\alpha,\gamma)^{19}Ne$. TRIUMF Research Proposal: E874, (2000).

[25] K. Rehm *et al.* In *Proceedings of the 7th International Symposium on Nuclei in the Cosmos - Tokyo, Japan*, (2002).

[26] A.N. Ostrowski *et al.* Study of the hot-CNO Breakout Reaction $^{15}O(\alpha,\gamma)^{19}Ne$. Experiment Proposal for CYCLONE - CRC, Louvain-la-Neuve, (1999).

[27] G. Hackman *et al.* Intermediate-energy coulomb excitation of ^{19}Ne. *Nuclear Physics*, **A682**:356–362, (2001).

[28] W.R. Dixon *et al.* The lifetime of the 3907 keV state of ^{19}F. *Physics Letters*, **62A**:479–482, (1977).

[29] A. Antilla *et al.* Lifetimes of low-lying states in ^{19}F. *Nuclear Physics*, **A334**:205–216, (1979).

[30] W.N. Catford *et al.* Lifetime of the 1.04 MeV 0^+, T= 1 state in ^{19}F. *Nuclear Physics*, **A407**:255–268, (1983).

[31] E.K. Warburton, J. W. Olness, and C. J. Lister. Lifetimes of the ^{21}Ne 2796-, 1747-, and 2867-keV levels. *Physical Review C*, **20**:619–640, (1979).

[32] D. Branford and I. F. Wright. A doppler shift attenuation method for measuring lifetimes in the range $10^{-13} - 10^{-15}$s using heavy-ion induced reactions. *Nuclear Instruments and Methods*, **106**:437–443, (1972).

[33] Goodfellow. http://www.goodfellow.com, (2002).

[34] Cyclotron Research Centre Louvain la Neuve. http://www.cyc.ucl.ac.be, (2002).

[35] D. J. Skyrme. The passage of charged particles through Silicon. *Nuc. Inst. Meth.*, **57**:61–73, (1967).

[36] H. Schatz. X-ray binaries: Nuclear physics at the extremes. Nuclear Astrophysics Summer School lecture, TRIUMF, Vancouver, Canada, (2002).

[37] M. Wiescher. Lecture on Nuclear Astrophysics - IOP half day meeting, York University, (2002).

[38] G. Vancraeynest *et al.* ^{19}Ne(p,γ)^{20}Na and ^{19}Ne(d,n)^{20}Na reaction and its astrophysical implications for the transition of the hot CNO cycle to the rp process. *Physical Review C*, **57**:2711–2723, (1998).

[39] J. José, A. Coc, and M. Hernanz. Nuclear uncertainties in the NeNa-MgAl cycles and production of ^{22}Na and ^{26}Al during nova outbursts. *The Astrophysical Journal*, **520**:347–360, (1999).

[40] INTEGRAL website. http://astro.estec.esa.nl, (2002).

[41] Gamma Ray Observatory. http://cossc.gsfc.nasa.gov/, (2002).

[42] M. Wiescher *et al.* Explosive hydrogen burning in novae. *Astron. Astrophys.*, **160**:56–72, (1986).

[43] R. A. Paddock. (p,t) Reaction on Even-Even N=Z Nuclei in the 2s1d Shell. *Physical Review C*, **5**:485–499, (1971).

[44] S. Czajkowski *et al.* Beta-p,-2p,-alpha spectroscopy of ^{22,23,24}Si and ^{22}Al. *Nuclear Physics*, **A616**:278c–285c, (1997).

[45] B. Blank *et al.* The spectroscopy of ^{22}Al: a βp, β2p and $\beta\alpha$ emitter. *Nuclear Physics*, **A615**:52–68, (1997).

[46] Claus Rolfs *et al.* A study of the low-lying states in ^{22}Mg. *Nuclear Physics*, **A191**:209–224, (1972).

[47] N. Bateman *et al.* Measurement of the ^{24}Mg(p,t)^{22}Mg reaction and implications for the ^{21}Na(p,γ)^{22}Mg stellar reaction rate. *Physical Review C*, **63**:035803, (2001).

[48] J. A. Caggiano *et al.* Excitation energies in ^{22}Mg from the ^{25}Mg(^{3}He,^{6}He)^{22}Mg reaction. *Physical Review C*, **66**:015804, (2002).

[49] G. P. A. Berg. In *Proc. 7th Int. Sym. Nuclei in the Cosmos, Tokyo*, (2002).

[50] A. A. Chen *et al.* Structure of ^{22}Mg and its implications for explosive nucleosynthesis. *Physical Review C*, **63**:065807, (2001).

[51] A. B. McDonald and E. G. Adelberger. A study of ^{22}Mg by the ^{20}Ne(^{3}He,n) reaction. *Nuclear Physics*, **A144**:593–606, (1970).

[52] W. P. Alford *et al.* Structure of ^{22}Mg, ^{26}Si, ^{34}Ar and ^{38}Ca via the (^{3}He,n) reaction. *Nuclear Physics*, **A457**:317–336, (1986).

[53] H. Grawe *et al.* Lifetime measurements in ^{22}Mg. *Nuclear Physics*, **A237**:18–28, (1975).

[54] Th. Delbar *et al.* One-step energy scanning of wide low-lying 1^- resonances in ^{13}C+p and ^{13}N+p scattering. *Nuclear Physics*, **A542**:263–277, (1992).

[55] W. Galster *et al.* Target and detection techniques for the $^{13}N(p,\gamma)^{14}O$ reaction using radioactive ion beams: $^{13}C(p,\gamma)^{14}N$ reaction as a test case. *Physical Review C*, **44**:2776–2787, (1991).

[56] J.-S. Graulich, R. Coszach, and P. Leleux. Nuclear astrophysics experiments: reactions and elastic scattering. *Eur. Phys. J.*, **A 13**:221–225, (2002).

[57] J.-S. Graulich *et al.* 7.07 MeV resonant state in ^{19}Ne reexamined through a new measurement of the $^{18}F(p,\alpha)^{15}O$ reaction and $^{18}F(p,p)$ scattering. *Physical Review C*, **63**:011302, (2000).

[58] R. Coszach. *Etude de la diffusion resonnant proton-noyau par la method de la cinematique inverse.* PhD thesis, UCL, Louvain-la-Neuve, (1997).

[59] R. Coszach *et al.* Resonant scattering of isobaric ^{19}Ne and ^{19}F beams on an H target. *Physical Review C*, **50**:1695–1701, (1994).

[60] R. E. Laxdal. private communication, (2002).

[61] R.E. Laxdal. Design specification for ISAC HEBT. Technical Report TRI-DN-99-23, TRIUMF, (1999).

[62] T. Davinson *et al.* Louvain-Edinburgh Detector Array (LEDA): a silicon detector array for use with radioactive nuclear beams. *Nuc. Inst. Meth.*, **A454**:350–358, (2000).

[63] B. Chambon *et al.* Elastic and inelastic proton scattering from ^{21}Ne and T=1 energy levels in ^{22}Na. *Physical Review C*, **12**:1–13, (1975).

[64] M. Dombsky. ISAC yields and targets page, TRIUMF personal homepage. http://www.triumf.ca/people/marik/homepage.html, (2002).

[65] W.N. Lennard. Nonlinear response of Si detectors for low-Z ions. *Nucl. Inst. Meth.*, **A248**:454–460, (1986).

[66] W.R. Leo. *Techniques for Nuclear and Particle Physics Experiments.* Springer-Verlag, (1994).

[67] L. Buchmann. private communication, (2002).

[68] A. Anttila. Investigation of ^{22}Ne excited states. *Z. Phys.*, **234**:455, (1970).

[69] J. Keinonen *et al.* Absolute resonance strengths in the ^{20,21,22}Ne(p,γ)^{21,22,23}Na and ^{21}Ne(p,pγ)^{21}Ne reactions. *Physical Review C*, **15**:579–586, (1977).

[70] H.L. Berg *et al.* Proton induced resonnaces on ^{21}Ne. *Nuclear Physics*, **A276**:168–188, (1976).

[71] J. Görres *et al.* Search for low-energy resonances in ^{21}Ne(p,γ)^{22}Na and ^{22}Ne(p,γ)^{23}Na. *Nuclear Physics*, **A385**:57–75, (1982).

[72] J. Görres *et al.* Proton-induced direct capture on ^{21}Ne and ^{22}Ne. *Nuclear Physics*, **A408**:372–396, (1983).

[73] L. Buchmann *et al.* Analysis of the total ^{12}C(α, γ)^{16}O cross section based on available angular distributions and other primary data. *Physical Review C*, **54**:393–410, (1996).

[74] F. Barker. The boundary condition parameter in R-matrix theory. *Australian Journal of Physics*, **25**:341–348, (1972).

[75] C. Brune. An alternative parameterization of R-matrix theory. *Physical Review C*, **66**:044611, (2002).

[76] C. Angulo and P. Descouvement. R-matrix analysis of interference effects in ^{12}C(α, α)^{12}C and ^{12}C(α, γ)^{16}O. *Physical Review C*, **61**:064611, (2000).

[77] P. M. Endt. Supplement to energy levels of A = 21-44 nuclei (VII). *Nuclear Physics*, **A633**:1–220, (1998).

[78] C. Ruiz *et al.* Strong resonances in elastic scattering of radioactive ^{21}Na on protons. *Physical review C*, **65**:042801, (2002).

[79] M. Wiescher, J. Görres, and F.-K. Thielemann. ^{17}F(p,γ)^{18}Ne in explosive hydrogen burning. *The Astrophysical Journal*, **326**:384–391, (1988).

[80] Nadya A. Smirnova and Alain Coc. ^{21}Na(p,γ)^{22}Mg thermonuclear reaction rate for ^{22}Na production in novae. *Physical Review C*, **62**:045803, (2000).

[81] Alain Coc *et al.* Update of nuclear reaction rates affecting nucleosynthesis in novae. *Nuclear Physics*, **A688**:450–452, (2001).

[82] P. M. Endt. Energy levels of A = 21-44 nuclei (VII). *Nuclear Physics*, **A521**:1–400, (1990).

[83] TIGRESS. http://physun.physics.mcmaster.ca/ jcw/nucexp/Tigress.htm, (2002).

[84] J.F. Ziegler. *The stopping and range of ions in matter.* Pergamon, New York, (1980).

[85] T. Bonner, J. P. Conner, and A. B. Lillie. Cross section and angular distribution of the ^{3}He(d,p)^{4}He nuclear reaction. *Phys. Rev.*, **88**:473–476, (1952).

[86] J.M. Blatt and L. C. Biedenharn. The Angular Distribution of Scattering and Reaction Cross Sections. *Reviews of Modern Physics*, **24**:258–272, (1952).

[87] L.C. Biedenharn, J. M. Blatt, and M. E. Rose. Some Properties of the Racah and Associated Coefficients. *Reviews of Modern Physics*, **24**:249–257, (1952).